博士論文

Double resonance Raman spectroscopy of single wall carbon nanotubes and graphene

(単層カーボンナノチューブとグラフェンの
二重共鳴ラマン分光)

朴珍成

平成20年

Acknowledgment

I would like to use this opportunity to thank the many people who contributed to this thesis over the three years of my PhD course studies at Tohoku University. First of all, I am very thankful to my supervisor Professor Riichiro Saito for his teaching me the fundamentals of research. His detail advices not only for physics but also for writing a paper and making a presentation have improved me as a scientist during the three years. I am indebted to Mr. Kentaro Sato who helped me for installing many useful computer programs. I appreciate Dr. Wataru Izumida and Dr. Kenichi Sasaki for stimulating discussion. I would like to thank our collaborator Professor Mildred S. Dresselhaus for her kind advices for nanotube physics. I thank to Professor Young Hee Lee and Mr. Ki Kang Kim for their hospitality and stimulating discussion about the metallicity dependence of the G' band Raman intensity during my visit to SKKU in Korea. I also thank to Mr. Alfonso Reina and Professor Jing Kong from MIT in USA for stimulating discussion of the G' band for multi-layer graphene. I am also grateful to Professor Ado Jorio and Dr. Cristiano Fantini for stimulating discussion on their experimental result for resonance window of carbon nanotubes. I also thank to Dr. Jie Jiang and Dr. Eduardo B. Barros for stimulating discussion during their stay in Japan. I am indebted to Monbukagakusho for financing my stay in Japan. Part of the work is supported by the 21st century COE program.

I am sincerely thankful to my Japanese host-family Hiroyuki Toyohara-san and his family for very warm friendship during the three years in Sendai. I am also sincerely thankful to my hometown seniors Professor Young Su Yoon and Dr. Kye Hoon Do who gave me great encouragement to finish this thesis.

Last of all, I appreciate my family for their continuous support.

Abstract

Resonance Raman spectroscopy of single wall carbon nanotubes (SWNTs) is widely used for evaluating the sample quality and the population of (n, m) SWNTs for a given sample, in which a SWNT is specified by two integers n, m. For Raman intensity calculation, we need to understand the electron-photon and electron-phonon interactions, and the Raman resonance window (hereafter, γ) in carbon nanotube system. Here, the γ value is defined by an energy region which gives resonance Raman enhancement. So far, we have used a constant value (0.06 eV) for the γ values for different (n, m) SWNTs. Experimentally, the γ value depends on the tube diameter and chirality. In this thesis, we calculate the Raman resonance window for different (n, m) SWNTs. For a resonance system, the Raman resonance window is related to the energy dissipation by inelastic electron-phonon scattering and obtained by calculating the transition probability of a photo-excited electron in the conduction band. The transition probability calculated by electron-phonon scattering is given by the Fermi Golden rule. The electron-phonon scattering is considered for 48 possible scattering processes, that is, intra- and inter-valley, forward and backward, emission and absorption, and six phonon modes. The calculated γ values are compared with Raman spectral width in the experiment directly. Using these γ values, we calculate the G' band Raman spectra, especially for a double resonance Raman scattering, which has a strong metallicity dependence in experiment. We suggest that the G' band comes from the overtone of iTO phonon mode by deducing the G' band properties. The electron-phonon matrix elements for iTO phonon mode show the dependence of electronic transition energy such as E_{22}^{S}, E_{11}^{M}, and E_{33}^{S}. The γ values for m-SWNTs give a smaller value than that for s-SWNTs. This is the reason why the G' band intensity depends on the metallicity in SWNTs. In addition, we calculate the G' band spectra of multi-layer graphene, in which the G' band Raman spectra change in shape, width, and peak position when the number of graphene layers increase from one (1L) to three (3L). Comparison

with single layer graphene, multi-layer graphene has inter-layer interaction between π electrons on the different layers, and then the energy band structure of the multi-layer graphene is split to several energy sub-bands around the Fermi level. The split sub-bands make many double resonance Raman scattering (DR) processes, and give broad the G' band compared with single layer graphene. Thus, for double (2L) and triple (3L) layer graphenes, there are four and nine possible DR processes for the G' band, respectively. However, Raman intensity calculation shows that each sub-band which appears due to corresponding DR process depends on its wave vector, and then the G' band of double and triple layer graphenes have three and five components, respectively. The calculated G' band intensity of multi-layer graphene depends on the number of graphene layers, and compares with the experiments.

Contents

Chapter 1

Introduction

1.1 Purpose of this study

The physics of carbon nanotubes has rapidly developed into a new research field since multi-wall carbon nanotube was discovered by S. Iijima in 1991 [1] and since single wall carbon nanotubes (SWNTs) was discovered two years later [2, 3]. Carbon nanotube is defined by a cylindrical graphene sheet with a nanoscale (1 nm=10^{-9} m) diameter and a microscale (1 μm=10^{-6} m) length. Most of the observed SWNTs have diameter less than 3 nm. Therefore, the SWNTs can be considered as one dimensional (1D) nano-structures because of high aspect ratio. A 1D SWNT can behave as either metallic or semiconducting nanotube depending on two integers (n, m) or two key structural parameters, chirality and diameter [4, 5]. Carbon nanotube is an ideal system for studying the physics of 1D material. Many theoretical and experimental researchers have focused on the relationship between the atomic and electronic structures, or on the electron-electron and electron-phonon interaction. Theoretical and experimental studies in various fields of SWNTs, such as mechanics, optics, chemistry, biology, and electronics, have also focused on both the fundamental physical properties and the commercial application of carbon nanotubes. These studies, in recent years, have generated significant breakthrough in the area of nano-science and technology.

Resonance Raman spectroscopy (RRS) and photoluminescence (PL) spectroscopy provide powerful tools to investigate the geometry and characterization of SWNTs for different samples. The unique optical and spectroscopic properties observed in SWNTs are mainly due to the 1D confinement of the electronic and phonon states. In particular, the 1D confinement of the electron (phonon) state results in the so-called van Hove singularities (vHSs) in the density of states (DOS) of SWNT as a function of energy [5, 6]. The vHSs in the DOS or corresponding the electronic joint density of states (JDOS) play an important role on various optical phenomena. When the incident excitation laser energy matches to the vHS for a SWNT in the JDOS between the valence and conduction bands, one can find a RRS resonance enhancement for the corresponding Raman scattering process, which we call resonance Raman spectroscopy. Thus, the RRS intensity allows one to obtain the information in detail about the phonon properties of SWNTs as well as the electronic properties. Recently, many theoretical studies in the optical properties of SWNTs have been performed in order to explain experimental observation. The resonance Raman scattering process in SWNT consists of the electron-photon and electron-phonon scattering processes [7, 8]. Therefore, for the RRS intensity calculation, we need to understand the electron-photon and electron-phonon interaction in a SWNT. The calculation of these interaction matrices has been able to explain the electronic and phonon structure of SWNTs with different chirality and diameter. However, for more precise RRS intensity calculation, we need to understand the Raman resonance window for different SWNTs. Here, the resonance window is defined by an energy region which gives resonance Raman enhancement [9]. In this thesis, we calculate the Raman resonance window for SWNTs with different chirality and diameter. Using these values, we then calculate the Raman spectra especially for a so-called G' band (~ 2700 cm^{-1}) of SWNT and multi-layer graphene.

1.1.1 Raman resonance window

Hereafter we overview the problems that are discussed in this thesis. Detailed definitions will be given in the following chapters. RRS can be used to assign the (n, m) value of a SWNT from a plot of the energy separation E_{ii} between the i-th vHS in the valence band and the i-th vHS conduction band as a function of diameter of the SWNT, which we call the Kataura plot [10]. RRS of SWNTs is also widely used for evaluating the sample quality and the population [7, 11] of (n, m) SWNTs in actual samples. In the analysis of Raman spectra, not only the resonance energies for the given (n, m) SWNTs, but also the Raman intensities relative to the intensity of other (n, m) SWNTs or of other phonon modes are important for evaluating the population of SWNTs in the generally available sample in which many (n, m) SWNTs are mixed to one another. The radial breathing mode (RBM, 100∼300 cm^{-1}) and G band (1550∼1600 cm^{-1}) Raman intensities [8,12] and the PL intensity [13] show the presence of a strong (n, m) chirality and diameter dependences, which are calculated by using an extended tight binding (ETB) calculation of the electronic [14] and phonon [12] structures. The calculated results are directly compared with (1) experimental PL intensity measurements on samples prepared at different synthesis temperatures [13], (2) experimental Raman/PL intensity ratio measurements [15], and (3) direct transmission electron microscope (TEM) measurements of the diameter distribution [16]. The agreement between theory and experiment is satisfactory except for some exceptions for small diameter SWNTs.

The first order Raman intensity, RBM and G band, as a function of phonon frequency ω and excitation laser energy E_{L} is given by:

$$I(\omega, E_{\text{L}}) = \sum_i \left| \sum_a \frac{M_{\text{el-op}}(i,b) M_{\text{el-ph}}(b,a) M_{\text{el-op}}(a,i)}{(E_{\text{L}} - (E_a - E_i) - i\gamma)(E_{\text{L}} - (E_a - E_i) - E_{\text{ph}} - i\gamma)} \right|^2, \tag{1.1.1}$$

where i, a, and b denote, respectively, the initial state, the excited state, and the scattered state of an electron, $M_{\text{el-op}}$ is the electron-photon interaction matrix, and $M_{\text{el-ph}}$ is the electron-phonon interaction matrix. Here E_{L}, E_i, E_a and E_{ph} are, respectively, the excitation laser energy, the initial state electronic energy, the excited state electronic energy, and the phonon energy. In Eq. (1.1.1), we have two energy difference denominators $(E_{\text{L}} - (E_a - E_i) - i\gamma)$ and $(E_{\text{L}} - (E_a - E_i) - E_{\text{ph}} - i\gamma)$ given by a time-dependent perturbation theory. If the condition $E_{\text{L}} = E_a - E_i$ (incident resonance) or $E_{\text{L}} = E_a - E_i + E_{\text{ph}}$ (scattered resonance) is satisfied, we expect the large resonance enhancement of Raman intensity, which is called resonance Raman effect. The resonance Raman intensity is very sensitive to the resonance window parameter γ. Experimentally, we can observe this γ value as the spectral width of the RBM spectra as a function of excitation laser energy (Raman excitation profile, REP) [9], and we see both the diameter and chiral angle dependences of the γ values. Moreover, the γ value for metallic SWNT (m-SWNT) is larger than that for semiconducting SWNT (s-SWNT) [9]. However, in the previous intensity calculations [8, 11], we used a constant value (0.06 eV) for the γ values for all SWNTs. This might be the reason why we do not get good agreement in the population analysis between the calculated and experimental values of the population of (n, m) especially for

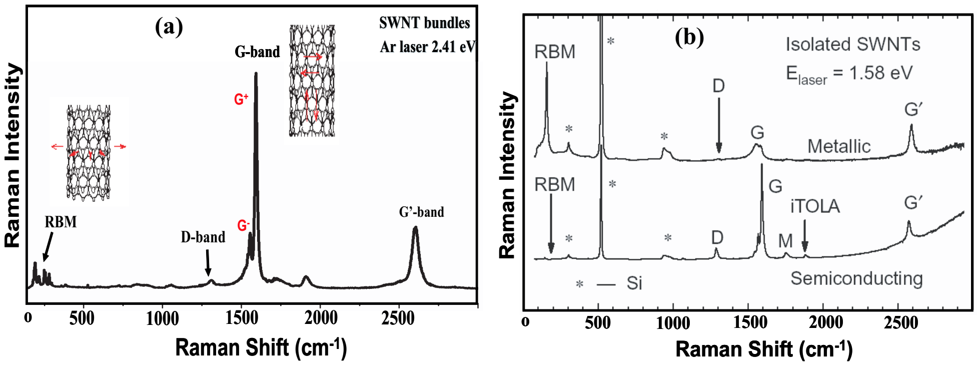

Figure 1.1: (a) Raman spectra taken HiPCO SWNT bundle with a excitation laser energy 2.41 eV. The spectra show the radial breathing mode (RBM), D band ($\sim$ 1350 cm^{-1}), G band, and G' band features. (b) Raman spectra taken from a metallic (top) and a semiconducting (bottom) SWNT grown by the CVD method on an Si/SiO$_2$ substrate [17]. The Si/SiO$_2$ substrate provides contributions to the Raman spectra denoted by "$*$".

smaller diameter SWNTs [15]. In order to get more reliable calculated intensity values, we will calculate the γ value as a function of (n, m) in Chapter 4.

1.1.2 Metallicity dependence in G' band of SWNT

The chiralities of SWNTs can be identified using the RBM frequencies in Raman spectroscopy [18]. The RBM frequencies $\omega_{\text{RBM}}(\text{cm}^{-1})$ are inversely proportional to the diameters of the SWNTs:

$$\omega_{\text{RBM}} = \frac{C_1}{d_t} + C_2, \tag{1.1.2}$$

where d_t(nm) is the diameter of a SWNT, and C_1 and C_2 are the constants that vary according to the environment such as bundle or substrate. For example, the fitted values are $C_1 = 248$ (cm^{-1}·nm) and $C_2 = 0$ (cm^{-1}) for isolated nanotubes on a SiO$_2$ substrate, and $C_1 = 234$ (cm$^{-1}\cdot$nm) and $C_2 = 10$ (cm^{-1}) for bundles [18,19]. However the assignment of the (n, m) values becomes difficult for a relatively higher E_{ii} and a larger d_t because there are many data of (n,m) in a small region of the Kataura plot. The G band spectra can distinguish the metallicity (either metallic or semiconducting) of the SWNTs, where the separation of frequencies for the split G band (G^+ and G^-) is larger for metallic SWNTs than that for semiconducting SWNTs and the G^- band spectrum of metallic SWNT is broaden [20] (see Fig. 1.1). The relative G band Raman intensity (G^+/G^-) strongly

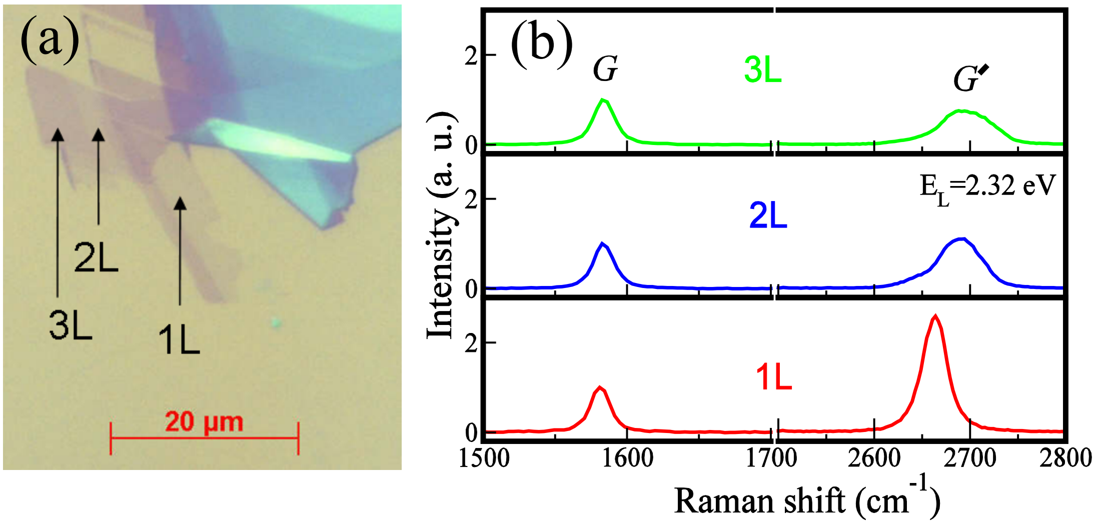

Figure 1.2: (a) Optical image of single, double and triple layer graphene on Si with a 300 nm SiO_2 over-layer, labeled in the paper as 1L, 2L, and 3L, respectively. (b) Raman spectra of 1L, 2L, and 3L graphene at excitation laser energy $E_{\mathrm{L}} = 2.32$ eV [26].

depends on the chiral angle [20], and the G^+/G^- value becomes large for SWNT with a chiral angle near a zigzag nanotube [21, 22]. Therefore, we need other simple information on the metallicity of SWNT by Raman spectroscopy. Recently, the metallicity dependence of the G' band intensity relative to the G band intensity was observed by separating the metal-enriched or semiconducting-enriched SWNT samples by the oxidation of nitronium ions [23–25]. The experimental results are confirmed by calculating the Raman intensity for the G' band using the double resonance Raman scattering theory, which is one of the results of the present thesis.

We will demonstrate that the G' band intensity of SWNTs shows a strong dependence on the metallicity of the sample in Chapter 5.

1.1.3 G' band of multi-layer graphene

Graphene is defined as a two-dimensional (2D) hexagonal lattice of carbon atoms. The recent discovery of graphene has stimulated great interest in the scientific community by the report of the massless and relativistic properties of the conduction electrons in this single layer system. It is in fact these special electrons that are responsible for the unusual properties of the quantum Hall effect [27, 28] in single layer and double layer graphene.

Many groups are now making devices by using graphene ribbon, because the 2D nanostructure of graphene makes it a promising candidate for electronic applications due to its high mobility, and its chemical and mechanical stability [29, 30]. The single layer graphene is usually obtained by using the procedure of micro-mechanical cleavage of bulk graphite, which is the same technique that allowed the isolation of graphene for the first time [31]. A single graphene layer placed on top of a Si wafer with a carefully chosen thickness of SiO_2 (300 nm) becomes visible in an optical microscope (see Fig. 1.2). However, this SiO_2 thickness dependence on visibility is very sensitive, and if the thickness is exceeded by about 5 nm, the single layer graphene becomes completely invisible in an optical microscope [31]. For overcoming of this difficulty, many groups use a Raman spectroscopy under an optical microscope, for distinguishing single layer from multi-layer graphene. Raman spectroscopy allows accurate measurement of the number of graphene layers on a SiO_2 substrate [32], using the G' band of the Raman spectra. The G' band Raman spectra change in shape, width, and peak position when the number of graphene layers changes from one to three [32] (see Fig. 1.2). It has been known that the electronic band structure around the Fermi level for multi-layer graphene plays an important role in an inter-valley double resonance Raman scattering process [32]. By analyzing the G' band of double layer graphene with several excitation laser energies, we can probe both the electronic energy and phonon dispersion around the K or K' point in the Brillouin zone of graphene [33].

In Chapter 6, we will report the results on the calculation of the Raman G' band as a function of number of graphene layers, and compare theory with experiment.

1.2 Organization

The present thesis is organized as follows. In the remaining section of Chapter 1, we explain the background for understanding this thesis. In Chapter 2, the structures of graphene and SWNT are reviewed and the concept of cutting lines leading to the zone-folding scheme is discussed. Also, the electronic band structures of graphene and SWNT are reviewed based on the simple tight binding and extended tight binding models. In Chapter 3, we introduce the calculation methods used in this thesis. The electron-phonon interaction matrix elements for the evaluation of Raman resonance windows is reviewed, which was developed by J. Jiang *et al.* [12, 34] in our group. Then, we show how to get the Raman resonance windows of the Raman excitation profiles for (n, m) SWNTs. The G' band intensity calculation for each (n, m) SWNT is introduced based on the double resonance scattering theory. For the G' band Raman intensity calculation, we consider the electron-phonon interaction matrix, the electron-photon interaction matrix, and the Raman resonance window. In Chapter 3, the electron-photon interaction matrix is simply reviewed, which was developed by J. Jiang *et al.* [35] and A. Grüneis *et al.* [36] in our group. For graphene with different number of layers, a computational program for the G' band spectra is developed, based on the double resonance scattering theory. By considering the unit cell of double and triple layer graphene with the AB stacking of graphene layer [37,38], we calculate the electronic structure for each number of layers. As the result, the electronic two-linear band of single graphene layer around the Fermi level is split into two or three energy sub-bands by the interlayer interaction. The electronic structure of multi-layer graphene is applied to calculate their G' band Raman spectra. Our contributed work will be shown from Chapter 4. In Chapter 4, the calculated results for the Raman resonance windows for each (n, m) SWNT are directly compared with the experimental value which was obtained by Raman excitation profile (REP). For metallic SWNTs, we will discuss an additional contribution to the calculated resonance windows for explaining discrepancy with the experimental results. For example, the interaction of photo-excited carriers with free electrons might contribute to the Raman resonance window in metallic SWNTs. In Chapter 5, the calculated G' band intensities of metallic SWNTs are given. We will show the G' band intensity for metallic SWNTs are stronger than that of semiconducting SWNTs. This results are compared with the experimental G' band for SWNTs sample in which metallic SWNTs are removed from semiconducting SWNTs by oxidization of SWNTs. We will also explain the reason why the G' band intensity for the metallic SWNTs is stronger than that for the semiconducting SWNTs. In Chapter 6, we will show that the electronic band splitting near the Fermi level plays an important role in determining the G' band shape and intensity for double and triple layer graphenes. Finally, in Chapter 7, a summary and conclusion of this thesis are given.

1.3 Background

1.3.1 Synthesis of SWNTs

The full potential of carbon nanotubes for commercial applications will be realized if the growth of carbon nanotubes can be optimized and well controlled. Over the years, various techniques have been developed to commercially synthesize SWNTs in large quantities, including arc discharge [39], laser ablation [40], high pressure carbon monoxide (CO) decomposition (HiPCO) [41], and chemical vapor deposition (CVD) [42]. The arc discharge method is a convenient tool to vaporize carbon atoms in the high temperature of the plasma, which approaches 3700 °C [43], and it has been used to produce such structures as carbon whiskers [44], fullerenes [45], and carbon nanotubes. Typical conditions for the arc discharge method are that a DC voltage of $20 - 25$ V is applied between two carbon rod electrodes with $5 - 20$ mm diameter in a reactor chamber at a given helium pressure around 500 Torr and the negative electrode rod contains the catalyst such as Co, Ni, and Fe in order to grow the SWNTs in the chamber. The laser ablation method is an efficient technique for the synthesis of bundles of SWNTs with a narrow diameter distribution. Under the condition flowing Ar gas at 30 Torr in a heated glass tube (1200 °C), a pulse laser beam is irradiated on the graphite target containing a small amount of metal catalyst. The irradiation arises from the graphite and the catalyst to vaporize. Flowing Ar gas, the vaporized particles are swept away the copper collector and then the SWNTs with high yield are formed [40]. The HiPCO process produces SWNTs from gas-phase reactions of iron carbonyl ($Fe(CO)_5$) in carbon monoxide (CO) at high pressures ($10 - 100$ atm). In the HiPCO process, SWNTs are obtained with less graphitic deposits and amorphous carbon and the process has the potential for producing SWNTs in large quantities due to a gas-phase reaction [41]. The CVD method is highly promising for producing large quantities of high quality SWNT. The SWNT growth process involves heating a catalyst to high temperatures in a tube furnace and flowing a hydrocarbon gas through the tube reactor for a period of time. The key parameters in SWNT CVD growth are the type of hydrocarbon and catalyst, and the growth temperature. For example, by using CH_4 or C_2H_5OH as carbon source, the reaction temperature in the range of $850 - 1000$ °C, the suitable catalyst materials (Ni, Co, Fe), and the gas flow condition, one can easily grow high quality SWNTs by a simple CVD method [46, 47]. Recent interest in CVD SWNT growth is to synthesize the aligned and ordered SWNT structure on surfaces under some control such as temperature and flowing rate of hydrocarbon gas [48, 49]. The controlled SWNT growth techniques have opened up new routes building the SWNT structure at the specified location and allow the construction of novel SWNT electromechanical devices [50]. Perhaps, it is an ultimate goal for carbon nanotube growth to gain control over the SWNT chirality and diameter, and be able to direct the growth of a semiconducting or metallic nanotube from and to any desired direction. But, it is still difficult to reach with current synthesis techniques. On the other hand, the diameter of SWNTs can be controlled significantly by optimizing the growth temperature and the size of catalyst. Thus, we generally get a mixture of SWNTs with different chiralities and diameters.

1.3.2 Experimental Raman spectra of SWNT

Resonance Raman spectra of SWNTs can be obtained by using commercial micro-Raman spectrometers. Relatively high laser powers (up to 40 $\mathrm{mW} \cdot \mu\mathrm{m}^{-2}$) can be used to probe isolated SWNTs on substrate or in aqueous solution because of their high thermal conductivity (3 $\mathrm{W} \cdot \mathrm{K}^{-1}$) [51], their high temperature stability, and their good thermal contact to the substrate. A triple monochromator is ideal for the Raman measurements for changing the excitation laser energy continuously, but the obtained intensity decreases significantly compared with the intensity obtained from a single monochromator spectrometer. We usually adopt a notch filter for removing a strong Rayleigh scattering of the light for a single monochromator setup.

In Fig. 1.1 (page 4), we show characteristics of Raman spectra from both bundled (Fig. 1.1a) and isolated (Fig. 1.1b) SWNTs. The first order single resonance Raman spectra RBM and G band features are the most intense Raman peaks. The D and the G' bands are the second order double resonance Raman spectra, in which the D band is defect-induced Raman spectra and the G' band is an inelastic two-phonon Raman scattering of the light [7, 52–57]. The second order Raman spectra provide a large amount of important information about SWNT electronic and vibrational properties that cannot be obtained by analyzing the first order Raman spectra. We will focus on the second order double resonance Raman spectra, in particular, the G' band in this thesis. Other weak peaks, such as the M band (an overtone of out of plane tangential optic (oTO) mode, ∼1750 cm^{-1}) [7] and the iTOLA band (a combination of in-plane tangential optic(iTO) at the

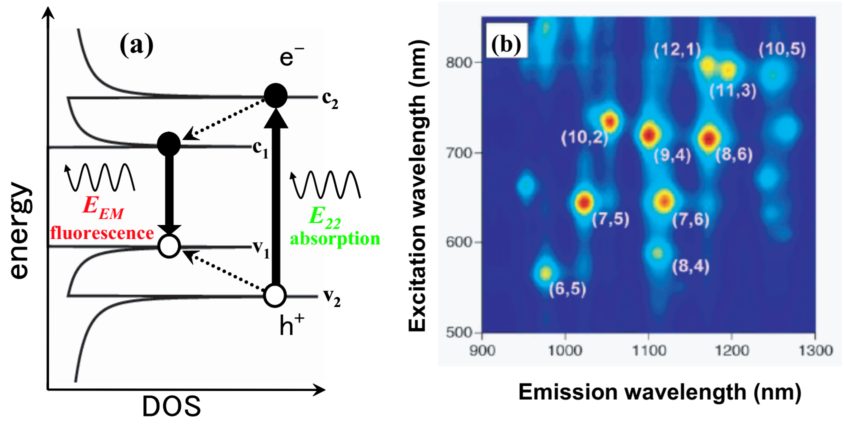

Figure 1.3: (a) Schematic electronic DOS in a SWNT. Bold solid arrows denote the optical excitation from second valence band v_2 to second conduction band c_2 and the emission (or fluorescence) from the first conduction band c_1 to the first valence band v_1, and dashed arrows denote the non-radiative relaxation of the electron in the conduction band ($c_2 \to c_1$) and the hole in the valence band ($v_2 \to v_1$) before the emission. (b) Contour plot of PL intensity versus excitation and emission wavelengths [58].

Γ point and in-plane longitudinal acoustic (iLA) modes, $\sim$1950 cm^{-1}) [7] also shown in Fig. 1.1, too. However, we will not discuss in this thesis.

1.3.3 Photoluminescence spectroscopy

Photoluminescence (PL) is a process in which a SWNT absorbs a photon and then emits a photon. Quantum mechanically, this process can be described as an excitation of an electron to a higher energy band and then a recombination with a hole by emitting a photon. The duration time between the absorption and the emission is typically in the order of 10 ns [59]. The wavelengths of light preferentially absorbed and emitted are determined by the selection rules for optical transition. Over the past few years, PL has become an important technique for the characterization of SWNTs [60]. The ability to probe the electronic structures of a large number of semiconducting SWNTs at the same time has made PL a complementary method to RRS for the characterization of SWNTs. In the most prior PL studies, the SWNT samples were dispersed in a surfactant solution, excited by a lamp source, and the PL spectra were recorded over the near and far IR spectral regions. Generally, in the most of studies, the strongly luminescent peaks are associated with a emission at E^S_{11} (from the first conduction band c_1 to the first valence band v_1, see Fig. 1.3 (a)) for different semiconducting SWNTs with a strong absorption at E^S_{22} (from the second conduction band c_2 to the second valence band v_2). A very fast ($<$ 1 ps) relaxation of the photo-excited carrier occurs by emitting a phonon from E^S_{22} to E^S_{11}, as shown in Fig. 1.3 (a). In Fig. 1.3 (b), a two-dimensional (2D) map for the PL intensity for a sample of HiPCO SWNTs suspended in SDS and deuterium oxide (D_2O) [58] is plotted as functions of absorption (E^S_{22}) wave-length ($y-$axis) and emission (E^S_{11}) wave-length ($x-$axis). Each strong peak in the 2D map corresponds to a (n, m) SWNT. We can see that the relative PL intensity depends on (n, m) value. It is because that (1) the population for (n, m) SWNTs is different [11] and that (2) the relative matrix elements of PL are strongly chirality dependent [12]. As for (2), we know that PL intensity is relatively strong for large chiral angle near armchair SWNTs [13].

1.4 Experimental background for this study

1.4.1 Resonance Raman window measurement

C. Fantini *et al.* as our collaborators measured the experimental resonance window for various samples at room temperature and at ambient pressure, using a DILOR XY triple-monochromator spectrometer in a backscattering configuration for measurement, equipped with a liquid N_2 cooled charge coupled device (CCD) [9], as shown in Fig 1.4. In Fig 1.4 (a), the 2D map of the Raman intensity is plotted as a function of the RBM frequency ($x-$axis) for 76 different excitation laser energies ($y-$axis). The samples were excited by a tunable laser system composed of a Ti:Sapphire laser, a dye laser, and an Ar-Kr ion laser, in the range 1.52 to 2.71 eV. Along a vertical line of the experimental 2D resonance Raman plot in Fig. 1.4 (a), we get experimental Raman excitation profile (REP) for the individual RBM features for different (n, m) SWNTs present in the sample (see Fig. 1.4 (b)). From these measurements, C. Fantini *et al.* obtained the experimental resonance window (γ_{EX}) values in the resonance Raman profiles as the spectral width of REP for individual (n, m) SWNTs. Experimental results reveal that the γ_{EX} value, representing the lifetime-broadening of the excitonic transition of an individual (n, m) SWNT, strongly depends on the environment of the (n, m) SWNT and on (n, m) values itself in a given sample, which suggests that electron-phonon (or exciton-phonon) coupling depends

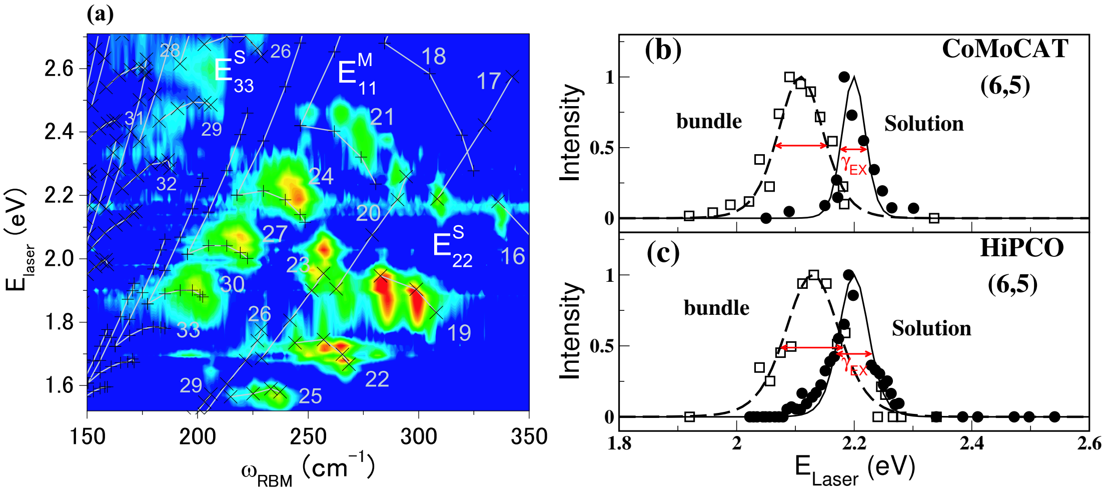

Figure 1.4: (a) The experimental 2D resonance Raman plot (the intensity increases from blue to red) compared with resonance points calculated by the extended tight binding method presented in a Kataura plot (+ for metallic and × for semiconducting nanotubes). SDS-wrapped HiPCO carbon nanotubes in solution were used in the experiment [9]. We can see that, for metallic nanotubes, the experimental peaks are related only to the lower transition energy (E_{11}^{ML}) in the extended Kataura plot. The numbers denote values of $2n+m$. The RBM intensity at 310 cm^{-1} is plotted as a function $E_{\rm L}$ for bundle SWNTs and for SDS wrapped (6,5) SWNTs in solution for (b) CoMoCAT and (c) HiPCO samples [61]. The experimental resonance window $\gamma_{\rm EX}$ are shown.

on the environment and (n, m) values.

In Fig. 1.4 (b-c), we show the REPs of the RBM at 310 cm^{-1} observed for (6,5) nanotubes in (b) CoMoCAT [62] and (c) HiPCO [41] samples. Solid circles and open squares denote SDS-wrapped SWNTs in solution and SWNTs within bundles, respectively. Solid and dashed lines represent the fit of the REPs to Eq. (1.1.1) for first order single resonance Raman scattering intensity $I(E_{\rm L})$. The matrix elements for optical absorption $M_{\rm el-op}$, electron-phonon coupling $M_{\rm el-ph}$, and optical emission $M_{\rm el-op}$ are taken as constants for the fitting. The spectra widths of the REPs correspond to the experimental resonance windows $\gamma_{\rm EX}$. In Chapter 3, we explain how to calculate the matrix elements, based on the electronic structure by the ETB method explained in Chapter 2. The optical matrix [36] and electron-phonon interaction matrix elements [12] were developed by A. Grüneis and J. Jiang, respectively, who had worked in our group. The

$\gamma_{\rm EX}$ value is determined by fitting the parameter γ of Eq. (1.1.1) to the experimental points. The fitting was performed not by Lorentzian functions but by making the integral in Eq. (1.1.1), and by considering the numerator as a $\delta-$function integrated in energy $\delta(E-(E_a-E_i))dE$ [9]. For the CoMoCAT nanotubes in solution, the REPs show a smaller resonance window than those for HiPCO nanotubes in solution. The $\gamma_{\rm EX}$ values of (6,5) nanotubes for HiPCO and CoMoCAT samples in solution are 63 meV and 40 meV, respectively. Moreover, the resonance window for SWNTs in solution is smaller than that for bundles, which means that there are more relaxation paths for the excited carriers in bundles. For example, the tube-tube interaction may make the carrier relaxation to other SWNTs possible. When we compare the REPs for HiPCO and CoMoCAT SWNTs in solution, we can see that there are minor differences (up to 80 meV) in the optical transition energies due to the environmental effects which gives rise to the shift of E_{ii} value by the surrounding materials of SWNTs [63]. It should be mentioned that the $\gamma_{\rm EX}$ for CoMoCAT SWNTs is not always smaller for all (n,m) tubes than the $\gamma_{\rm EX}$ for HiPCO SWNTs. Thus the 23 meV difference should be considered as a sample- and (n,m)-dependent deviation. We expect that the catalyst or the length of SWNT might not contribute to the resonance window very much because most of catalyst will be removed in the purification process and the electron-phonon scattering is also independent of the tube length. In Chapter 4, we will consider the γ value of isolated SWNTs. The calculated γ values for some (n,m) values are compared with the isolated SDS wrapped SWNTs in solution.

1.4.2 G' band measurement of SWNT

K. K. Kim *et al.* as our collaborators in Korea observed the dependence of the G' band intensity on the metallicity (being either metallic or semiconducting properties) of SWNTs by RRS with several excitation laser energies of 2.41 eV (514 nm, $\rm Ar^+$ ion laser), 1.96 eV (632.8 nm, He-Ne laser), and 1.58 eV (785 nm, diode laser) [23]. These measurements used HiPCO SWNTs sample with diameters ranging from 0.8 to 1.3 nm. For the observation of the metallicity dependence of the G' band intensity, the pristine HiPCO sample was treated by nitronium ions ($\rm NO_2^+$) to remove the metallic (m-) SWNTs. In this treatment, 10 mg of the pristine sample were sonicated for 24 hours in tetramethylene sulfone/chloroform (1:1 by weight) containing 50 mmol nitronium hexafluoroantimonate

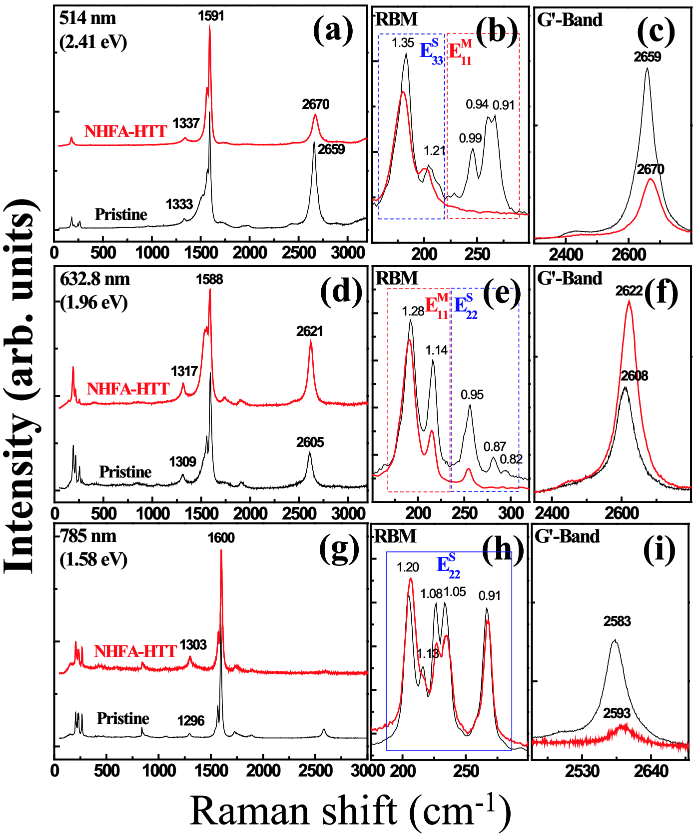

Figure 1.5: Raman spectra of the pristine HiPCO sample (black) and the NHFA-treated HiPCO sample (red) at an excitation energy of (a-c) 2.41 eV, (d-f) 1.96 eV, and (g-i) 1.58 eV. The NHFA-treated HiPCO sample was annealed at 900 °C. In Figures (b,e,f), the blue and red dotted regions indicate the semiconducting and metallic RBM frequency regions. The G' band intensity is normalized to the G band peak intensity [23].

(NHFA). While the semiconducting (s-) SWNTs with small diameter range ($<$ 1nm) remain after the chemical reaction, the m-SWNTs are removed by oxidation in the same diameter range as the s-SWNTs [24].

Figure 1.5 shows strong metallicity dependence of the G' band intensity of the HiPCO sample. The Raman spectra with excitation laser energy $E_{\mathrm{L}} = 2.41$ eV in Fig. 1.5 (a-c) show that the pristine HiPCO sample (black lines) consists of both m- and s-SWNTs by analyzing the RBM and G band. After the NHFA treatment followed by thermal annealing at 900 °C, the m-SWNTs with small diameters were removed completely, while the s-SWNTs still remained without damage (red lines). This observation was confirmed by the significant reduction in Breit-Wigner-Fano (BWF) component in the G band, as shown in Fig. 1.5(a,b). In m-SWNTs, the G band becomes soft and the spectra shows asymmetry around the peak position which can be fitted to BWF lines [64]. Then, the G' band for the NHFA-treated sample was significantly suppressed since the m-SWNTs were removed. If the m-SWNTs with a diameter approximately 0.94 nm were present in the NHFA-treated sample, a strong G' band intensity would be expected due to the scattering resonance condition for the G' band at E_{11}^{M}. This suggests that the dependence of the G' band intensity on the metallicity is dominated by the incident photon resonance of the s-SWNTs. In the case of $E_{\mathrm{L}} = 1.96$ eV in Fig. 1.5 (d-f), more m-SWNTs with large diameters ($>$ 1nm) remained in the sample, while the s-SWNTs with small diameters were removed after NHFA treatment. The BWF line for the NHFA treatment sample are stronger than that for the pristine sample due to the higher m-SWNT component which can be seen in RBM peak in the metallic resonance condition. In this case, the G' band intensity becomes stronger. For $E_{\mathrm{L}} = 1.58$ eV in Fig. 1.5 (g-f), the s-SWNTs can be resonant to E_{22}^{S} even after the NHFA treatment. The metallicity dependence of the G' band is not well recognized in this Raman spectra, because the its G' band intensity is much smaller than the G band intensity.

In Chapter 5, we will calculate the G' band intensity for m- and s-SWNT and explain the origin of the metallicity dependence of the G' band.

1.4.3 G' band measurement of multi-layer graphene

Finally, we introduce the G' band measurement of multi-layer graphene which is done by A. Reina in MIT as our collaborator. The graphene samples were prepared on Si substrates with a 300 nm SiO_2 over-layer following the procedure given in previous publications [28,31]. After graphene deposition by micro-mechanical cleavage [31], the substrates were inspected under an optical microscope and one to three layer (1L, 2L and 3L) graphene regions were identified by both color contrast in the optical microscope and the atomic force microscopy (AFM) height measurements, as shown in Fig. 1.2 (a) (page 5). The Raman spectra were taken with a homemade confocal Raman spectrometer with 7 laser excitation energies from 1.83 eV to 2.72 eV. The laser spot size is 0.5 μm^2 and the power of the laser is 1.5 mW at each excitation energy. Intensity calibration of the spectrometer, at each laser energy, was carried with a white tungsten lamp. The experimental spectra shown here are normalized with the G band intensity for each laser energy. Raman spectra of single, double, and triple layer graphenea at excitation laser energy $E_{\rm L} = 2.32$ eV are given in Fig. 1.2 (b). The width and peak position of the G' band become larger and blue-shifted with increasing number of graphene layers.

In Chapter 6, we will calculate the G' band spectra shape and intensity for multi-layer graphene.

Chapter 2

Geometry and electronic structure of SWNT

2.1 Geometry of SWNT

A carbon nanotube rolled up a single graphene sheet is called a single wall carbon nanotube (SWNT), and a carbon nanotube made of concentrically arranged cylinders rolled up several graphene sheets is referred to as a multi-wall carbon nanotube (MWNT). In this thesis, the SWNT is our main work.

This Section provides some basic definitions about the structure of SWNTs and the construction of one dimensional (1D) Brillouin zone of SWNT in relation to two dimensional (2D) Brillouin zone of graphene sheet. A carbon nanotube is a hollow cylinder of 2D graphene sheet. The structure of carbon nanotube has been investigated by the transmission electron microscopy (TEM) [1–3] and the scanning tunneling microscopy (STM) [65], yielding that the carbon nanotube is a seamless cylinder rolled up a graphene sheet with the honeycomb lattice. There are many ways to roll a graphene sheet into a cylindrical carbon nanotube, resulting in different diameter and helical structures of the nanotubes. These carbon nanotubes are defined by the diameter and the chiral angle which means the angle of the hexagon helix around the nanotube axis [5]. The physical properties of SWNTs significantly depend on the structure, including the electronic energy band structure, in particular, their metallic or semiconducting properties [4].

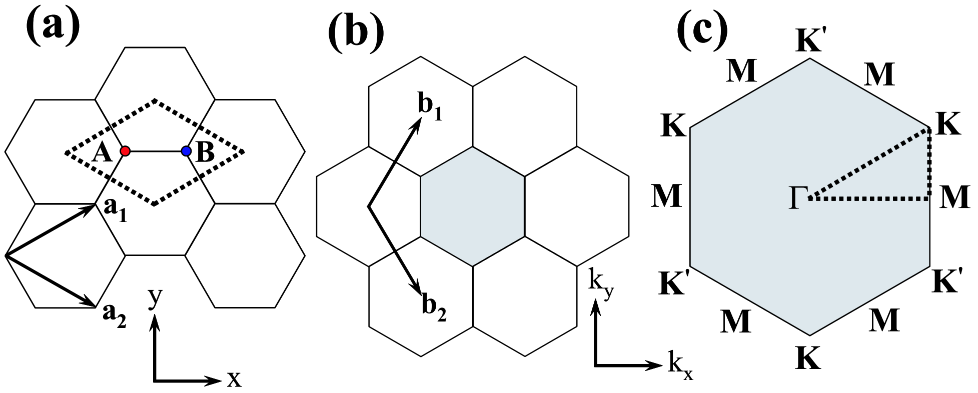

Figure 2.1: (a) The unit cell of graphene sheet is shown as the dotted rhombus. The red and blue dots in the dotted rhombus indicate the A and B sub-lattices, respectively. The real lattice unit vectors $\mathbf{a}_1$ and $\mathbf{a}_2$ are shown by arrows in the x, y coordinates system. (b) The first Brillouin zone is by a shaded region. The reciprocal lattice vectors $\mathbf{b}_1$ and $\mathbf{b}_2$ are shown by arrows in the k_x, k_y coordinates. (c) The first Billouin zone of (b). Γ, K, K', and M indicate the high symmetry points. In general, energy dispersion relations are obtained along the side of the dotted triangle connecting the high symmetry points, Γ, K and M [5].

2.1.1 Graphene is 2D

Graphene is one atomic layer of graphite. The nearest neighbor distance between two carbon atoms in the graphene sheet is 0.142 nm (a_{CC}). The unit cell and the Brillouin zone of graphene are expressed, respectively, by $\mathbf{a}_1$ and $\mathbf{a}_2$ unit vectors in real space, and by $\mathbf{b}_1$ and $\mathbf{b}_2$ reciprocal lattice vectors in the k space as shown in Fig. 2.1. In real space, the unit vectors $\mathbf{a}_1$ and $\mathbf{a}_2$ are given by:

$$\begin{cases} \mathbf{a}_1 = \dfrac{\sqrt{3}a}{2}\hat{\mathbf{x}} + \dfrac{a}{2}\hat{\mathbf{y}}, \\ \mathbf{a}_2 = \dfrac{\sqrt{3}a}{2}\hat{\mathbf{x}} - \dfrac{a}{2}\hat{\mathbf{y}}, \end{cases} \tag{2.1.1}$$

where $a = \sqrt{3}a_{\mathrm{CC}} = 0.246$ nm is the lattice constant of graphene sheet. $\hat{\mathbf{x}}$ and $\hat{\mathbf{y}}$ are the unit vectors in x and y directions of graphene sheet, respectively. These two unit vectors $\mathbf{a}_1$ and $\mathbf{a}_2$ make an angle 60° in Fig. 2.1 (a). The reciprocal lattice vectors $\mathbf{b}_1$ and $\mathbf{b}_2$ are related to the real space vectors $\mathbf{a}_1$ and $\mathbf{a}_2$ according to following definition:

$$\mathbf{a}_i \cdot \mathbf{b}_j = 2\pi\delta_{ij}, \tag{2.1.2}$$

where δ_{ij} is the Kronecker delta function. Therefore, the reciprocal unit vectors $\mathbf{b}_1$ and $\mathbf{b}_2$ are given by:

$$\begin{cases} \mathbf{b}_1 = \dfrac{2\pi}{\sqrt{3}a}\hat{\mathbf{x}} + \dfrac{2\pi}{a}\hat{\mathbf{y}}, \\ \mathbf{b}_2 = \dfrac{2\pi}{\sqrt{3}a}\hat{\mathbf{x}} - \dfrac{2\pi}{a}\hat{\mathbf{y}}, \end{cases} \tag{2.1.3}$$

where the unit vectors $\mathbf{b}_1$ and $\mathbf{b}_2$ make an angle 120° in Fig. 2.1 (b). These reciprocal lattice unit vectors define the first Brillouin zone of the graphene sheet and then, the first Brillouin zone has the same hexagon shape as the real space unit cell, but the hexagon orientation is different by 90° from each other. In the Brillouin zone as shown in Fig. 2.1 (c), we define three high symmetry points, Γ, K, and M as the center, the hexagonal corner, and the center of a hexagon side, respectively. In general, the energy dispersion of the graphene sheet is calculated for the electron wave vectors on the ΓKM triangle, as shown in Fig. 2.1 (c).

2.1.2 1D unit cell

The structure of a SWNT is conveniently described in terms of its 1D unit cell [5]. The 1D unit cell is defined by the chiral vector $\mathbf{C}_h$ and the translation vector $\mathbf{T}$, as shown in Fig. 2.2. The chiral vector $\mathbf{C}_h$ can be represented by the 2D graphene unit vectors $\mathbf{a}_1$ and $\mathbf{a}_2$ in Eq. (2.1.1):

$$\mathbf{C}_h = n\mathbf{a}_1 + m\mathbf{a}_2 \equiv (n, m), \tag{2.1.4}$$

where (n, m) is a pair of integers uniquely defining the particular structure of SWNT $(n \geq m)$. Many properties of SWNTs such like their electronic band or phonon structures change dramatically with the chiral vector, even though they have similar diameter or similar chiral vector direction [5]. Figure 2.2 shows the unit cell of SWNT with the chiral vector $\mathbf{C}_h = (4, 2)$, and the chiral angle θ between the chiral vector $\mathbf{C}_h$ and the *zigzag* direction $(\theta = 0)$, and the unit vector $\mathbf{a}_1$ and $\mathbf{a}_2$ of the graphene sheet. The chiral angle θ is given by:

$$\theta = \tan^{-1}\Big(\frac{\sqrt{3}n}{2m + n}\Big). \tag{2.1.5}$$

Therefore, the zigzag $(n, 0)$ and armchair (n, n) nanotubes correspond to chiral angle $\theta = 0$ and 30°, respectively, and the chiral (n, m) nanotubes correspond to $0 < \theta < 30°$.

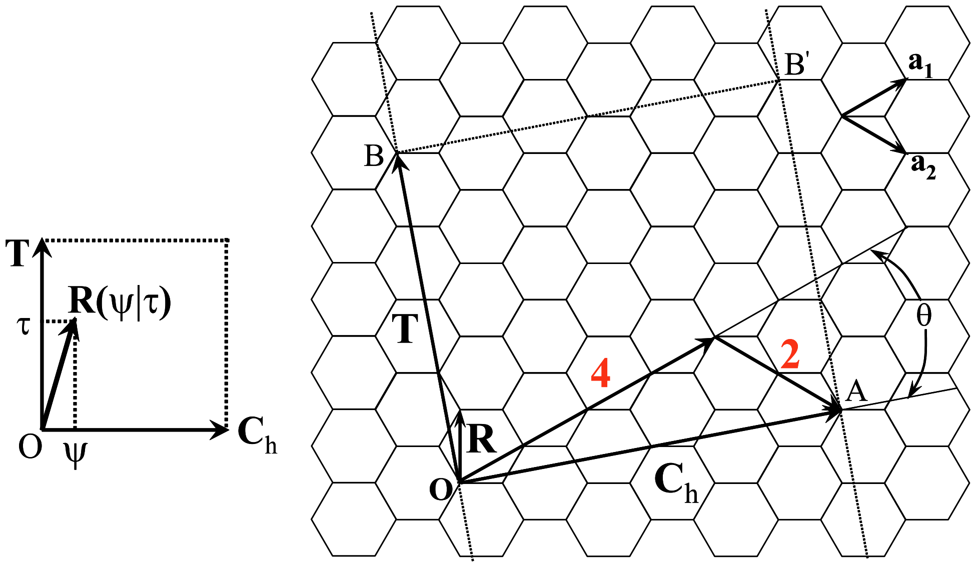

Figure 2.2: (right) The unrolled graphene sheet of nanotube. **OA** and **OB** define the chiral vector $\mathbf{C}_h$ and the translation vector $\mathbf{T}$ of the SWNT, respectively. Here $\mathbf{C}_h = (4, 2)$, $\mathbf{T} = (4, -5)$. The chiral angle θ is the angle between $\mathbf{a}_1$ and $\mathbf{C}_h$. Therefore, the chiral angle $\theta = 0$ along the zigzag axis. When we connect four sites O, A, B', and B, a SWNT can be constructed. The rectangle $OAB'B$ defines the 1D SWNT unit cell. The vector $\mathbf{R}$ indicates a symmetry vector; $\mathbf{R} = (1, -1)$. (left) The rotation angel ψ and the translation τ constitute the basic symmetry operation $R = (\psi|\tau)$ for the SWNT. The number of hexagons per unit cell of the SWNT is denoted by N. For (4,2) SWNT, $N = 28$ [5].

The diameter d_t of a (n, m) SWNT is given by:

$$d_t = \frac{C_h}{\pi} = \frac{a}{\pi}\sqrt{n^2 + nm + m^2}, \tag{2.1.6}$$

where C_h is the length of chiral vector $\mathbf{C}_h$, and $a = \sqrt{3}a_{\mathrm{CC}}$.

The translation vector $\mathbf{T}$ is normal to the chiral vector $\mathbf{C}_h$ and is parallel to the nanotube axis in the unrolled graphene sheet. The translation vector $\mathbf{T}$ corresponds to the vector $\overrightarrow{OB}$ (which is normal to $\mathbf{C}_h$) with the first lattice point B and can be expressed by unit vectors $\mathbf{a}_1$ and $\mathbf{a}_2$:

$$\mathbf{T} = t_1\mathbf{a}_1 + t_2\mathbf{a}_2 \equiv (t_1, t_2), \tag{2.1.7}$$

where t_1 and t_2 are obtained by using the condition $\mathbf{C}_h \cdot \mathbf{T} = 0$:

$$\begin{cases} t_1 = \dfrac{2m+n}{d_R}, \\[2ex] t_2 = -\dfrac{2n+m}{d_R}, \end{cases} \tag{2.1.8}$$

where $d_R = \gcd(2n+m, 2m+n)$, and $\gcd(i,j)$ denotes the greatest common divisor of two integers i and j. The quantity d_R is obtained by repeated use of Euclid's law which $\gcd(i,j)$ $=\gcd(i-j,j)$ if $i > j$. Namely, the quantity $d = \gcd(n,m)$ defined by the chiral vector $\mathbf{C}_h$ is related to $d_R = \gcd(2n+m, 2m+n)$ introduced in the translation vector $\mathbf{T}$:

$$\begin{cases} d = \gcd(n,m) = \gcd(n-m,m), \\[2ex] d_R = \gcd(2n+m,2m+n) = \gcd(n-m,2m+n) = \gcd(n-m,3m). \end{cases} \tag{2.1.9}$$

Then, we can relate d_R to d:

$$d_R = \begin{cases} d, & \text{if } \operatorname{mod}(n-m,3d) \neq 0, \\[2ex] 3d, & \text{if } \operatorname{mod}(n-m,3d) = 0, \end{cases} \tag{2.1.10}$$

where $\operatorname{mod}(i,j)$ is the remainder (or modulus) of the division of i by j. The unit cell of the SWNT is defined by the chiral vector $\mathbf{C}_h$ and the translation vector $\mathbf{T}$. The area of the SWNT unit cell is given by the absolute value of the vector product of $\mathbf{C}_h$ and $\mathbf{T}$, $\left|\mathbf{C}_h \times \mathbf{T}\right|$. The number of hexagons per unit cell of the SWNT, N is obtained by dividing the area of the SWNT unit cell by the area of the hexagonal unit cell in the graphene sheet, $\left|\mathbf{a}_1 \times \mathbf{a}_2\right|$, of Fig. 2.1:

$$N = \frac{\left|\mathbf{C}_h \times \mathbf{T}\right|}{\left|\mathbf{a}_1 \times \mathbf{a}_2\right|} = \frac{2(n^2+nm+m^2)}{d_R}. \tag{2.1.11}$$

Consequently, $(4,2)$ SWNT in Fig. 2.2 has $d_R = d = 2$, $\mathbf{T} = (4,-5)$, and $N = 28$. The length of the translation vector T is given by:

$$T = |\mathbf{T}| = \frac{\sqrt{3}a}{d_R}\sqrt{n^2+nm+m^2} = \frac{\sqrt{3}C_h}{d_R}. \tag{2.1.12}$$

The translational length T is significantly diminished when $\gcd(n,m) \neq 1$. For example, in the case of $(9,9)$ armchair nanotube, we have $d_R = 3d = 27$, $\mathbf{T} = (1,-1)$, and $N = 18$ and for $(9,0)$ zigzag nanotube, $d_R = 9$, $\mathbf{T} = (1,-2)$, and $N = 18$, while for $(9,8)$ chiral nanotube, $d_R = d = 1$, $\mathbf{T} = (25,-26)$, and $N = 434$.

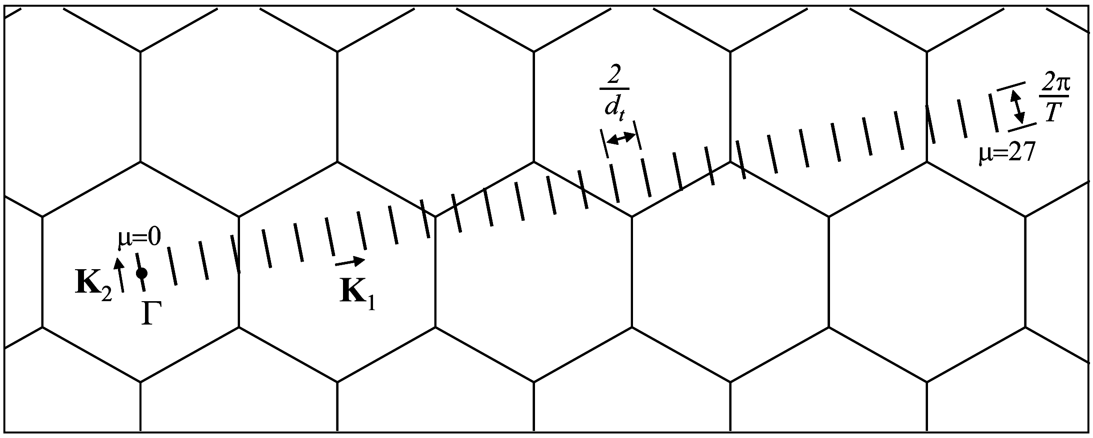

Figure 2.3: The Brillouin zone of (4,2) SWNT is represented by the set of $N = 28$ parallel cutting lines. The vector $\mathbf{K}_1$ and $\mathbf{K}_2$ are the reciprocal lattice vectors which correspond to $\mathbf{C}_h$ and $\mathbf{T}$, respectively. The cutting lines are labeled by the angular momentum index μ, which defines integer values from 0 to $N-1 = 27$. The length of cutting line is defined by $2\pi/T = 2\pi/\sqrt{21}a$, where $a = \sqrt{3}a_{\mathrm{CC}} = 0.246$ nm [5].

2.1.3 Cutting line

In Section 2.1.2, we determined the unit cell of SWNT, and in this section, we construct 1D Brillouin zone of a SWNT. Along the circumference vector $\mathbf{C}_h$ of the SWNT, any allowed wave vector $\mathbf{k}$ is quantized according to the periodic boundary condition. The wave function of an electron of the SWNT has a boundary-condition-satisfied phase of an integer multiple of 2π for the circumference vector $\mathbf{C}_h$:

$$\mathbf{k} \cdot \mathbf{C}_h = 2\pi\mu, \tag{2.1.13}$$

where μ is the angular momentum of standing wave in the SWNT and is an integer from $\mu = 0$ to $N-1$. In terms of the 2D Brillouin zone of graphene sheet, the allowed electronic states $\mathbf{k}$ lie along parallel lines separated by a spacing of $2\pi/C_h = 2/d_t$. These lines are called to cutting lines [66, 67]. Whereas the 1D unit cell of SWNT in the real space is expressed by the chiral vector $\mathbf{C}_h$ and the translation vector $\mathbf{T}$, the corresponding vectors of SWNT in reciprocal space are the reciprocal lattice vectors $\mathbf{K}_1$ along the circumferential direction and $\mathbf{K}_2$ along the nanotube axis. Therefore, by using the relations, $\mathbf{R}_i \cdot \mathbf{K}_j = 2\pi\delta_{ij}$, between the real lattice vector $\mathbf{R}_i$ (= $\mathbf{C}_h$ or $\mathbf{T}$) and the reciprocal lattice vector $\mathbf{K}_j$, the reciprocal lattice vector of SWNT, $\mathbf{K}_1$ and $\mathbf{K}_2$ are defined by:

$$\begin{cases} \mathbf{T}\cdot\mathbf{K}_1 = 0, \quad \mathbf{C}_h\cdot\mathbf{K}_1 = 2\pi, \\ \mathbf{C}_h\cdot\mathbf{K}_2 = 0, \quad \mathbf{T}\cdot\mathbf{K}_2 = 2\pi. \end{cases} \tag{2.1.14}$$

We substitute $\mathbf{C}_h$ and $\mathbf{T}$ from Eqs. (2.1.4) and (2.1.7) into Eq. (2.1.14), and then we express $\mathbf{a}_1$ and $\mathbf{a}_2$ in $\mathbf{K}_1$ and $\mathbf{K}_2$ as $\mathbf{b}_1$ and $\mathbf{b}_2$ by comparing Eqs. (2.1.1) and (2.1.3):

$$\begin{cases} \mathbf{K}_1 = \dfrac{-t_2\mathbf{b}_1 + t_1\mathbf{b}_2}{N}, \\ \mathbf{K}_2 = \dfrac{m\mathbf{b}_1 - n\mathbf{b}_2}{N}, \end{cases} \tag{2.1.15}$$

The reciprocal lattice vectors, $\mathbf{K}_1$ and $\mathbf{K}_2$ define the separation between the neighboring cutting lines, and the length of the cutting lines, respectively. The magnitudes of $\mathbf{K}_1$ and $\mathbf{K}_2$ are given by:

$$\left|\mathbf{K}_1\right| = \frac{2\pi}{C_h} = \frac{2}{d_t}, \quad \left|\mathbf{K}_2\right| = \frac{2\pi}{T}, \tag{2.1.16}$$

Therefore, the N parallel cutting lines are related to discrete value of the angular momentum μ in Eq. (2.1.13) and the length of the cutting line $\left|\mathbf{K}_2\right|$ determines the periodicity of the 1D momentum k that has continuous wave vector in the $\mathbf{K}_2$ direction for an infinite SWNT length because of the translational symmetry of the vector $\mathbf{T}$. The allowed wave vector $\mathbf{k}$ of a SWNT takes the following form:

$$\mathbf{k} = \mu\mathbf{K}_1 + k\frac{\mathbf{K}_2}{K_2}, \tag{2.1.17}$$

where $\mu = 0, \cdots, N-1$, and $k = -\pi/T < k < \pi/T$. The unit cell of the SWNT has N hexagons, and then the first Brillouin zone of the SWNT consists of N cutting lines. In Fig. 2.3, the reciprocal lattice vectors, $\mathbf{K}_1$ and $\mathbf{K}_2$, for a (4,2) chiral SWNT are shown, in which $N = 28$, $\mathbf{K}_1 = (3\sqrt{3}, 1)\pi/14a$, and $\mathbf{K}_2 = (1/\sqrt{3}, 3)\pi/7a$. For the N cutting lines, N 1D energy bands for each 2D energy band and N 1D phonon dispersions for each phonon mode will appear. The wave vectors in the $\mathbf{K}_2$ direction for a SWNT with infinite tube length are continuous because of its translational symmetry, but, for a SWNT with finite tube length L, the spacing between wave vectors is $2\pi/L$, and its effect on energy band was observed in experiment [68].

2.2 Electronic structure

2.2.1 Electronic structure of graphene

Next, we review a simple tight-binding (STB) model that plays an important role to understand the electronic structure of a graphene sheet and a SWNT. The electronic structure of a SWNT using STB model is derived from that of graphene. For obtaining a good agreement with recent optical experiments, we have to extend the STB model by including the long-range atomic interactions and the σ molecular orbitals, and by optimizing the geometrical structure. The resulting model is hereafter called to extended tight-binding (ETB) model, which we explain below.

In graphene, the π electrons in $2p_z$ orbital are valence electrons which are relevant to the transport and other optical properties. The π electron has an energy band structure near the Fermi energy, so that electrons can be optically excited from the valence (π) to the conduction (π^*) band.

The electronic energy dispersion relations of a graphene are obtained by solving the single particle Schrodinger equation:

$$\hat{H}\Psi^b(\mathbf{k},\mathbf{r},t) = i\hbar\frac{\partial}{\partial t}\Psi^b(\mathbf{k},\mathbf{r},t), \tag{2.2.1}$$

where the single-particle Hamiltonian operator $\hat{H}$ is given by the following expression:

$$\hat{H} = -\frac{\hbar^2}{2m}\nabla^2 + U(\mathbf{r}), \tag{2.2.2}$$

where ∇ is the gradient operator, $\hbar$ is the Plank's constant, m is the electron mass, $U(\mathbf{r})$ is the effective periodic potential, $\Psi^b(\mathbf{k},\mathbf{r},t)$ is one electron wave function, b $(= 1, 2, ..., 8)$ is the electron energy band index, $\mathbf{k}$ is the electron wave vector, $\mathbf{r}$ is the spatial coordinate, and t is time. The one electron wave function $\Psi^b(\mathbf{k},\mathbf{r},t)$ is constructed from four atomic orbitals, $2s$, $2p_x$, $2p_y$, and $2p_z$, for the two inequivalent carbon atoms at A and B in the unit cell of graphene as shown Fig. 2.1 (a), and is approximated by a linear combination of atomic orbitals (LCAO) in terms of Bloch wave function [69]:

$$\Psi^b(\mathbf{k},\mathbf{r},t) = e^{iE^b(\mathbf{k})t/\hbar}\sum_{s}^{A,B}\sum_{o}^{2s,\ldots,2p_z} C^b_{so}(\mathbf{k})\Phi_{so}(\mathbf{k},\mathbf{r}), \tag{2.2.3}$$

where $E^b(\mathbf{k})$ is the one electron energy, the C^b_{so} is the wave function coefficient for the Bloch function $\Phi_{so}(\mathbf{k},\mathbf{r})$. The Bloch wave function $\Phi_{so}(\mathbf{k},\mathbf{r})$ is given by a sum over the atomic wave function $\phi_o(\mathbf{r})$ for each orbital at the u-th unit cell in a graphene sheet:

$$\Phi_{so}(\mathbf{k},\mathbf{r}) = \frac{1}{\sqrt{U}} \sum_{u}^{U} e^{i\mathbf{k}\cdot\mathbf{R}_{us}} \phi_o(\mathbf{r}-\mathbf{R}_{us}), \tag{2.2.4}$$

where the index u $(= 1, ..., U)$ spans all the U unit cells in a graphene sheet and $\mathbf{R}_{us}$ is the atomic coordinate for the $u-$th unit cell and $s-$th atom. Since the electron wave functions $\Psi^b(\mathbf{k},\mathbf{r},t)$ should also satisfy Bloch's theorem, the summation in Eq. (2.2.3) is taken only for the Bloch wave function $\Phi_{so}(\mathbf{k},\mathbf{r})$ with the same value of $\mathbf{k}$. The eigenvalue $E^b(\mathbf{k})$ as a function of $\mathbf{k}$ is given by:

$$E^b(\mathbf{k}) = \frac{\langle \Psi(\mathbf{k})|\hat{H}|\Psi(\mathbf{k})\rangle}{\langle \Psi(\mathbf{k})|\Psi(\mathbf{k})\rangle}. \tag{2.2.5}$$

Substituting Eq. (2.2.3) into Eq. (2.2.5), we obtain the following equation:

$$E^b(\mathbf{k}) = \frac{\displaystyle\sum_{s'o'}\sum_{so} C^{b*}_{s'o'}(\mathbf{k}) H_{s'o'so}(\mathbf{k}) C^b_{so}(\mathbf{k})}{\displaystyle\sum_{s'o'}\sum_{so} C^{b*}_{s'o'}(\mathbf{k}) S_{s'o'so}(\mathbf{k}) C^b_{so}(\mathbf{k})}, \tag{2.2.6}$$

where the transfer integral $H_{s'o'so}(\mathbf{k})$ and overlap integral $S_{s'o'so}(\mathbf{k})$ matrices are given by:

$$\begin{aligned} H_{s'o'so}(\mathbf{k}) &= \frac{1}{U}\sum_{u}^{U} e^{i\mathbf{k}\cdot(\mathbf{R}_{us}-\mathbf{R}_{u's'})} \int \phi^*_{o'}(\mathbf{r}-\mathbf{R}_{u's'}) H \phi_o(\mathbf{r}-\mathbf{R}_{us}) d\mathbf{r}, \\ S_{s'o'so}(\mathbf{k}) &= \frac{1}{U}\sum_{u}^{U} e^{i\mathbf{k}\cdot(\mathbf{R}_{us}-\mathbf{R}_{u's'})} \int \phi^*_{o'}(\mathbf{r}-\mathbf{R}_{u's'}) \phi_o(\mathbf{r}-\mathbf{R}_{us}) d\mathbf{r}. \end{aligned} \tag{2.2.7}$$

When we fix the values of the $n \times n$ $(n = 8)$ matrices $H_{s'o'so}(\mathbf{k})$ and $S_{s'o'so}(\mathbf{k})$ in Eq. (2.2.7) for a given electron wave vector $\mathbf{k}$, the wave function coefficient $C^{b*}_{s'o'}(\mathbf{k})$ is optimized so as to minimize $E^b(\mathbf{k})$. The coefficient $C^{b*}_{s'o'}(\mathbf{k})$ as a function of $\mathbf{k}$ is a complex variable with a real and a complex part, and both $C^{b*}_{s'o'}(\mathbf{k})$ and $C^b_{so}(\mathbf{k})$ are independent each other. Taking a partial derivative for $C^{b*}_{s'o'}(\mathbf{k})$ while fixing the coefficient $C^b_{so}(\mathbf{k})$, we can get the variational condition for finding the minimum of the ground state energy [5]:

$$\frac{\partial E^b(\mathbf{k})}{\partial C^{b*}_{s'o'}(\mathbf{k})} = 0. \tag{2.2.8}$$

By substituting the ground state energy $E^b(\mathbf{k})$ from Eq. (2.2.5) into Eq. (2.2.8), Eq.

(2.2.8) becomes:

$$\begin{aligned}\frac{\partial E^b(\mathbf{k})}{\partial C^{b*}_{s'o'}(\mathbf{k})} &= \frac{\sum\limits_{so} H_{s'o'so}(\mathbf{k})C^b_{so}(\mathbf{k})}{\sum\limits_{s'o'}\sum\limits_{so} C^{b*}_{s'o'}(\mathbf{k})S_{s'o'so}(\mathbf{k})C^b_{so}(\mathbf{k})} \\ &\quad - \frac{\sum\limits_{s'o'}\sum\limits_{so} C^{b*}_{s'o'}(\mathbf{k})H_{s'o'so}(\mathbf{k})C^b_{so}(\mathbf{k})}{\Big(\sum\limits_{s'o'}\sum\limits_{so} C^{b*}_{s'o'}(\mathbf{k})S_{s'o'so}(\mathbf{k})C^b_{so}(\mathbf{k})\Big)^2}\sum_{so} S_{s'o'so}(\mathbf{k})C^b_{so}(\mathbf{k}) \\ &= \frac{\sum\limits_{so} H_{s'o'so}(\mathbf{k})C^b_{so}(\mathbf{k}) - E^b(\mathbf{k})\sum\limits_{so} S_{s'o'so}(\mathbf{k})C^b_{so}(\mathbf{k})}{\sum\limits_{s'o'}\sum\limits_{so} C^{b*}_{s'o'}(\mathbf{k})S_{s'o'so}(\mathbf{k})C^b_{so}(\mathbf{k})} \\ &= 0,\end{aligned} \tag{2.2.9}$$

and then upon multiplying both side of Eq. (2.2.9) by $\sum\limits_{s'o'}\sum\limits_{so} C^{b*}_{s'o'}(\mathbf{k})S_{s'o'so}(\mathbf{k})C^b_{so}(\mathbf{k})$, we can obtain simple following equation:

$$\sum_{so} H_{s'o'so}(\mathbf{k})C^b_{so}(\mathbf{k}) - E^b(\mathbf{k})\sum_{so} S_{s'o'so}(\mathbf{k})C^b_{so}(\mathbf{k}) = 0. \tag{2.2.10}$$

Eq. (2.2.10) is expressed by a matrix form when we define the $C^b_{so}(\mathbf{k})$ as a column vector:

$$\begin{aligned}\Big(H(\mathbf{k}) - E^b(\mathbf{k})S(\mathbf{k})\Big)C^b(\mathbf{k}) = 0, \\ C^b(\mathbf{k}) = \begin{pmatrix} C^b_{2s^A} \\ \vdots \\ C^b_{2p_z^B}\end{pmatrix}, (b = 1, \cdots, 8).\end{aligned} \tag{2.2.11}$$

The eigenvalues of $H_{s'o'so}(\mathbf{k})$ are calculated by solving the following secular equation for each $\mathbf{k}$:

$$\det\Big[H(\mathbf{k}) - E^b(\mathbf{k})S(\mathbf{k})\Big] = 0, \tag{2.2.12}$$

where Eq. (2.2.12) gives eight eigenvalues of $E^b(\mathbf{k})$ for the energy band index $b = 1, \cdots, 8$ for a given electron wave vector $\mathbf{k}$. Considering four atomic orbitals per one carbon atom $(2s, 2p_x, 2p_y, 2p_z)$ and two carbon atomic site (A, B) per unit cell of a graphene sheet, we obtain the 8×8 Hamiltonian $H_{s'o'so}(\mathbf{k})$ and overlap $S_{s'o'so}(\mathbf{k})$ matrices, and then these matrices are expressed by 2×2 sub-matrix for two sub-atoms:

$$H(\mathbf{k}) = \begin{pmatrix} H_{AA}(\mathbf{k}) & H_{AB}(\mathbf{k}) \\ H_{BA}(\mathbf{k}) & H_{BB}(\mathbf{k})\end{pmatrix} \text{ and } S(\mathbf{k}) = \begin{pmatrix} S_{AA}(\mathbf{k}) & S_{AB}(\mathbf{k}) \\ S_{BA}(\mathbf{k}) & S_{BB}(\mathbf{k})\end{pmatrix}, \tag{2.2.13}$$

where H_{AA} (H_{BB}) and H_{AB} (H_{BA}) are expressed by 4×4 sub-matrix for four orbitals. The matrix elements between $2p_z$ orbital and $2s$, $2p_x$, and $2p_y$ are zero because of the odd (even) function $2p_z$ ($2s$, $2p_x$, and $2p_y$) of z for the both cases of H_{AA} (H_{BB}) and H_{AB} (H_{BA}):

$$\begin{aligned}
H_{AA}(\mathbf{k}) &= \begin{pmatrix} \langle 2s^A|H|2s^A\rangle & \langle 2s^A|H|2p_x^A\rangle & \langle 2s^A|H|2p_y^A\rangle & \langle 2s^A|H|2p_z^A\rangle \\ \langle 2p_x^A|H|2s^A\rangle & \langle 2p_x^A|H|2p_x^A\rangle & \langle 2p_x^A|H|2p_y^A\rangle & \langle 2p_x^A|H|2p_z^A\rangle \\ \langle 2p_y^A|H|2s^A\rangle & \langle 2p_y^A|H|2p_x^A\rangle & \langle 2p_y^A|H|2p_y^A\rangle & \langle 2p_y^A|H|2p_z^A\rangle \\ \langle 2p_z^A|H|2s^A\rangle & \langle 2p_z^A|H|2p_x^A\rangle & \langle 2p_z^A|H|2p_y^A\rangle & \langle 2p_z^A|H|2p_z^A\rangle \end{pmatrix} \\
&= \begin{pmatrix} \langle 2s^A|H|2s^A\rangle & 0 & 0 & 0 \\ 0 & \langle 2p_x^A|H|2p_x^A\rangle & 0 & 0 \\ 0 & 0 & \langle 2p_y^A|H|2p_y^A\rangle & 0 \\ 0 & 0 & 0 & \langle 2p_z^A|H|2p_z^A\rangle \end{pmatrix} \\
&= H_{BB}(\mathbf{k}),
\end{aligned} \tag{2.2.14}$$

$$\begin{aligned}
H_{AB}(\mathbf{k}) &= \begin{pmatrix} \langle 2s^A|H|2s^B\rangle & \langle 2s^A|H|2p_x^B\rangle & \langle 2s^A|H|2p_y^B\rangle & \langle 2s^A|H|2p_z^B\rangle \\ \langle 2p_x^A|H|2s^B\rangle & \langle 2p_x^A|H|2p_x^B\rangle & \langle 2p_x^A|H|2p_y^B\rangle & \langle 2p_x^A|H|2p_z^B\rangle \\ \langle 2p_y^A|H|2s^A\rangle & \langle 2p_y^A|H|2p_x^A\rangle & \langle 2p_y^A|H|2p_y^B\rangle & \langle 2p_y^A|H|2p_z^B\rangle \\ \langle 2p_z^A|H|2s^A\rangle & \langle 2p_z^A|H|2p_x^B\rangle & \langle 2p_z^A|H|2p_y^B\rangle & \langle 2p_z^A|H|2p_z^B\rangle \end{pmatrix} \\
&= \begin{pmatrix} \langle 2s^A|H|2s^B\rangle & \langle 2s^A|H|2p_x^B\rangle & \langle 2s^A|H|2p_y^B\rangle & 0 \\ \langle 2p_x^A|H|2s^B\rangle & \langle 2p_x^A|H|2p_x^B\rangle & \langle 2p_x^A|H|2p_y^B\rangle & 0 \\ \langle 2p_y^A|H|2s^A\rangle & \langle 2p_y^A|H|2p_x^A\rangle & \langle 2p_y^A|H|2p_y^B\rangle & 0 \\ 0 & 0 & 0 & \langle 2p_z^A|H|2p_z^B\rangle \end{pmatrix} \\
&= {}^T H_{BA}^*(\mathbf{k}).
\end{aligned}$$

In a flat graphene sheet, these matrices are partitioned into the 6×6 and 2×2 sub-matrices corresponding to the σ and π molecular orbitals, respectively, because the atomic orbital $2s$, $2p_x$, and $2p_y$ are even functions of z, which parallel to the graphene sheet, while the $2p_z$ orbital is an odd function of z.

The STB model neglects the σ molecular orbitals and the long-range atomic interactions, $R > a_{\text{CC}}$. Therefore, in the STB model, we solve for the 2×2 sub-matrix to determine the dispersion relation $E^b(\mathbf{k})$ and the electron wave function coefficients for the π electrons in a flat graphene sheet. When we consider only nearest-neighbor interactions, there is only an integration over a single atom in $H_{AA}(\mathbf{k})$ and $H_{BB}(\mathbf{k})$, and then these 2×2 matrix Hamiltonians are obtained by Eq. (2.2.7) [5]:

$$\begin{aligned} H_{AA}(\mathbf{k}) &= \frac{1}{U}\sum_{u}^{U} e^{i\mathbf{k}\cdot(\mathbf{R}_{uA}-\mathbf{R}_{u'A})}\int \phi_\pi^*(\mathbf{r}-\mathbf{R}_{u'A})H\phi_\pi(\mathbf{r}-\mathbf{R}_{uA})d\mathbf{r} \\ &= \frac{1}{U}\sum_{u=u'}^{U}\varepsilon_{2p} + \frac{1}{U}\sum_{R_{uA}=R_{u'A}\pm a}^{U} e^{\pm ika}\int \phi_\pi^*(\mathbf{r}-\mathbf{R}_{u'A})H\phi_\pi(\mathbf{r}-\mathbf{R}_{uA})d\mathbf{r} \\ &\quad +(\text{terms equal to or more distance than } R_{uA}=R_{u'A}\pm 2a) \\ &= \varepsilon_{2p} + (\text{terms equal to or more distance than } R_{uA}=R_{u'A}\pm a), \end{aligned} \tag{2.2.15}$$

where the maximum contribution to the matrix element $H_{AA}(\mathbf{k})$ comes from $u = u'$, and this gives the orbital energy of the $2p$ level, ε_{2p}. The next order is neglected for simplicity. The absence of nearest-neighbor interactions within the same unit cell atom A or B yields the diagonal Hamiltonian and overlap matrix elements, $H_{AA}(\mathbf{k}) = H_{BB}(\mathbf{k}) = \varepsilon_{2p}$ and $S_{AA}(\mathbf{k}) = S_{BB}(\mathbf{k}) = 1$. For the $H_{AB}(\mathbf{k})$ and the $S_{AB}(\mathbf{k})$ matrix elements, the inter-atomic vectors $\mathbf{R}_A^n$ from A atom site to its three nearest-neighbor B atoms ($n = 1, 2, 3$) in Eq. (2.2.7) are given as follows:

$$\mathbf{R}_A^1 = \Big(\frac{1}{\sqrt{3}}, 0\Big)a, \quad \mathbf{R}_A^2 = \Big(-\frac{1}{2\sqrt{3}}, \frac{1}{2}\Big)a, \quad \mathbf{R}_A^3 = \Big(-\frac{1}{2\sqrt{3}}, -\frac{1}{2}\Big)a, \tag{2.2.16}$$

where a is the lattice constant of a graphene sheet. Similarly, the inter-atomic vector $\mathbf{R}_B^n$ is defined to $\mathbf{R}_A^n$ with minus sign, $\mathbf{R}_A^n = -\mathbf{R}_B^n$. Substituting these vectors into Eq. (2.2.7), we obtain the matrix elements:

$$\begin{aligned} H_{AB}(\mathbf{k}) &= \frac{1}{U}\sum_{u}^{U} e^{i\mathbf{k}\cdot(\mathbf{R}_{uB}-\mathbf{R}_{u'A})}\int \phi_\pi^*(\mathbf{r}-\mathbf{R}_{u'A})H\phi_\pi(\mathbf{r}-\mathbf{R}_{uB})d\mathbf{r} \\ &= t\sum_{n}^{3} e^{i\mathbf{k}\cdot\mathbf{R}_A^n} \\ &= tf(\mathbf{k}), \end{aligned} \tag{2.2.17}$$

$$\begin{aligned} S_{AB}(\mathbf{k}) &= \frac{1}{U}\sum_{u}^{U} e^{i\mathbf{k}\cdot(\mathbf{R}_{uB}-\mathbf{R}_{u'A})}\int \phi_\pi^*(\mathbf{r}-\mathbf{R}_{u'A})\phi_\pi(\mathbf{r}-\mathbf{R}_{uB})d\mathbf{r} \\ &= s\sum_{n}^{3} e^{i\mathbf{k}\cdot\mathbf{R}_A^n} \\ &= sf(\mathbf{k}), \end{aligned}$$

where t is transfer integral, s is the overlap integral between the nearest-neighbor A and B atoms, and $f(\mathbf{k})$ is defined by starting from an A atom and going out to the three nearest-neighbor B atoms:

$$\begin{aligned} t &= \int \phi_\pi^*(\mathbf{r} - \mathbf{R}_{u'A}) H \phi_\pi(\mathbf{r} - \mathbf{R}_{uB}) d\mathbf{r}, \\ s &= \int \phi_\pi^*(\mathbf{r} - \mathbf{R}_{u'A}) \phi_\pi(\mathbf{r} - \mathbf{R}_{uB}) d\mathbf{r}, \\ f(\mathbf{k}) &= e^{ik_x a/\sqrt{3}} + 2e^{-ik_x a/2\sqrt{3}} \cos\Big(\frac{k_y a}{2}\Big). \end{aligned} \tag{2.2.18}$$

The $H_{BA}(\mathbf{k})$ and $S_{BA}(\mathbf{k})$ matrix elements are derived in a similar method to inter-atomic vector $\mathbf{R}_B^n$ from B atom site to its three nearest-neighbor A atoms, that is, $H_{BA}(\mathbf{k}) = tf^*(\mathbf{k})$, and $S_{BA}(\mathbf{k}) = sf^*(\mathbf{k})$. It is note that the $H(\mathbf{k})$ and $S(\mathbf{k})$ are Hermite matrices. Therefore, the secular equation Eq. (2.2.12) for $H(\mathbf{k})$ and $S(\mathbf{k})$ can be written as the explicit forms:

$$\begin{pmatrix} \varepsilon_{2p} & tf(\mathbf{k}) \\ tf^*(\mathbf{k}) & \varepsilon_{2p} \end{pmatrix} \begin{pmatrix} C_{A\pi}^b(\mathbf{k}) \\ C_{B\pi}^b(\mathbf{k}) \end{pmatrix} = E^b(\mathbf{k}) \begin{pmatrix} 1 & sf(\mathbf{k}) \\ sf^*(\mathbf{k}) & 1 \end{pmatrix} \begin{pmatrix} C_{A\pi}^b(\mathbf{k}) \\ C_{B\pi}^b(\mathbf{k}) \end{pmatrix}. \tag{2.2.19}$$

Solving the secular equation Eq. (2.2.12), the eigenvalues $E^b(\mathbf{k})$ are obtained as a function of $w(\mathbf{k})$:

$$\begin{vmatrix} \varepsilon_{2p} - E^b(\mathbf{k}) & f(\mathbf{k})\Big(t - sE^b(\mathbf{k})\Big) \\ f^*(\mathbf{k})\Big(t - sE^b(\mathbf{k})\Big) & \varepsilon_{2p} - E^b(\mathbf{k}) \end{vmatrix} = 0, \tag{2.2.20}$$

and then we get:

$$\begin{cases} E^v(\mathbf{k}) = \dfrac{\varepsilon_{2p} + tw(\mathbf{k})}{1 + sw(\mathbf{k})}, \\ E^c(\mathbf{k}) = \dfrac{\varepsilon_{2p} - tw(\mathbf{k})}{1 - sw(\mathbf{k})}, \end{cases} \tag{2.2.21}$$

where the band indexes $b = v, c$ denote the valence and conduction bands, t is negative ($t < 0$), s is positive ($s > 0$), and $w(\mathbf{k})$ is the absolute value of the phase factor $f(\mathbf{k})$,

$$w(\mathbf{k}) = \sqrt{|f(\mathbf{k})|^2} = \sqrt{1 + 4\cos\Big(\frac{\sqrt{3}}{2}k_x a\Big)\cos\Big(\frac{1}{2}k_y a\Big) + 4\cos^2\Big(\frac{1}{2}k_y a\Big)}. \tag{2.2.22}$$

The overlap integral s is responsible for the asymmetry between the valence and conduction energy bands. When the overlap integral s becomes zero ($s = 0$), the valence and conduction bands become symmetrical around $E = \varepsilon_{2p}$ which can be understood from Eq. (2.2.21).

Substituting the energy eigenvalues $E^b(\mathbf{k})$ of Eq. (2.2.21), the wave function coefficients $C_A^b(\mathbf{k})$ and $C_B^b(\mathbf{k})$ for the energy bands $b = v, c$ are yielded:

$$\begin{cases} \Big(\varepsilon_{2p} - E^b(\mathbf{k})\Big) C_A^b(\mathbf{k}) + f(\mathbf{k})\Big(t - sE^b(\mathbf{k})\Big) C_B^b(\mathbf{k}) = 0, \\ f^*(\mathbf{k})\Big(t - sE^b(\mathbf{k})\Big) C_A^b(\mathbf{k}) + \Big(\varepsilon_{2p} - E^b(\mathbf{k})\Big) C_B^b(\mathbf{k}) = 0, \end{cases}$$

therefore,

$$\begin{cases} C_A^v(\mathbf{k}) = \dfrac{f(\mathbf{k})}{w(\mathbf{k})} C_B^v(\mathbf{k}) \ , \ C_B^v(\mathbf{k}) = \dfrac{f^*(\mathbf{k})}{w(\mathbf{k})} C_A^v(\mathbf{k}) \text{ for } b = v, \\ C_A^c(\mathbf{k}) = -\dfrac{f(\mathbf{k})}{w(\mathbf{k})} C_A^c(\mathbf{k}) \ , \ C_B^c(\mathbf{k}) = -\dfrac{f^*(\mathbf{k})}{w(\mathbf{k})} C_A^c(\mathbf{k}) \text{ for } b = c. \end{cases} \tag{2.2.23}$$

The orthonormal conditions for the electron wave function of Eq. (2.2.3) can be expanded in terms of Bloch wave functions:

$$\begin{aligned} &\langle \Psi^{b'}(\mathbf{k}, \mathbf{r}, t) | \Psi^b(\mathbf{k}, \mathbf{r}, t) \rangle \\ &= \sum_{s'}^{A,B} \sum_{s}^{A,B} C_{s'}^{b'^*}(\mathbf{k}) C_s^b(\mathbf{k}) S_{s's}(\mathbf{k}) \\ &= C_A^{b'^*}(\mathbf{k}) C_A^b(\mathbf{k}) + sf(\mathbf{k}) C_A^{b'^*}(\mathbf{k}) C_B^b(\mathbf{k}) + sf^*(\mathbf{k}) C_B^{b'^*}(\mathbf{k}) C_A^b(\mathbf{k}) + C_B^{b'^*}(\mathbf{k}) C_B^b(\mathbf{k}) \\ &= \delta_{b'b}, \ (b', b = v, c). \end{aligned} \tag{2.2.24}$$

Thus, we obtain the wave function coefficients $C_A^b(\mathbf{k})$ and $C_B^b(\mathbf{k})$ for π electrons which are related to each other by complex conjugation, for valence band $b = v$,

$$C_A^v(\mathbf{k}) = \sqrt{\frac{f(\mathbf{k})}{2w(\mathbf{k})(1 + sw(\mathbf{k}))}} \ , \ C_B^v(\mathbf{k}) = \sqrt{\frac{f^*(\mathbf{k})}{2w(\mathbf{k})(1 + sw(\mathbf{k}))}}, \tag{2.2.25}$$

for conduction band $b = c$,

$$C_A^c(\mathbf{k}) = \sqrt{\frac{f(\mathbf{k})}{2w(\mathbf{k})(1 - sw(\mathbf{k}))}} \ , \ C_B^c(\mathbf{k}) = -\sqrt{\frac{f^*(\mathbf{k})}{2w(\mathbf{k})(1 - sw(\mathbf{k}))}}. \tag{2.2.26}$$

In order to reproduce the first principle calculation for the energy dispersion relations of the graphene sheet [70], we use the parameters, that is, the transfer integral $t = -3.033$ eV, and overlap integral $s = 0.129$, after setting the atomic orbital energy equal to the origin ($\varepsilon_{2p} = 0$) in the energy scale [5], as shown in Fig. 2.4.

The wave function formation for the valence and conduction electrons can be understood from the Bloch wave function coefficients given by Eqs. (2.2.25) and (2.2.26) and

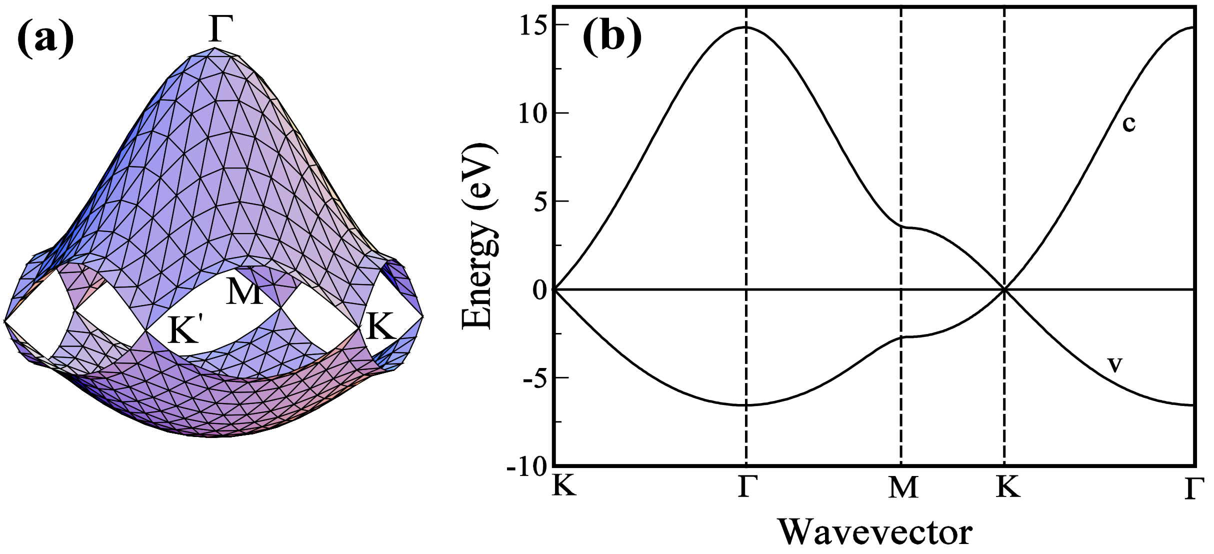

Figure 2.4: Electronic energy dispersion relations of a graphene sheet given by Eq. (2.2.21) with STB parameters, transfer integral $t = -3.033$ eV, overlap integral $s = 0.129$ eV, and atomic orbital energy $\varepsilon_{2p} = 0$ eV, (a) for the whole region of the Brillouin zone and (b) along the high symmetry direction of $K - \Gamma - M - K - \Gamma$ (Fig. 2.1 (c)). The valence and conduction bands are labeled by v and c, respectively [5].

the phase factor of $f(\mathbf{k})$. At the Γ point ($\mathbf{k} = 0$), $C_A^v = C_B^v$, while $C_A^c = -C_B^c$. Therefore, the wave functions become $\Psi^v(\mathbf{r}) = \Phi_A(\mathbf{r}) + \Phi_B(\mathbf{r})$ and $\Psi^c(\mathbf{r}) = \Phi_A(\mathbf{r}) - \Phi_B(\mathbf{r})$. Away from the Γ point ($\mathbf{k} \neq 0$), the Bloch wave functions, $\Phi_A(\mathbf{k}, \mathbf{r})$ and $\Phi_B(\mathbf{k}, \mathbf{r})$, have different phase factor, $f(\mathbf{k})$. At the K point, if $f(\mathbf{k}) = 0$, we get $\Psi^b(\mathbf{r}) = \Phi_A(\mathbf{r})$ or $\pm\Phi_B(\mathbf{r})$, where $\pm$ corresponds to the energy bands $b = v$ and $b = c$, respectively.

The energy band structure of a graphene sheet has a linear dispersion relation around the K and K' points near the Fermi level. Around the K point in the first Brillouin zone, the electron wave vector $\mathbf{k}$ is written to the form $k_x = \Delta k_x$ and $k_y = -4\pi/(3a) + \Delta k_y$, where $\Delta k_x, \Delta k_y \ll 1/a$. Substituting these wave vectors into Eq. (2.2.22) and approximating the cosine function up to the second order in the Maclaurin series as functions of $\Delta k_x a$ and $\Delta k_y a$, we can obtain w as a function of Δk (distance from the K

point),

$$\begin{aligned} w(\mathbf{k}) &= \sqrt{1+4\cos\Big(\frac{\sqrt{3}}{2}\Delta k_x a\Big)\cos\Big(-\frac{2}{3}\pi+\frac{1}{2}\Delta k_y a\Big)+4\cos^2\Big(-\frac{2}{3}\pi+\frac{1}{2}\Delta k_y a\Big)} \\ &\approx \frac{\sqrt{3}}{2}\Delta k a,\ \Big(\Delta k=\sqrt{\Delta k_x^2+\Delta k_y^2}\ ,\ \cos x = 1-\frac{x^2}{2!}+\frac{x^4}{4!}-\frac{x^6}{6!}+\cdots\Big), \end{aligned} \tag{2.2.27}$$

and then the energy dispersion relations for the valence and conduction bands are yielded by substituting w into Eq. (2.2.21):

$$\begin{cases} E^v(\Delta k) = \varepsilon_{2p} - \dfrac{\sqrt{3}}{2}(\varepsilon_{2p}s - t)a\Delta k, \\ E^c(\Delta k) = \varepsilon_{2p} + \dfrac{\sqrt{3}}{2}(\varepsilon_{2p}s - t)a\Delta k. \end{cases} \tag{2.2.28}$$

Eq. (2.2.28) shows that the energy band for the valence and conduction band are linear in Δk. The density of electronic states (DOS) at Fermi level is zero, indicating that a graphene sheet is a zero-gap semiconductor. The DOS is proportional to $|E|$, because of linear energy dispersion relation.

2.2.2 Electronic structure of SWNT

The electronic structure of a SWNT is derived by the STB calculation for the π electrons of carbon atoms, using the definition of the structure of SWNTs discussed in Section 2.1. We discussed the energy band structure of a graphene sheet in detail in Section 2.2.1, because the electronic structure of a SWNT is obtained simply from that of the graphene sheet.

The allowed wave vectors $\mathbf{k}$, cutting lines [66, 67], around the carbon nanotube circumference (the chiral vector $\mathbf{C}_h$ direction) become quantized (see Eq. (2.1.17)), taking only discrete values. Along the nanotube axis (the direction of the translational vector $\mathbf{T}$), in contrast, the cutting lines are continuous for a nanotube of infinite length(see Eq. (2.1.17)). The real lattice of the SWNT is formed by rolling the real lattice of a graphene sheet, therefore the reciprocal lattice of the SWNT is obtained by folding the reciprocal lattice of the graphene sheet. This is called to *zone-folding approximation* [5, 71]. The basic idea of the zone-folding method is that the energy dispersion relations of a SWNT is given by the corresponding energy dispersion relations of the graphene sheet along the

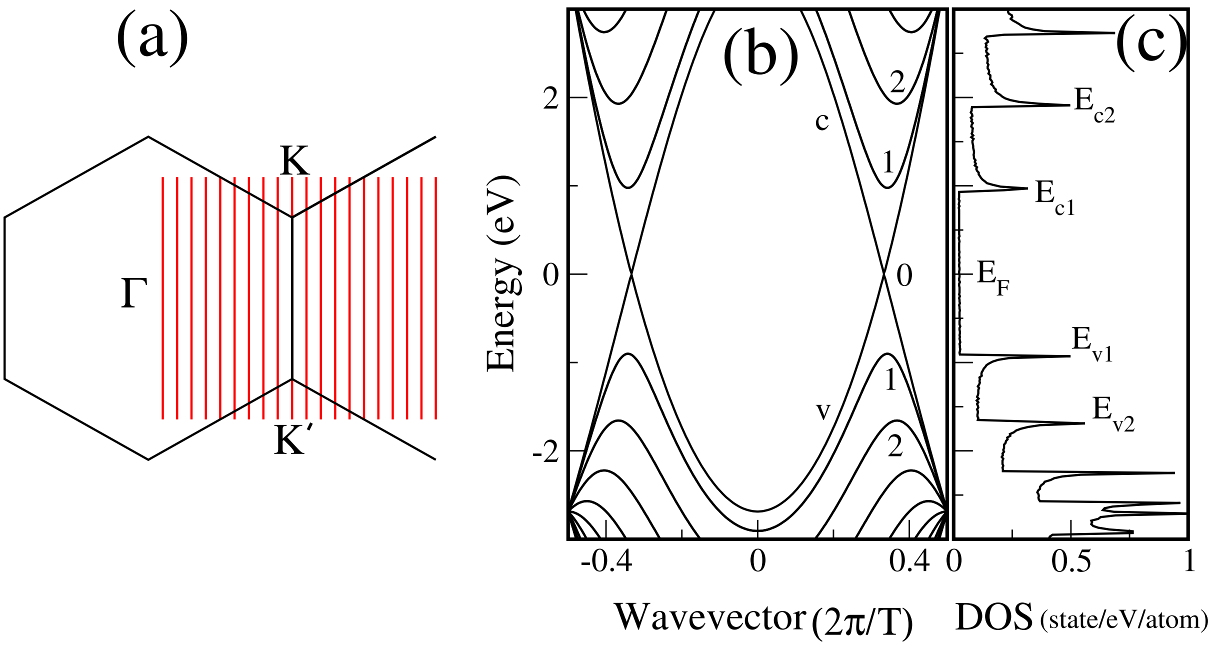

Figure 2.5: (a) Cutting lines of the (10,10) SWNT. One of red cutting lines passes through K and K' points of the Brillouin zone of a graphene sheet. (b) The energy dispersion relations of the (10,10) SWNT when the different cutting lines are folded together into the 1D Brillouin zone. The length of the 1D Brillouin zone is $2\pi/T$. The energy sub-bands are labeled by band index $b = v, c$ and by sub-band number i progressively increasing away from the Fermi level. (c) The electronic density of states (DOS) for the (10,10) SWNT. A finite DOS at Fermi level $E_F = 0$ eV indicates that the (10,10) SWNT is metallic. The sharp spikes in the DOS as a function of energy are known as van Hove singularities (vHSs). The vHSs associated with different sub-band edges are labeled by E_{bi}.

cutting lines. This zone-folding technique for SWNTs is also applicable to the phonon modes and other quasi-particle excitations.

A good example to see the power of zone-folding method is the metallic and semiconducting properties of the SWNTs. While 2/3 of SWNTs are semiconductors, the rest 1/3 are metallic or small-gap semiconducting [4]. This peculiar property is explained by the energy band structure of the graphene sheet. Since the valence and conduction bands of the graphene touch to each other at the K point of the Brillouin zone, if the K point of the graphene lies on the allowed states of a SWNT, it is metallic. Otherwise, the SWNT is semiconducting with a moderate energy gap. When the 1D cutting lines

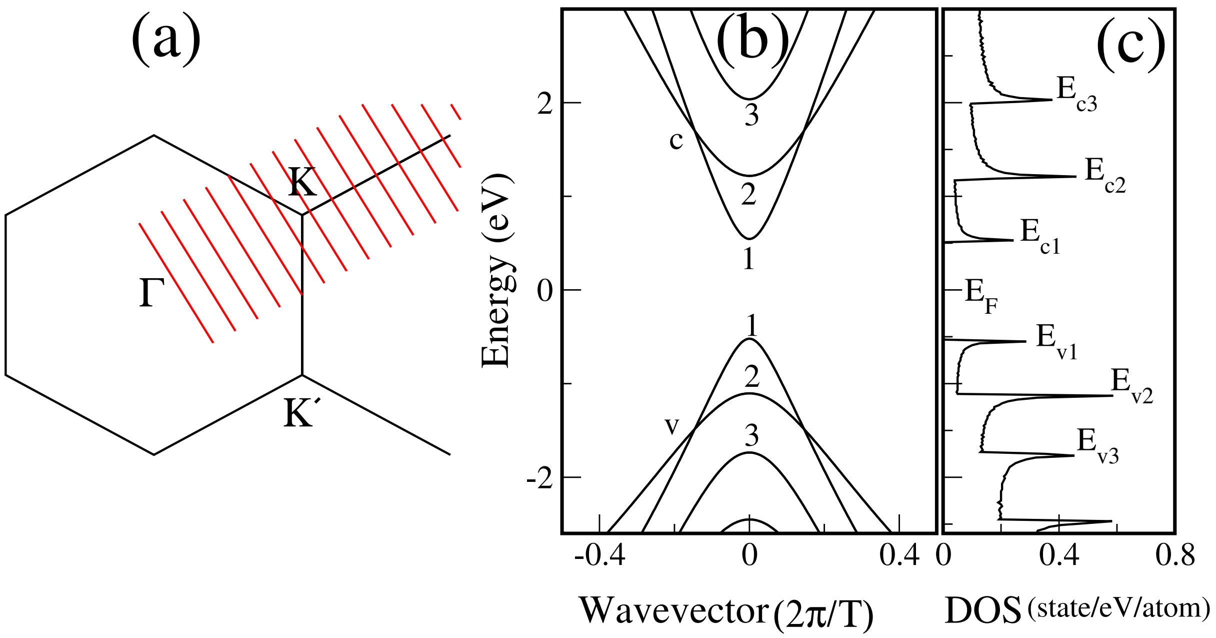

Figure 2.6: (a) Cutting lines of the (10,0) SWNT. None of red cutting lines passes through K or K' point of the 2D Brillouin zone. (b) The energy dispersion relations of the (10,0) SWNT. The energy sub-bands are labeled by band index $b = v, c$ and by sub-band number i progressively increasing away from the Fermi level. (c) The electronic DOS of the (10,0) SWNT. Vanishing DOS at the Fermi level $E_F = 0$ eV indicates that the (10,0) SWNT is semiconducting. The vHSs associated with different sub-band edges are labeled by E_{bi}.

$\mu\mathbf{K}_1 + k\mathbf{K}_2/|\mathbf{K}_2|$ of a SWNT in Eq. (2.1.17) are superimposed on the 2D electronic energy dispersion surface of the graphene sheet in Eq. (2.2.21), N pairs of energy dispersion relations $E^b_{\mathrm{SWNT}}(\mu, k)$ of SWNT are obtained:

$$E^b_{\mathrm{SWNT}}(\mu, k) = E^b_{\mathrm{2D}}\Big(\mu\mathbf{K}_1 + k\frac{\mathbf{K}_2}{|\mathbf{K}_2|}\Big), \ \Big(\mu = 0, \cdots, N-1, -\frac{\pi}{T} < k < \frac{\pi}{T}\Big), \qquad (2.2.29)$$

where μ is the angular momentum of a standing wave in the SWNT, which shows how many nodes of the wave function exhibit along the circumference of the SWNT [72], N is the number of hexagons in the translational unit cell of the SWNT as explained in Section 2.1, k is the 1D momentum along the SWNT axis, and $T = |\mathbf{T}|$ is the length of a SWNT translation. For a particular (n, m) SWNT, if a cutting line passes through a K or K' point of the Brillouin zone of the graphene sheet, where the valence and conduction bands of the graphene touch to each other, the 1D electronic energy bands of the SWNT have a zero energy gap, and therefore, they become metallic (DOS at E_{F} is finite), as shown in Fig. 2.5. However, if a cutting line does not pass through a K or K' point, the (n,m) SWNT is semiconducting with a finite energy band gap, as shown in Fig. 2.6.

The electronic states are restricted to the 1D wave vector $\mathbf{k}$ in the graphene sheet that fulfills the condition $\mathbf{k}\cdot\mathbf{C}_h = 2\pi\mu$ that the ratio of the length of the circumference $|\mathbf{C}_h|$ to an electron wave length $\lambda = 2\pi/k = |\mathbf{C}_h|/\mu$ around the circumference of the SWNT must be an integer. For the particular SWNT $(4,2)$, the K point is not allowed for any $\mathbf{k}$ and then, the SWNT $(4,2)$ becomes semiconducting. The K point of the Brillouin zone of the graphene is at $(2\mathbf{b}_1+\mathbf{b}_2)/3$, defining as $\mathbf{K}$. The $\mathbf{b}_1$ and $\mathbf{b}_2$ are the reciprocal lattice vectors of the grapheen sheet as explained in Section 2.1. Thus, a SWNT (n,m) is a metallic if the 1D momentum $\mathbf{k}$ is equal to K point;

$$\begin{aligned}\mathbf{k}\cdot\mathbf{C}_h &= \mathbf{K}\cdot\mathbf{C}_h\\ &= \frac{(2\mathbf{b}_1+\mathbf{b}_2)}{3}\cdot(n\mathbf{a}_1+m\mathbf{a}_2)\\ &= \frac{2}{3}(2n+m)\pi\\ &= 2\pi\mu,\end{aligned} \tag{2.2.30}$$

that is,

$$2n+m = 3\mu, \tag{2.2.31}$$

where μ is an integer. Therefore, we find that a SWNT (n,m) is metallic if $\mathrm{mod}(2n+m,3)=0$ and otherwise semiconducting, where $\mathrm{mod}(x,y)$ is the residual of the division of x by y, as shown in Fig. 2.7. The latter condition, $\mathrm{mod}(2n+m,3)$ =1 and 2, shows that there are twice as many semiconducting SWNTs as metallic SWNTs.

If we project the ΓK vector pointing toward the K point on the $\mathbf{K}_1$ direction normal to the cutting lines, we can find the projection:

$$\begin{aligned}\frac{\Gamma K\cdot\mathbf{K}_1}{\mathbf{K}_1\cdot\mathbf{K}_1} &= \frac{\frac{1}{3}(2\mathbf{b}_1+\mathbf{b}_2)\cdot\frac{1}{N}(t_1\mathbf{b}_2-t_2\mathbf{b}_1)}{\frac{1}{N}(t_1\mathbf{b}_2-t_2\mathbf{b}_1)\cdot\frac{1}{N}(t_1\mathbf{b}_2-t_2\mathbf{b}_1)}\\ &= \frac{2n+m}{3},\end{aligned} \tag{2.2.32}$$

where $N = 2(n^2+nm+m_2)/d_R$, $t_1 = (2m+n)/d_R$, $t_2 = -(2n+m)/d_R$, d_R=gcd$(2n+m, 2m+n)$, and the function gcd(i,j) denotes the greatest common divisor of the two integers i and j. If $(2n+m)/3$ is an integer, ΓK has an integer number of $\mathbf{K}_1$ components, and then one of the cutting lines passes through the K point, that is, this SWNT is metallic. If $(2n+m)/3$ is not an integer, namely the residual is 1 or 2, the K point exists

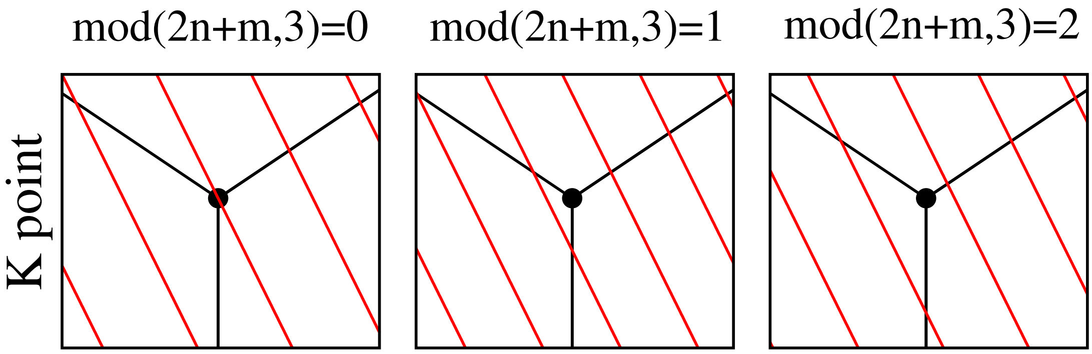

Figure 2.7: Three possible configurations of the cutting lines in the vicinity of the K point depending on the value of $\mathrm{mod}(2n+m,3)$. The red lines indicate the cutting lines, the black solid dot shows the K point, and the black lines represent the KM directions. If $\mathrm{mod}(2n+m,3)=0$, a SWNT is metallic ($M0$), if $\mathrm{mod}(2n+m,3)=1$ or 2, a SWNT is semiconducting ($S1$) or ($S2$).

1/3 or 2/3 position between two cutting lines near the K point, and then the SWNT becomes semiconducting [66, 67]. Thus, these three types of SWNTs are referred to as $M0$, $S1$, and $S2$, respectively:

$$\begin{aligned} \mathrm{mod}(2n+m,3) &= 0 \Rightarrow M0 \\ \mathrm{mod}(2n+m,3) &= 1 \Rightarrow S1 \\ \mathrm{mod}(2n+m,3) &= 2 \Rightarrow S2. \end{aligned} \tag{2.2.33}$$

In Figure 2.8, the chiral vectors for $M0$, $S1$, and $S2$ SWNTs are shown with different color, white, violet, and light cyan, respectively. Within the triangular graphene sheet, the diagonal lines of each hexagon are connected to a diagonal lines of the adjacent hexagons, which are shown as the dashed red lines in Fig. 2.8, and then these lines with constant value of $2n+m$, $2m+n$, and $n-m$ are called the family lines. All $M0$, $S1$, and $S2$ SWNTs along the same dashed line in Fig. 2.8 can be said to belong to the same family. For example, a SWNT with the chiral vector $(6,2)$ belongs to families, $2n+m=14$, $2m+n=10$, and $n-m=4$, as shown in Fig. 2.8. The (n,m) SWNTs with the same family constant $2n+m=14$ are (7,0), (6,2), and (5,4) and for $2m+n=10$, there are (10,0), (8,1), (6,2), and (4,3) and for $n-m=4$, there are (4,0), (5,1), (6,2), and (7,3). These SWNTs are semiconducting and can be classified to $S2$ type, since $\mathrm{mod}(2n+m,3)=\mathrm{mod}(14,3)=2$. However, for the same SWNT (6,2), $\mathrm{mod}(2m+n,3)=\mathrm{mod}(10,3)=1$

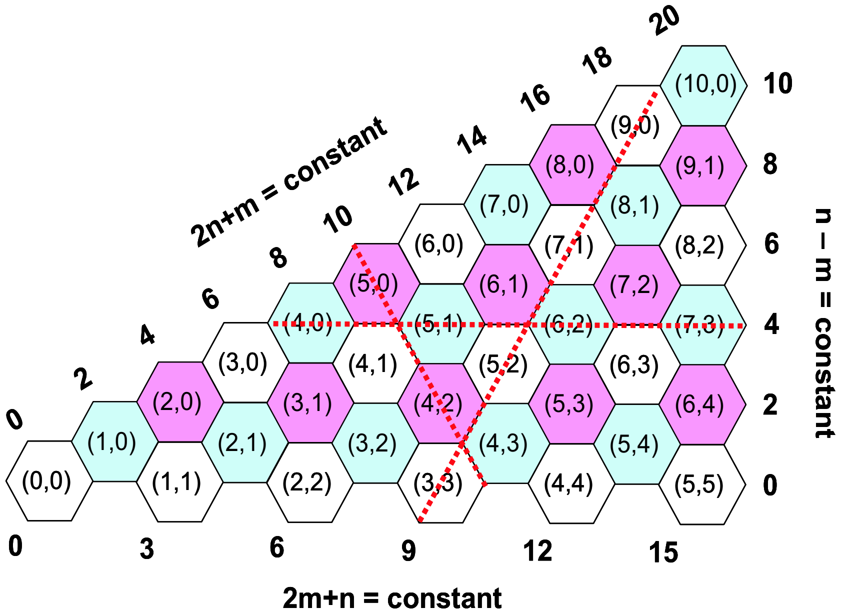

Figure 2.8: Classification of $M0$, $S1$, and $S2$ in the graphene sheet. The (n, m) indexes are written in the hexagon of the corresponding chiral vector. The white, violet, and light cyan hexagons correspond to the chiral vectors of $M0$, $S1$, and $S2$ SWNTs, respectively. The dashed red lines indicate the families of constant $2n + m$, $2m + n$, and $n - m$. The numbers of the triangle graphene sheet side indicate the values of $2n + m$, $2m + n$, and $n - m$ for each family [72].

and $\mathrm{mod}(n - m, 3) = \mathrm{mod}(4, 3) = 1$. Thus, the definition of $S1$ and $S2$ types is given by the $2n+m$ family line. In Fig. 2.8, the $M0$, $S1$, and $S2$ type SWNTs are classified by the definition of the family $2n + m$ =constant. The $2n + m$ families of the $M0$, $S1$, and $S2$ type SWNTs have the closest diameters, compared with the $2m + n$ and $n - m$ families.

Moreover, we can classify $M0$ SWNTs as $M1$ and $M2$ according to whether $d_R = 3d$ or $d_R = d$ [66], respectively, which d is the greatest common divisor of two integers, d =gcd(n, m). If $\mathrm{mod}(3m/d_R, 3) = 0$, the $M0$ SWNT becomes $M1$ type, otherwise $M2$ type. The Fermi energy of the $M1$ type is located at the Γ points of the 1D Brillouin zone, while the Fermi energy of $M2$ type is located at a $\frac{5}{6}$ (or $\frac{1}{6}$) position on a cutting line. The $M2$ type SWNTs further divide into $M2+$ and $M2-$, according to whether $\mathrm{mod}(3m/d_R, 3) = 1$ or 2 [66]. While the K point of 2D Brillouin zone of the graphene is located at the center of the cutting line for the $M1$ type SWNTs, for the $M2+$ and $M2-$

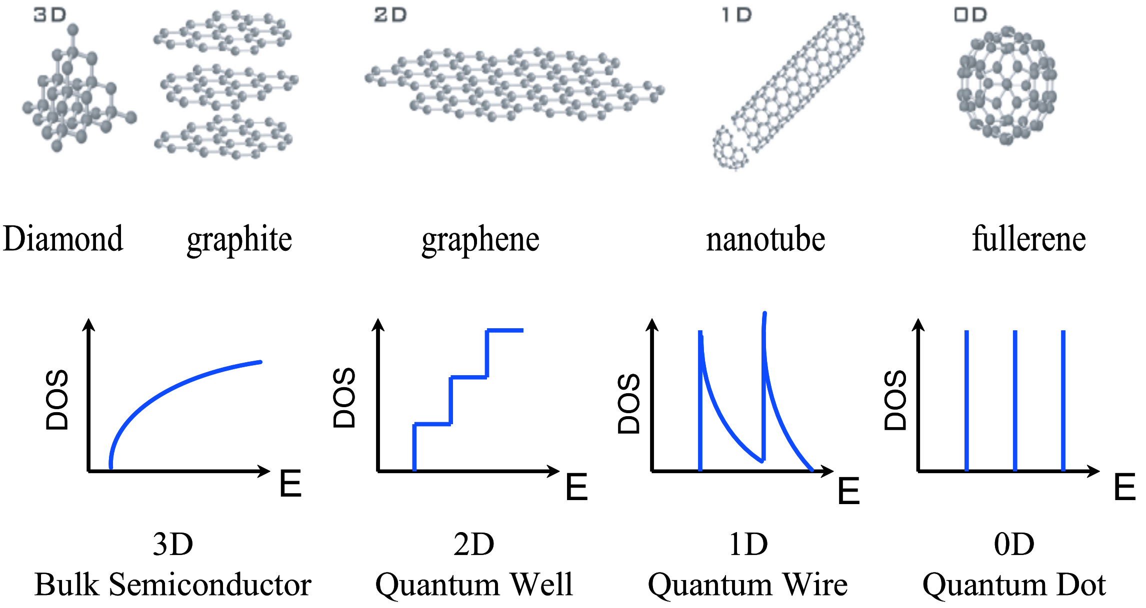

Figure 2.9: The electronic density of states (DOS) of typical 3D, 2D, 1D, and 0D systems. The representative 3D materials are diamond and graphite, for 2D, graphene sheet, for 1D, nanotube and nanowire, and for OD, fullerene. The DOSs of 3D and 2D systems are both increasing with increasing energy. The DOSs of 1D and 0D systems show singularities at certain energy values [73].

types, the K points are located at a $\frac{1}{6}$ and $\frac{5}{6}$ position of the cutting line, respectively. The $S1$ ($S2$) type SWNT also divides into $S1+$ and $S1-$ ($S2\pm$) for which satisfies the condition $\mathrm{mod}(N, 3) = 1$ or 2 [66], respectively. However, in general, the $M0$, $S1$, and $S2$ classification for $2n+m$ =constant family is sufficient for describing the optical properties of SWNTs.

2.2.3 Electronic density of states of SWNT

The electronic density of states (DOS), *i.e.*, the number of available electrons for a given energy interval, is useful to understand the application of the electronic properties and the experimental study. The DOS is known to depend on the dimension of a system, as shown in Fig. 2.9. For the parabolic bands as found in most of semiconductors, the DOS rises as the square root of the energy above the energy band bottom E_0 in the 3D case such as diamond and graphite, $g(E) \propto (E - E_0)^{\frac{1}{2}}$, in 2D systems such as graphene sheet, exhibits a step-like function, in 1D systems such as nanotube and nanowire, diverges as the inverse of a square root, $g(E) \propto (E - E_0)^{-\frac{1}{2}}$, and finally, in 0D systems such as fullerene, is a δ-function, $g(E) \propto \delta(E - E_0)$.

For a 3D system, E_0 might correspond to the energy gap for the onset of optical transitions, or to a band edge state such as an exciton in a semiconductor. For a 2D system, E_0 would correspond to the energy at which a new sub-band or a quantum confinement level is formed. For a 1D system, E_0 is equal to the sub-band edge energy E_i^b, where the magnitude of the DOS becomes singular as known as van Hove singularity (vHS) . The SWNT are one-dimensional material and an energy band can always be approximated as parabolic around its minimum and maximum, $E(\mu, k) = C_\mu k^2$ $(C_\mu > 0)$. Thus, we expect a $\frac{1}{\sqrt{E-E_0}}$ behavior for the DOS of the SWNTs, as shown in Figs. 2.5(c) and 2.6(c).

2.2.4 Extended tight binding model

In the previous sections, we used a model for the electronic energy dispersion relation of SWNTs based on the confinement of the π electrons in small stripes of graphene, that is, STB model. In this section, we present the extension of the zone-folding approximation and the STB model to the smaller diameter region (d_t <1.2 nm) which agrees well with the experimental Kataura plot obtained by the band gap PL measurements of SWNTs suspended by SDS surfactant in D_2O aqueous solution and was developed by Ge. G. Samsonidze *et al*. [14].

The Kataura plot describes the transition energy E_{ii} from E_i^v to E_i^c vHS energies as a function of SWNT diameter d_t or inverse SWNT diameter $1/d_t$, as shown in Fig. 2.10, where the index i specifies the vHS in the valence and conduction bands away from the Fermi level. The E_{ii} energies for $M0$, $S1$, and $S2$ SWNTs show a distinct behavior, while there is no obvious difference between $M1$ and $M2$ subtypes of $M0$ type. Within the $M0$, $S1$, and $S2$ types, each E_{ii} energy follows the family patterns of constant $2n + m$ group in the Kataura plot. The E_{ii} energies within each family of constant $2n + m$ group are connected by one line labeled by $2n + m$ values. By adjusting the STB parameters to the resonance Raman spectra from individual SWNTs on a SiO_2 substrate [74], the Kataura plot is calibrated with the fitting STB parameters, $\varepsilon = 0$ eV, $t = -2.89$ eV, and $s = 0$, as shown in Fig. 2.10. While the STB approach provides reliable results for the

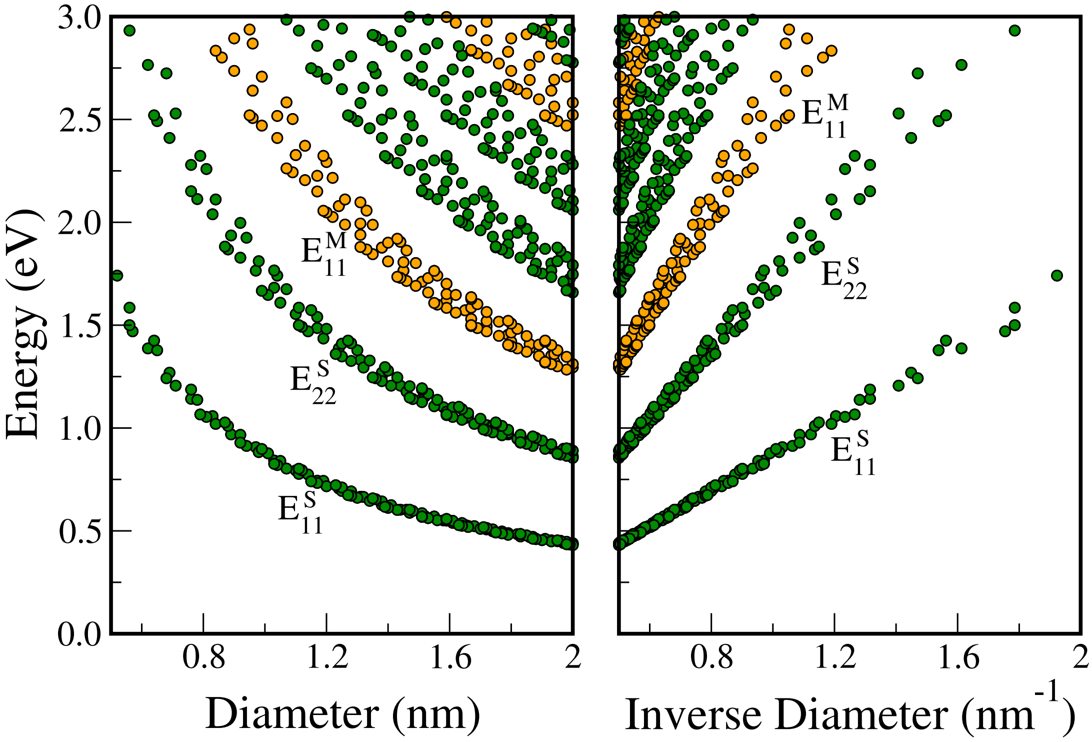

Figure 2.10: The Kataura plot for all possible (n, m) SWNTs calculated within the simple tight binding (STB) method of Section 2.2.2 as a function of the SWNT diameter d_t (left) and the inverse diameter $1/d_t$ (right). Green and orange circles correspond to semiconducting and metallic SWNTs, respectively.

larger diameter SWNTs (d_t >1.2 nm), because the electronic structures of SWNTs with large diameter are similar to those of the graphene sheet, it fails in the smaller diameter region (d_t <1.2 nm), as has been shown in photoluminescence (PL) and resonance Raman spectra studies of SWNTs dispersed by a surfactant (sodium dodecyl sulfate, SDS) in an aqueous solution (deuterium oxide, D_2O) [60] which was discussed in Chapter 1.

When comparing the experimental Kataura plot [75] with the one calculated from the STB model [10], two major differences can be found. First, the experimental E_{22}^S/E_{11}^S ratio in the large d_t limit is less than 2, while the E_{22}^S/E_{11}^S ratio by STB model approaches 2 with increasing d_t (the ratio problem) [76]. Second, in the small d_t limit, the experimental spread of the E_{ii}^S energies within the same constant $2n+m$ family is much larger than the corresponding spread of the STB E_{ii}^S energies. While the ratio problem can be explained by many-body effects [76], the family spread is mainly attributed to the curvature effects

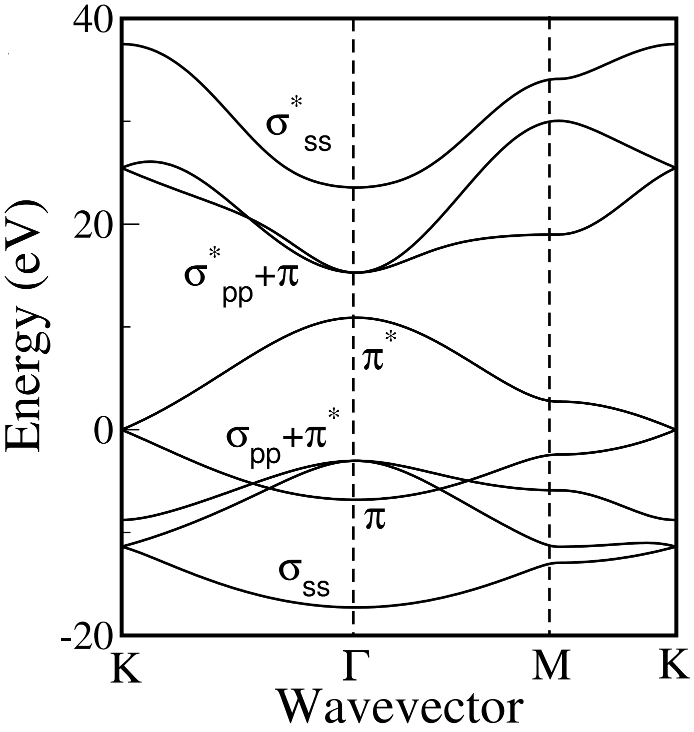

Figure 2.11: Electronic energy dispersion relations for the σ and π bands of a graphene sheet along the $K-\Gamma-M-K$ direction.

and to the C-C bond length optimization in SWNTs with small diameter (d_t <1.2 nm) [77] which are missing in the STB model, where we neglected the long-range atomic interactions and the σ molecular orbitals. In small d_t range, the long-range interactions of the π orbitals are not negligible [78], and the curvature of SWNT sidewall changes the lengths of the inter-atomic bonds as well as the angles of the hexagon. This leads the $sp^2 - sp^3$ re-hybridization, which has an effect on the electronic band structure of the π electrons around the Fermi level.

In graphene, the π molecular orbitals cannot mix with the σ orbitals because the π orbitals are perpendicular to the flat graphene sheet, while the σ orbitals are parallel to the graphene sheet. The σ (or σ^*) energy bands of the graphene lie several eV away from the Fermi level, in contrast to the π energy bands, and are obtained by solving the Eq. (2.2.10) for the σ molecular orbitals, as shown in Fig. 2.11. However, the π and σ orbitals on the curved sidewall of SWNT with small diameter d_t mix to each other and form hybrids that are partly of sp^2 state and partly of sp^3 state. In a small d_t limit, the geometrical structure of SWNT deviates from the rolled-up graphene sheet, and thus the geometrical structure optimization should be performed to allow for atomic relaxation to equilibrium position [77]. The curvature effect can be included in the tight binding model by extending the basis set to the atomic $2s$, $2p_x$, $2p_y$, and $2p_z$ orbitals at Eq. (2.2.3) that form the σ and π molecular orbitals according to the Slater-Koster formalism [69].

Thus, we can extend the STB model by including (1) the long-range atomic interactions and (2) the σ molecular orbitals, and (3) by optimizing the geometrical structure of SWNT. This model is called to the extended tight binding (ETB) model [14]. The ETB model makes use of the four transfer integrals $t_{ss}(R)$, $t_{s\sigma}(R)$, $t_{\sigma\sigma}(R)$, and $t_{\pi\pi}(R)$ and four overlap integrals $s_{ss}(R)$, $s_{s\sigma}(R)$, $s_{\sigma\sigma}(R)$, and $s_{\pi\pi}(R)$ as functions of the inter-atomic distance R calculated within a density functional theory (DFT) framework [79] and the two atomic orbital energies, $\varepsilon_{2s} = -13.57$ eV, and $\varepsilon_{2p} = -5.372$ eV. At the nearest neighbor inter-atomic distance $R = a_{\mathrm{CC}} = 0.142$ nm, the ETB parameter $t_{\pi\pi}$ and $s_{\pi\pi}$ have the value -3.351 eV and 0.150 eV, respectively, while the STB parameter $t_{\pi\pi} = -3.033$ eV and $s_{\pi\pi} = 0.129$ eV. At the second neighbor inter-atomic distance $R = a = \sqrt{3}a_{\mathrm{CC}} = 0.246$ nm, the ETB parameters $t_{\pi\pi}$ and $s_{\pi\pi}$ have the values -0.248 eV and 0.008 eV, which the STB parameters are neglected. In order to get the geometrical structure optimization of the SWNT, we have to minimize the total energy of the SWNT system which is given by a sum of the electronic band energy and the repulsive energy equal to a sum of short-range repulsive potentials between pairs of atoms. The total energy per a carbon atom of a graphene sheet is given by [72]:

$$E_{tot} = \sum_{b}^{8} n^b E^b + \frac{1}{4U} \sum_{uu'}^{U} \sum_{ss'} v(|R_{us} - R_{u's'}|), \tag{2.2.34}$$

where the electron occupation number n^b is 2 and 0 for the valence bands and for the conduction bands at $T = 0$ K, respectively, E^b is the electronic band energy, U is the number of the hexagonal unit cells of graphene, and the summation on atomic site s in unit cell u is carried out over the third neighbors of atomic site s' in unit cell u'. The factor $\frac{1}{4}$ indicates that each atomic pair in the second term of Eq. (2.2.34) is counted twice.

For the geometrical structure optimization of a SWNT, one needs the electronic band energy E^b and the repulsive energy $v(R)$ contributions to the forces acting on the carbon atoms. The electronic energy band contribution to the force on the atom with a position

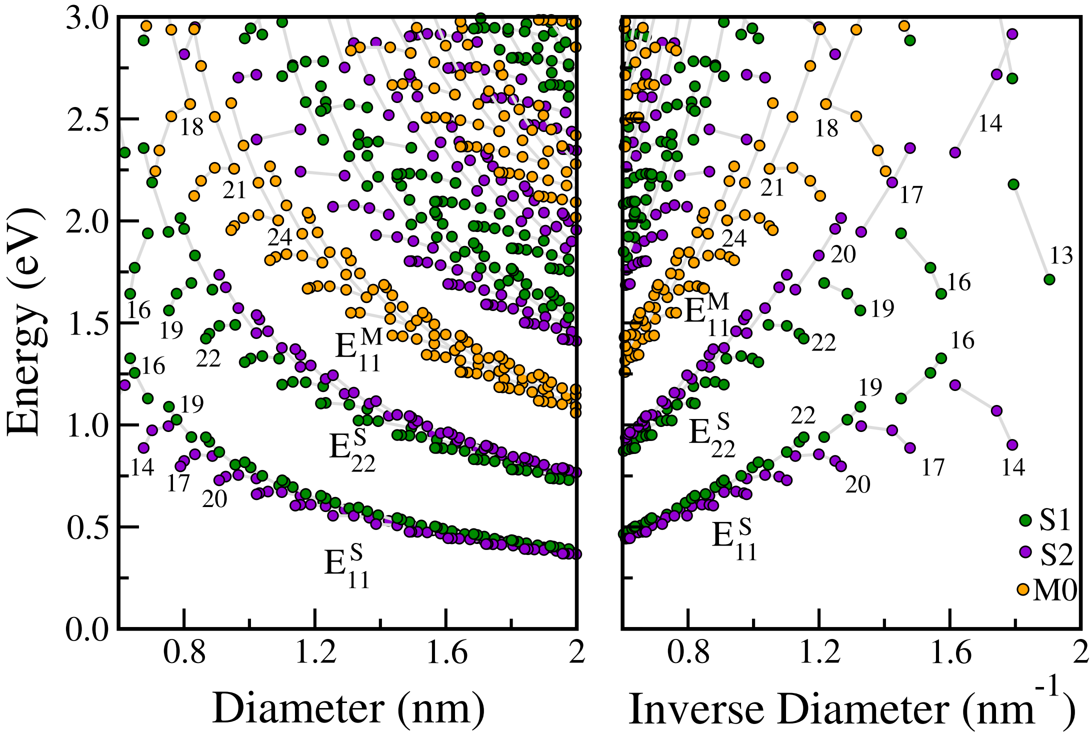

Figure 2.12: The Kataura plot for all possible (n, m) SWNTs calculated within the extended tight binding (ETB) method as functions of the SWNT diameter d_t (left) and the inverse diameter $1/d_t$ (right). Green, violet, and orange circles correspond to S1, S2, and M0 SWNTs, respectively. The E_{ii} energies within the family constant $2n + m$ group are connected by gray lines and labeled by $2n + m$ values.

vector $\mathbf{R}_{u's'}$ is given by the Hellmann-Feynman theorem, $\mathbf{F} = \partial E^b / \partial \mathbf{R}_{u's'}$. The repulsive energy contribution is the first derivative of the total repulsive energy with respect to $\mathbf{R}_{u's'}$.

The ETB Kataura plot considered for the optimized geometrical structure shows a similar family spread to the PL and RRS experimental Kataura plots as shown in Fig. 2.12. The experimental family spread is attributed to the relaxation of the geometrical structure of the SWNTs. Even though the family spread of ETB model is good agreement with the PL and RRS Kataura plots, it still remains an overall blue-shift of E_{ii}^{Exp} $(200 - 300$ meV) from the ETB Kataura plot. The differences between the experimental PL energies E_{ii}^{PL} and the corresponding ETB calculated energies E_{ii}^{ETB}, ΔE_{ii}, depend on the chiral angle weakly and d_t monotonically. These energy differences can be explained by many-body effects [80–85]. The many-body (exciton) effect consists of electron-electron Coulomb repulsion and the electron-hole Coulomb attraction. Because of the 1D SWNT structure, electron-electron Coulomb repulsion exceeds the electron-hole Coulomb attraction so that the energies E_{ii} by the many-body effect have blue-shifted value from one-electron energies E_{ii}.

Chapter 3

Calculation method

In this Chapter, we introduce the electron-photon and electron-phonon interactions, and then explain how to calculate the resonance window in Chapter 4, and the G' Raman spectra for the SWNT and multi-layer graphene, respectively, in Chapters 5 and 6.

3.1 Electron-photon interaction

The optical transition in solid consists of the absorption and emission of photons with the excitation and annihilation of an electron-hole pair, respectively. These processes are determined by the electron-photon interaction. The most important term in the electron-photon interaction is the dipole-allowed transition, where the probability of the transition is determined by the matrix element.

Within time-dependent perturbation theory, the electron-photon matrix elements for the dipole transition between the initial $\mathbf{k}_i$ and final $\mathbf{k}_f$ electronic states is given by:

$$M^{b'\lambda b}_{\text{el}-\text{op}}(\mathbf{k}_f, \mathbf{p}, \mathbf{k}_i) = \langle \Psi^{b'}(\mathbf{k}_f, \mathbf{r}, t) | H^{\lambda}_{\text{el}-\text{op}}(\mathbf{p}, \mathbf{r}, t)) | \Psi^{b}(\mathbf{k}_i, \mathbf{r}, t) \rangle, \tag{3.1.1}$$

where b is the band index, λ is the polarization index, $\mathbf{p}$ is the photon wave vector, $\Psi^b(\mathbf{k}, \mathbf{r}, t)$ is one electron wave function in the b-th electronic energy band of Eq. (2.2.3), $\mathbf{r}$ is the spatial coordinate, and $H^{\lambda}_{\text{el}-\text{op}}(\mathbf{p}, \mathbf{r}, t)$ is the perturbation Hamiltonian acting on an electron and generates its transition from the initial $\mathbf{k}_i$ and final $\mathbf{k}_f$ electronic states:

$$H^{\lambda}_{\text{el}-\text{op}}(\mathbf{p}, \mathbf{r}, t)) = i\frac{e\hbar}{m}\mathbf{A}^{\lambda}(\mathbf{p}, \mathbf{r}, t)) \cdot \nabla, \tag{3.1.2}$$

where e is the elementary charge, m is the electron mass, $\mathbf{A}^{\lambda}(\mathbf{p}, \mathbf{r}, t)$ is the vector potential of the electromagnetic field, and ∇ is the gradient operator. Optical transitions occur vertically in the k space, connecting an occupied energy band to an unoccupied one with almost the same wave vector as a result of energy-momentum conservation of the light and electron. Therefore, $\mathbf{p}$ is neglected, $\mathbf{p}=0$, and $\mathbf{k}_i=\mathbf{k}_f=\mathbf{k}$.

The vector potential of the electromagnetic field is obtained by solving Maxwell equations:

$$\mathbf{A}^{\lambda}(0,\mathbf{r},t)=\sqrt{\frac{\hbar n_{\pm}^{\lambda}}{2\kappa\kappa_0 V\omega}}e^{i(\kappa r\mp\omega t)}\mathbf{P}^{\lambda}, \tag{3.1.3}$$

where κ is the dielectric constant of the material, κ_0 is the dielectric permittivity of free space, V is the quantization volume for the electromagnetic field, $n_{\pm}^{\lambda}$ is the photon occupation number for the emission (+) and absorption (−), ω is the photon frequency, and $\mathbf{P}^{\lambda}$ is the photon polarization vector. The electron-photon matrix elements for the photon induced absorption and spontaneous emission processes, $M^{c\lambda v}(\mathbf{k},0,\mathbf{k})$ and $M^{v\lambda c}(\mathbf{k},0,\mathbf{k})$, respectively, are given by substituting Eqs. (2.2.3) and (3.1.3) into Eq. (3.1.2):

$$\begin{cases} M^{c\lambda v}_{\mathrm{el-op}}(\mathbf{k},0,\mathbf{k})=i\dfrac{e\hbar^2}{mE_{\mathrm{L}}}\sqrt{\dfrac{I}{2\sqrt{\kappa}\kappa_0 c}}\mathbf{P}^{\lambda}\cdot\mathbf{D}^{\mathrm{cv}}(\mathbf{k},0,\mathbf{k}), \\ M^{v\lambda c}_{\mathrm{el-op}}(\mathbf{k},0,\mathbf{k})=i\dfrac{e\hbar^2}{mE_{\mathrm{L}}}\sqrt{\dfrac{E_{\mathrm{L}}}{2\kappa\kappa_0 V}}\mathbf{P}^{\lambda}\cdot\mathbf{D}^{\mathrm{vc}}(\mathbf{k},0,\mathbf{k}), \end{cases} \tag{3.1.4}$$

where I is the radiant flux density of the incoming light beam, E_{L} is the incident laser energy, and $\mathbf{D}^{b'b}(\mathbf{k},0,\mathbf{k})$ is the dipole vector to represent the transition from the b-th energy band to the b'-th energy band:

$$\begin{aligned} \mathbf{D}^{b'b}(\mathbf{k},0,\mathbf{k}) &= \langle\Psi^{b'}(\mathbf{k}_f,\mathbf{r},t)|\nabla|\Psi^{b}(\mathbf{k}_i,\mathbf{r},t)\rangle \\ &= \sum_{s'o'}\sum_{so}C^{b'*}_{s'o'}(\mathbf{k})C^{b}_{so}(\mathbf{k})\mathbf{D}_{s'o'so}(\mathbf{k},0,\mathbf{k}), \end{aligned} \tag{3.1.5}$$

where $\mathbf{D}_{s'o'so}(\mathbf{k},0,\mathbf{k})$ is the atomic dipole matrix elements:

$$\mathbf{D}_{s'o'so}(\mathbf{k},0,\mathbf{k})=\frac{1}{U}\sum_{u}^{U}e^{i\mathbf{k}\cdot\mathbf{R}}\int\phi^{*}_{o'}(\mathbf{r})\nabla\phi_{0}(\mathbf{r}-\mathbf{R})d\mathbf{r}, \tag{3.1.6}$$

where $\mathbf{R}=\mathbf{R}_{us}-\mathbf{R}_{u's'}$ connects the two interacting atoms, and $\phi(\mathbf{r})$ is the atomic wave function in Eq. (2.2.4). As for $\mathbf{D}_{s'o'so}(\mathbf{k},0,\mathbf{k})$, we consider only $2p_z$ orbital in the nearest neighbor interaction [36].

3.2 Electron-phonon interaction

A periodic displacement of atoms around the equilibrium position gives rise to the electron-phonon interaction which can be treated in first-order time-dependent perturbation theory. The electron-phonon interaction plays an important role in the calculation of the Raman intensity or the lifetime of a photo-excited carrier. The electron-phonon interactions can also induce subtle changes in the electronic band structure and open a small band gap at the Fermi level of metallic SWNTs [86, 87]. The matrix element of the electron-phonon interaction is determined by a scalar product of the derivative of the periodic potential V with respect to an atomic displacement vector in the ν-th phonon eigenvector [8, 12, 34]. The electron-phonon interaction matrix element from an initial $\mathbf{k}_i$ to the final $\mathbf{k}_f$ electronic states in the SWNT system can be written by the following form:

$$M_{\text{el-ph}}^{b'\nu b}(\mathbf{k}_f, \mathbf{q}, \mathbf{k}_i) = \langle \Psi^{b'}(\mathbf{k}_f, \mathbf{r}, t) | \delta V^{\nu}(\mathbf{q}, \mathbf{r}, t) | \Psi^{b}(\mathbf{k}_i, \mathbf{r}, t) \rangle, \tag{3.2.1}$$

where $\Psi^b(\mathbf{k}_f, \mathbf{r}, t)$ is the one-electron wave function in the b-th electronic energy band of Eq. (2.2.3), δV^ν is the variation of the periodic potential for the ν-th phonon mode, which is expressed by the deformation potential ∇v:

$$\delta V^{\nu}(\mathbf{q}, \mathbf{r}, t) = -\sum_{u's'} \nabla v(\mathbf{r} - \mathbf{R}_{u's'}) \cdot S^{\nu}(\mathbf{R}_{u's'}), \tag{3.2.2}$$

where $v(\mathbf{r} - \mathbf{R}_{u's'})$ is the Kohn-Sham potential of a neutral pseudoatom moving along $\mathbf{R}_{u's'}$, and $S^\nu(\mathbf{R}_{u's'})$ is the site position deviation from the equilibrium site $\mathbf{R}_{u's'}$ caused by a vibration:

$$S^{\nu}(\mathbf{R}_{us}) = \sqrt{\frac{\hbar n_{\pm}^{\nu}(\mathbf{q})}{2UM\omega^{\nu}(\mathbf{q})}} \mathbf{e}_s^{\nu}(\mathbf{q}) e^{\mp i \left(\mathbf{q} \cdot \mathbf{R}_{us} - \omega^{\nu}(\mathbf{q}) t \right)}, \tag{3.2.3}$$

where U is the number of two-atom unit cells, M is the carbon atom mass, $\omega^\nu(\mathbf{q})$ is the ν-th phonon frequency, $\mathbf{e}_s^\nu(\mathbf{q})$ is the phonon eigenvector, and $n_\pm^\nu(\mathbf{q})$ is the phonon occupation number for the phonon emission (+) and absorption (−), respectively. At equilibrium position, the phonon occupation number $n^\nu(\mathbf{q})$ is determined by the Bose-Einstein distribution function:

$$n^{\nu}(\mathbf{q}) = \frac{1}{e^{\hbar \omega^{\nu}(\mathbf{q})/k_{\mathrm{B}}T} - 1}, \tag{3.2.4}$$

where k_{B} is the Boltzmann constant and T is the temperature.

Substituting Eqs. (2.2.3), (3.2.2), and (3.2.3) into Eq. (3.2.1), the electron-phonon matrix element from $\mathbf{k}_i$ in the b-th energy band to $\mathbf{k}_f$ in the b'-th energy band coupled by the ν-th phonon mode is given by:

$$M^{b'\nu b}_{\text{el-ph}}(\mathbf{k}_f, \mathbf{q}, \mathbf{k}_i) = -\sqrt{\frac{\hbar n^{\nu}_{\pm}(\mathbf{q})}{2UM\omega^{\nu}(\mathbf{q})}}\, m^{b'\nu b}_{\text{el-ph}}(\mathbf{k}_f, \mathbf{q}, \mathbf{k}_i). \tag{3.2.5}$$

Here, $m^{b'\nu b}_{\text{el-ph}}(\mathbf{k}_f, \mathbf{q}, \mathbf{k}_i)$ is expressed in the following form:

$$m^{b'\nu b}_{\text{el-ph}}(\mathbf{k}_f, \mathbf{q}, \mathbf{k}_i) = \sum_{s'o'}\sum_{so} C^{b'^*}_{s'o'}(\mathbf{k}_f) C^{b}_{so}(\mathbf{k}_i) D^{\nu}_{s'o'so}(\mathbf{k}_f, \mathbf{q}, \mathbf{k}_i), \tag{3.2.6}$$

where $D^{\nu}_{s'o'so}(\mathbf{k}_f, \mathbf{q}, \mathbf{k}_i)$ is the atomic deformation potential matrix element:

$$D^{\nu}_{s'o'so}(\mathbf{k}_f, \mathbf{q}, \mathbf{k}_i) = \sum_{u''s''} \langle \Phi_{s'o'}(\mathbf{k}_f, \mathbf{r}) | \nabla v(\mathbf{r} - \mathbf{R}_{u''s''}) \cdot \mathbf{e}^{\nu}_{s''}(\mathbf{q}) e^{\mp i\left(\mathbf{q}\cdot\mathbf{R}_{u''s''} - \omega^{\nu}(\mathbf{q})t\right)} | \Phi_{so}(\mathbf{k}_i, \mathbf{r}) \rangle, \tag{3.2.7}$$

where $\Phi_{so}(\mathbf{k}, \mathbf{r})$ is the Bloch wave function in Eq. (2.2.4). By keeping only two-center atomic matrix elements, $\mathbf{R}_{u''s''} = \mathbf{R}_{us}$, $\mathbf{R}_{u''s''} = \mathbf{R}_{u's'}$, and $\mathbf{R}_{u's'} = \mathbf{R}_{us}$, we can split Eq. (3.2.7) into three terms:

$$\begin{aligned} D^{\nu}_{s'o'so}(\mathbf{k}_f, \mathbf{q}, \mathbf{k}_i) = \sum_{u}^{U} & \Big(\alpha_{o'o}(\mathbf{R}_{us} - \mathbf{R}_{u's'}) \cdot \mathbf{e}^{\nu}_{s'}(\mathbf{q})\Big) e^{-i\mathbf{k}_f(\mathbf{R}_{us} - \mathbf{R}_{u's'})} \\ + & \Big(\beta_{o'o}(\mathbf{R}_{us} - \mathbf{R}_{u's'}) \cdot \mathbf{e}^{\nu}_{s'}(\mathbf{q})\Big) e^{i\mathbf{k}_i(\mathbf{R}_{us} - \mathbf{R}_{u's'})} \\ + & \Big(\lambda_{o'o}(\mathbf{R}_{us} - \mathbf{R}_{u's'}) \cdot \mathbf{e}^{\nu}_{s'}(\mathbf{q})\Big) e^{\pm i\mathbf{q}(\mathbf{R}_{us} - \mathbf{R}_{u's'})}, \end{aligned} \tag{3.2.8}$$

where the atomic deformation potential vector $\alpha_{o'o}(\mathbf{R})$, $\beta_{o'o}(\mathbf{R})$, and $\lambda_{o'o}(\mathbf{R})$ are defined as follows [12, 72]:

$$\begin{cases} \alpha_{o'o}(\mathbf{R}) = \displaystyle\int \phi^{*}_{o'}(\mathbf{r}) \nabla v(\mathbf{r} - \mathbf{R}) \phi_{o}(\mathbf{r} - \mathbf{R}) d\mathbf{r}, \\ \beta_{o'o}(\mathbf{R}) = \displaystyle\int \phi^{*}_{o'}(\mathbf{r}) \nabla v(\mathbf{r}) \phi_{o}(\mathbf{r} - \mathbf{R}) d\mathbf{r}, \\ \lambda_{o'o}(\mathbf{R}) = \displaystyle\int \phi^{*}_{o'}(\mathbf{r}) \nabla v(\mathbf{r} - \mathbf{R}) \phi_{o}(\mathbf{r}) d\mathbf{r}, \end{cases} \tag{3.2.9}$$

where $\phi_o(\mathbf{r})$ is the atomic wave function for the o-th orbital, $\mathbf{R}$ connects the two interacting atoms, $\alpha_{o'o}(\mathbf{R})$ and $\beta_{o'o}(\mathbf{R})$ are the off-site atomic deformation potential vectors, and $\lambda_{o'o}(\mathbf{R})$ is the on-site atomic deformation potential vector.

3.3 Raman resonance window

For a resonance system, the resonance window γ is related to the energy dissipation. In quantum mechanics, γ is obtained by the uncertainty relation to the lifetime of the photo-excited carriers. The dominant origin of the lifetime of the photo-excited carriers in the Raman spectra is inelastic scattering by emitting or absorbing phonons. In this section, we calculate the carrier lifetime [34] by considering electron-phonon matrix elements [8,12] and the Fermi Golden rule.

3.3.1 Electron-phonon transition probability

In this section, we calculate the electron-phonon transition probability for a photo-excited electron scattered to the other electronic states by emitting or absorbing a phonon. The inverse of this transition probability is called to the relaxation time τ [13, 88] which is inversely proportional to the resonance window, γ, and the γ satisfies the uncertainty principle:

$$\gamma = \frac{\hbar}{\tau}. \tag{3.3.1}$$

We consider the effect of a time-dependent perturbation Hamiltonian for the electron-phonon interaction $H_{\mathrm{el-ph}}$ on the system which has eigenstates $|i\rangle$ of a given Hamiltonian H_0. If $H_{\mathrm{el-ph}}$ is oscillating as a function of time with an angular frequency ω, the transition occurs from the initial state to other states, absorbing or emitting the phonon energy $\hbar\omega$. In both cases, the one-to-many transition probability per unit of time, $W_{i\to f}$, from the initial state $|i\rangle$ to a set of final states $|f\rangle$ is given by first order perturbation theory to be called to Fermi Golden rule [13, 88]:

$$W_{i\to f} = \frac{2\pi}{\hbar} \sum_f |\langle f|H_{\mathrm{el-ph}}|i\rangle|^2 \delta(\varepsilon_f - \varepsilon_i \pm \hbar\omega), \tag{3.3.2}$$

where the delta function $\delta(\varepsilon_f - \varepsilon_i \pm \hbar\omega)$ expresses the energy-momentum conservation, and $\langle f|H_{\mathrm{el-ph}}|i\rangle$ indicates the electron-phonon interaction matrix element in Eqs. (3.2.1) and (3.2.5).

Therefore, the transition probability for the scattering of an excited electron from an initial state $\mathbf{k}$ to a final states $\mathbf{k}'$ by the ν-th phonon mode per unit time can be obtained by substituting Eq. (3.2.5) into Eq. (3.3.2):

$$\begin{aligned} W^{\nu}_{\mathbf{k}\to\mathbf{k}'} &= \frac{2\pi}{\hbar}\frac{\hbar}{2UM\omega^{\nu}(\mathbf{q})}|m^{b'\nu b}_{\mathrm{el-ph}}(\mathbf{k}',\mathbf{q},\mathbf{k})|^2 \\ &\quad\times\Big\{n^{\nu}(\mathbf{q})\delta\big(\varepsilon_f-\varepsilon_i-\hbar\omega^{\nu}(\mathbf{q})\big)+\big(n^{\nu}(\mathbf{q})+1\big)\delta\big(\varepsilon_f-\varepsilon_i+\hbar\omega^{\nu}(\mathbf{q})\big)\Big\}. \end{aligned} \tag{3.3.3}$$

Here, the electron wave vector $\mathbf{k}$ of a SWNT can be expressed by the cutting line, $\mu\mathbf{K}_1 + k\mathbf{K}_2/K_2$. The wave number k becomes continuous along the $\mathbf{K}_2$ axis because the SWNT is sufficiently long in the direction of nanotube axis:

$$\begin{aligned} \sum_k &\to \frac{L}{2\pi}\int dk \\ &= \frac{SU}{2\pi^2 d_t}\int\left[\frac{dE}{dk}\right]^{-1} dE, \end{aligned} \tag{3.3.4}$$

where L is the SWNT length, S denotes the area of the 2D graphene unit cell. The surface area of a SWNT is given by $US = \pi d_t L$. Therefore, we can obtain the final form of the transition probability from an initial state $\mathbf{k}$ to all possible final states $\mathbf{k}'$:

$$\begin{aligned} W_{\mathbf{k}} &= \sum_{\mathbf{k}',\nu} W^{\nu}_{\mathbf{k}\to\mathbf{k}'} \\ &= \frac{S}{2\pi M d_t}\sum_{\mu',k',\nu}\frac{|m^{b'\nu b}_{\mathrm{el-ph}}(\mathbf{k}',\mathbf{q},\mathbf{k})|^2}{\omega^{\nu}(\mathbf{q})}\left[\frac{dE(\mu',k')}{dk'}\right]^{-1} \\ &\quad\times\left\{\frac{\delta\big(\varepsilon(\mathbf{k}')-\varepsilon(\mathbf{k})-\hbar\omega^{\nu}(\mathbf{q})\big)}{e^{\beta\hbar\omega^{\nu}(\mathbf{q})}-1}+\frac{\delta\big(\varepsilon(\mathbf{k}')-\varepsilon(\mathbf{k})+\hbar\omega^{\nu}(\mathbf{q})\big)}{1-e^{-\beta\hbar\omega^{\nu}(\mathbf{q})}}\right\}, \end{aligned} \tag{3.3.5}$$

where $\beta = 1/k_{\mathrm{B}}T$, μ' is the cutting line index of the final state, and $[dE(\mu',k')/dk']^{-1}$ is the density of final state. The relaxation process is restricted to satisfying energy-momentum conservation. The first and second terms in brace in Eq. (3.3.5), respectively, represent the absorption and emission processes of the ν-th phonon mode with phonon energy $\hbar\omega_{\nu}(\mathbf{q})$. In Eq. (3.3.5), the phonon absorption rate for optical phonons with high phonon energy is very small compared with the emission rate at the room temperature, since when the phonon energy $\hbar\omega_{\nu}(\mathbf{q})$ increases relative to $k_{\mathrm{B}}T$, the number of phonons for the absorption and emission approach 0 and 1, respectively.

3.4 Double resonance Raman scattering

Double resonance Raman scattering consists of (1) two-phonon scattering processes and (2) one-phonon and one-elastic scattering process [7, 52–57]. Two-phonon scattering pro-

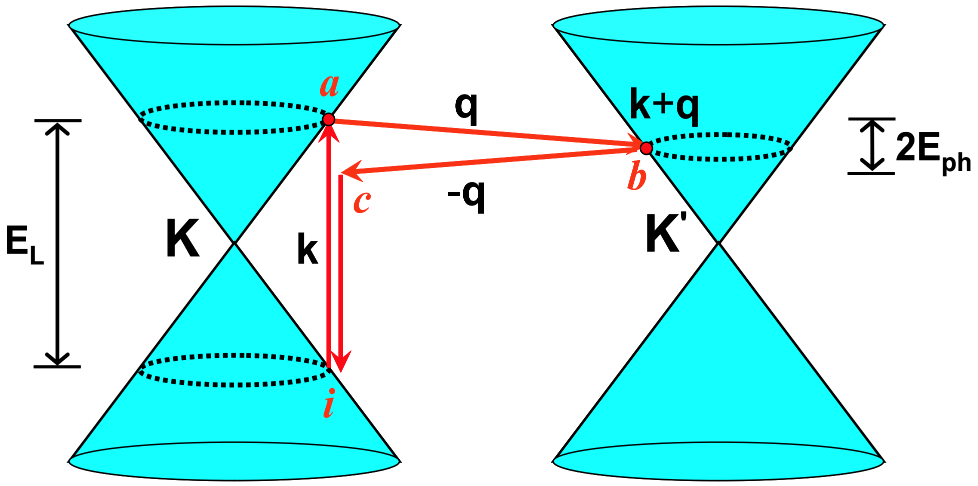

Figure 3.1: Schematic two-phonon Raman scattering processes. The optical transition occurs from the valence band i state with $\mathbf{k}$ wave vector to the conduction band a state with the same wave vector by absorbing a photon. Then, the electron-phonon interaction $M_{\rm el-ph}$ which was explained in Section 3.2 creates (or annihilates) a phonon and the excited electron scatters from a state around the K point to b state around the K' state, changing its energy. The electron at b state scatters back to c state by interacting another phonon, and finally, recombines with a hole at i state by emitting a photon. The solid red arrows indicate the double resonance Raman scattering processes, and the two solid red circles at a and b represent the resonance points.

cesses involve the same phonon modes (an overtone mode) and different phonon modes (a combination mode). In graphene and SWNT, the D band which appears at around 1350 cm^{-1} is related to one-phonon and one-elastic scattering process, and the G' band which appears at around 2700 cm^{-1} is due to two-phonon Raman scattering processes. In Chapters 5 and 6, we will explain the properties of the G' Raman spectra for SWNTs and multi-layer graphene.

3.4.1 G' band of SWNT

The two-phonon scattering processes for the G' band intensity are calculated by the extended tight-binding (ETB) method. The electronic energy dispersion of a SWNT was obtained by using the ETB method, in which $2s$, $2p_z$, $2p_y$, and $2p_x$ atomic orbitals are taken into account to reproduce the E_{ii} values for a SWNT particularly for a smaller diameter SWNT, as explained in Section 2.2.4. The phonon dispersion relation, $\hbar\omega_\nu(\mathbf{q})$, was calculated using the force-constant tight binding model, in which the force constant was taken up to the 20th nearest neighbor atomic sites given by Dubay and Kresse [89], which reproduces the phonon dispersion obtained by the inelastic X-ray scattering [90]. The Raman intensity for the G' band Raman spectra, $I(\omega, E_\mathrm{L})$, is given as a function of excitation laser energy E_L and the sum of two phonon energies $\omega = \omega_1 + \omega_2$ using the following formula:

$$I(\omega(\mathbf{q}), E_\mathrm{L}) = \sum_i \left| \sum_{a,b,\omega_1,\omega_2} J_{a,b}\big(\omega_1(\mathbf{q}), \omega_2(\mathbf{q})\big) \right|^2, \tag{3.4.1}$$

where $J_{a,b}\big(\omega_1(\mathbf{q}), \omega_2(\mathbf{q})\big)$ is given by:

$$J_{a,b}\big(\omega_1(\mathbf{q}), \omega_2(\mathbf{q})\big) = \frac{M_{\mathrm{el-op}}(i,c)M_{\mathrm{el-ph}}(c,b)M_{\mathrm{el-ph}}(b,a)M_{\mathrm{el-op}}(a,i)}{\Delta E_{ai}(\Delta E_{bi} - \hbar\omega_1(\mathbf{q}))(\Delta E_{ai} - \hbar\omega_1(\mathbf{q}) - \hbar\omega_2(\mathbf{q}))}, \tag{3.4.2}$$

and $\Delta E_{ai} = E_\mathrm{L} - (E_a - E_i) - i\gamma$ is the incident resonance condition, γ denotes the Raman resonance window, i, a, b and c denote the initial, the excited, the first scattered, and the second scattered states of the photo-excited electron, respectively. The two-phonon scattering processes involve $\mathbf{q}$ and $-\mathbf{q}$ scattering phonon wave vectors, so that a photo-excited electron can return to its original $\mathbf{k}$ electron wave vector after the electron-phonon scattering. In two-phonon scattering processes for the SWNTs, a valence electron (1) absorbs a photon at a $\mathbf{k}$ electron state, (2) scatters to $\mathbf{k}+\mathbf{q}$ state by emitting a phonon with $\mathbf{q}$ wave vector in conduction band, (3) scatters back to the $\mathbf{k}$ state by emitting another phonon with $-\mathbf{q}$ wave vector , and (4) emits a photon by recombining with a hole at the $\mathbf{k}$ state in valence band. The phonon scattering is inelastic by emitting a phonon, as shown in Fig. 3.1.

For simplicity, only electron-phonon scattering but no hole-phonon scattering processes were taken into account in the present thesis. $M_{\mathrm{el-ph}}$ and $M_{\mathrm{el-op}}$ indicate the electron-phonon and electron-photon interaction matrix elements, respectively, which were calculated using the ETB electronic wave function and the force-constant tight-binding phonon modes. In the calculation of electron-phonon interaction matrix elements, the amplitude of the atomic vibration for each carbon atom was calculated for a large unit cell with a length of 1000 nm and at a temperature of 300 K. In the summation of the phonon frequencies ω_1 and ω_2, the energy-momentum conservation is required for the matrix elements, either for $M_{\mathrm{el-ph}}(b, a)$ or for $M_{\mathrm{el-ph}}(c, b)$, in order to satisfy the double resonance condition, either for the incident resonance or for the scattered resonance, respectively. For ω_1 and ω_2, 48 ($= 6 \times 2 \times 2 \times 2$) possible electron-phonon scattering processes which satisfy the energy-momentum conservation can exist as far as the scattered electronic states are unoccupied, because there are (1) six phonon modes in the 2D graphite Brillouin zone, (2) two intra-valley and inter-valley scatterings, where the intra-valley and inter-valley scatterings denote the scattering of an electron from K to K (or K' to K') and from K to K' (or K' to K), respectively, (3) two scattering directions (forward and backward scatterings) and (4) phonon absorption and emission. For the G' band intensity calculation, we select some of these possible cases, that is, two phonon modes (in-plane transverse optic (iTO) and longitudinal optic (LO) mode), inter-valley scattering, forward and backward scatterings, and only phonon emission. In the denominator ($\Delta E_{ai} = E_{\mathrm{L}} - (E_a - E_i) - i\gamma$) of Eq. (3.4.2), the Raman resonance window, γ, was calculated from the uncertainty principle for a finite lifetime of a photo-excited electron due to the electron-phonon interaction for each (n, m) SWNTs using the Fermi Golden rule [61] (See the Eq. (3.3.1) and Eq. (3.3.5)). The calculated γ values were checked in order to reproduce the resonance window of the Raman excitation profile for the RBM modes observed by single nanotube spectroscopy.

3.4.2 G' band of graphene

single layer graphene

The G' band of the graphene which appears at around 2650 cm^{-1} is the two-phonon double resonance Raman scattering process similar to that of SWNT. The two-phonon scattering process for the G' band of the graphene sheet is an inter-valley scattering process which connects two high symmetry points K and K' of first Brillouin zone of the graphene. For the calculation of the G' band of the graphene, we also have to consider the electron-photon and electron-phonon matrix elements similarly in Section 3.4.1. In order to calculate the G' band Raman intensity of the graphene at frequency ω for the laser excitation energy E_{L}, we use a similar formula to Eqs. (3.4.1) and (3.4.2) [7]. The electronic band structure of the graphene is calculated by the ETB method as explained in Chapter 2. The band structure of the graphene shows a linear energy dispersion relation

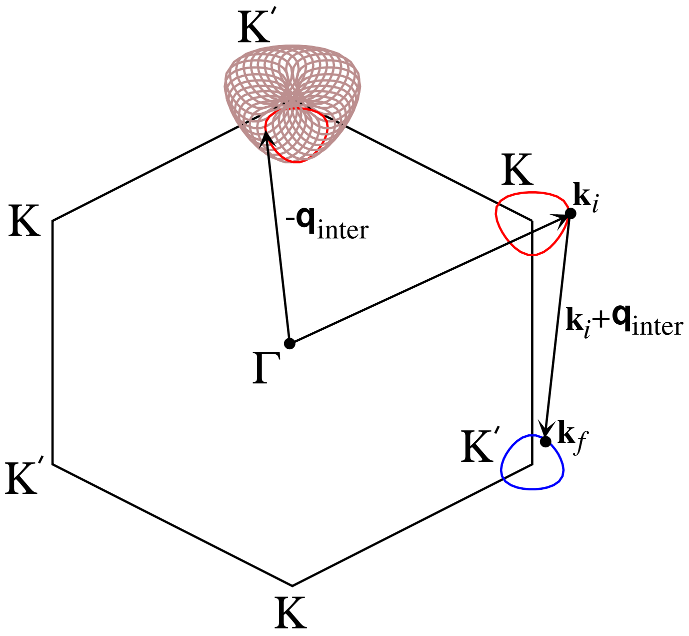

Figure 3.2: Equi-energy contours for incident laser energy $E = E(\mathbf{k}_i)$, interaction energy $E(\mathbf{k}_i + \mathbf{q}_{\text{inter}})$, and scattered energy $E(\mathbf{k}_f)$ are shown as red, brown, and blue solid circles, respectively, around the hexagonal corners of the K or K' points in the 2D Brillouin zone of the graphene sheet. Solid arrow with $\mathbf{q}_{\text{inter}}$ denote an inter-valley scattering from a given electron wave vector $\mathbf{k}$ as shown around the upper-right K point. When we measure phonon wave vectors $\mathbf{q}$ from the Γ point, $\mathbf{q}_{\text{inter}} = \mathbf{k}_f - \mathbf{k}_i$ exists on brown solid circles around the K' point for the given electron wave vector $\mathbf{k}$ by considering momentum conservation.

around the K and K' points near the Fermi level and the valence and conduction bands touch each other at the K and K' points.

In order to find the phonon wave vector $\mathbf{q}$ as shown in Fig. 3.2, we select an equi-energy contour with the same incident excitation laser energy around the K point and another equi-energy contour around the K' point after one phonon scattering. Therefore, the phonon states $\mathbf{q}$ are obtained around the K' point that connects the electronic states $\mathbf{k}_i$ and $\mathbf{k}_f$ on the contours around the K and K' points according to the momentum conservation relative to $\mathbf{q} = \mathbf{k}_f - \mathbf{k}_i$. The phonon dispersion relations of the graphene are obtained by the force-constant model in which we consider up to the 20-th nearest neighbor atomic sites [89] so as to reproduce the inelastic X ray scattering for the phonon dispersion [90]. The ΔE_{ai} in the denominator of Eq. (3.4.1) which denotes the Raman resonance condition includes the energy uncertainty, γ, attributed to the experimental resonance window. Here we simply use γ=10 meV for all the cases. In previous section, we showed how to calculate the γ values for SWNTs [61]. In the case of the graphene, we use the γ value averaged over the equi-energy line. For comparison with the experiment, we calculate five spectral profiles $I(\omega, E_{\rm L})$ for excitation energies $E_{\rm L}$=1.65, 1.75, 1.92, 2.06, and 2.41 eV. Around the K point, we have three phonon modes iTO (in-plane transverse optical), iLO (in-plane longitudinal optical), and iLA (in-plane longitudinal acoustic) from the higher frequency range. Here we consider only the iTO phonon mode since the G' band comes from the iTO overtone modes along the $K\Gamma$ direction [7, 23]. The results will be shown in Chapter 6.

double and triple layer graphene

In order to understand the G' Raman band of the double and triple layer graphenes, we first calculate the electronic band structure. By considering the unit cells of double and triple layer graphenes with an AB layer stacking, we calculate the electronic energy band structures for each of the number of layers. Figure 3.3 shows the atomic structures of the double and triple layer graphenes. Two nonequivalent atoms A and B give rise to a unit cell with four and six atoms in double and triple layer graphene systems, respectively. The Slonczewski-Weiss-McClure (SWM) model [37, 38] for the graphite has six constants γ_0, γ_1, γ_2, γ_3, γ_4 and γ_5 corresponding to a pair of atoms associated with the hopping processes.

Thus, the two linear electronic bands for a single graphene layer around the Fermi level are split into two or three energy bands according to the interlayer interaction between graphene layers. This energy band splitting plays an important role in determining the G' band shape and intensity in double and triple layer graphenes. For a given excitation laser energy $E_{\rm L}$, we get the different phonon wave vectors $\mathbf{q}$, since the initial electronic states $\mathbf{k}_i$ for the optical transitions are different for the different energy bands, and since there are several intermediate states for the different energy bands. We will neglect the splitting effect of the phonon branches in double and triple layer graphenes because of the very small splitting of these phonon branches (1.5 cm^{-1}) [32]. Figure 3.4 shows the

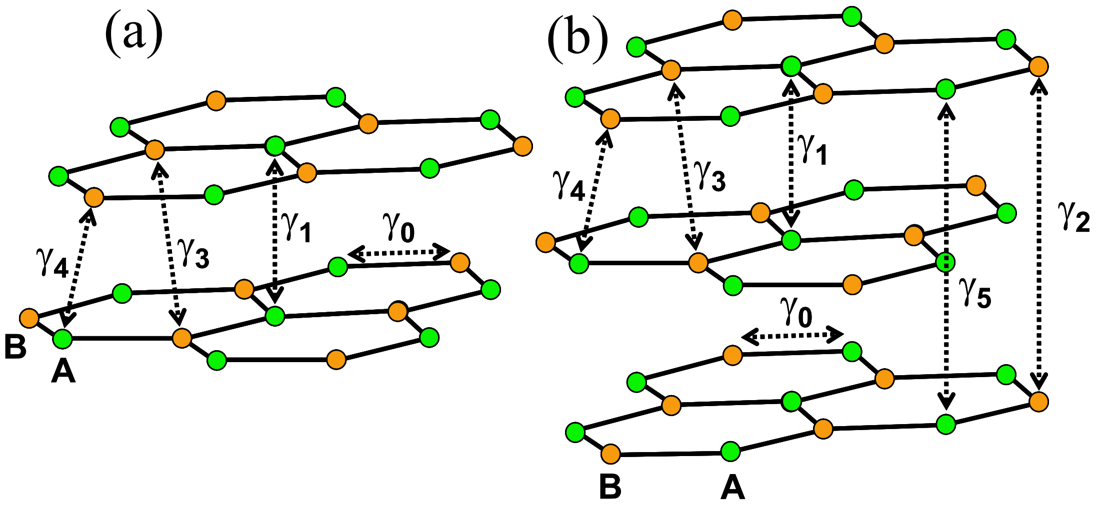

Figure 3.3: The atomic structure of (a) double layer graphene and (b) triple layer graphene. We distinguish the two inequivalent atoms A and B in each plane giving rise to a unit cell with four and six atoms for the double and triple layer systems, respectively. Since the unit cells of double and triple layer graphenes are the same for graphite in the Bernal stacking structure, the electronic energy dispersion relations of double and triple layer graphenes are represented in terms of the Slonczewski-Weiss-McClure (SWM) model for graphite. The SWM constants γ_0, γ_1, γ_2, γ_3, γ_4, and γ_5 are associated with the transfer integral calculated for the nearest neighbor atoms.

electronic energy band structure of the double and triple layer graphenes along the ΓKM direction. The electronic energy band structure of the double layer graphene around the Fermi level has two split parabolic bands in the valence and conduction bands. In the case of the triple layer graphene, there are two linear k bands between two convex parabolic conduction bands and two concave parabolic valence bands around the Fermi level. According to the theory [91], the electronic structure of the multi-layer graphene around the Fermi level depends on the number of layers n of the graphene, that is, if n is odd, the graphene has two-linear bands between $n-1$ convex parabolic conduction bands and $n-1$ concave parabolic valence bands, and if n is even, the graphene only has $2n$ parabolic bands.

Therefore, we can get two or three equi-energy contours in the conduction bands near the K and K' points for the double or triple layer graphenes, respectively, as shown in Fig.

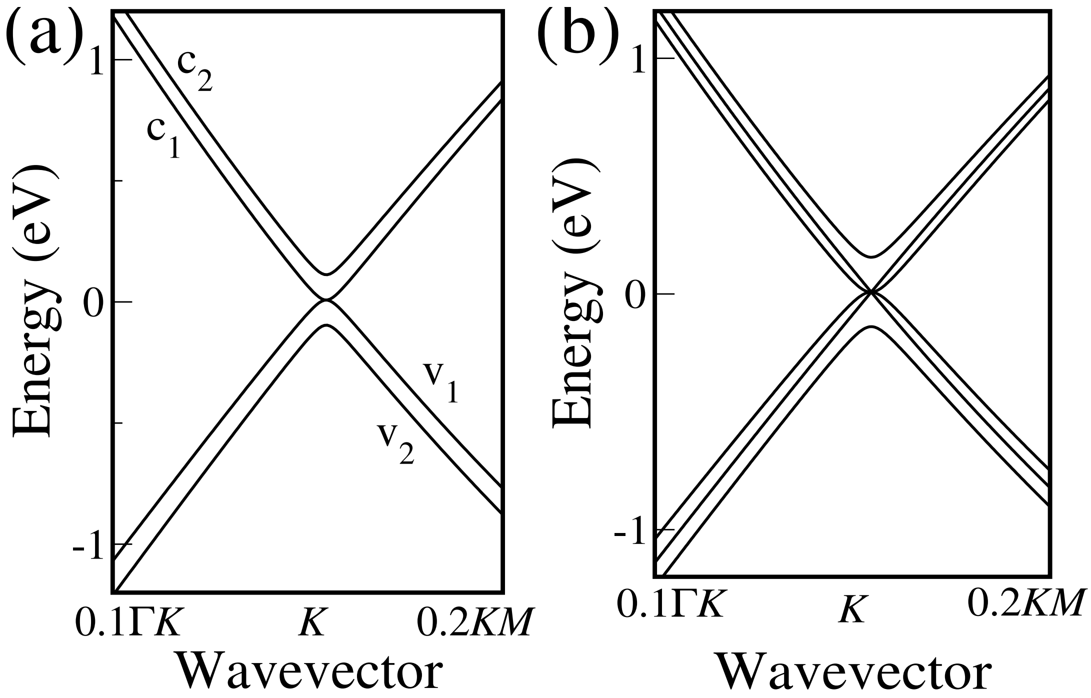

Figure 3.4: The electronic band structure of (a) double layer and (b) triple layer graphenes along the ΓKM direction. The electronic energy band around the Fermi level splits to two and three for the double and triple layer graphenes, respectively, compared with that of single layer graphene (see the Fig. 2.4).

3.5, because of the splitting of the energy bands around the Fermi level. The phonon state $\mathbf{q}$ is obtained from the resonance condition for the possible double resonance processes. In Fig. 3.5, the process P_{11} indicates scattering from the first equi-energy contour around the K point to the first equi-energy contour around the K' point, and the phonon wave vector becomes $\mathbf{q}_{11}$. In the case of the inter-valley scattering in the double layer graphene, we can get four types of the phonon wave vector, $\mathbf{q}_{11}$, $\mathbf{q}_{12}$, $\mathbf{q}_{21}$, and $\mathbf{q}_{22}$. These phonon wave vectors play a role to determine different subcomponents for the G' band of the double layer graphene, since the G' peak depends on the magnitude of the phonon wave vector. The magnitudes of four phonon wave vectors are enumerated by following:

$$|\mathbf{q}_{11}| > |\mathbf{q}_{12}| \sim |\mathbf{q}_{21}| > |\mathbf{q}_{22}|. \tag{3.4.3}$$

Therefore, this means that the G' band of the double layer graphene has three subcomponent peaks. Similarly, in the case of the triple layer graphene, there are nine different phonon wave vectors, $\mathbf{q}_{11}$, $\mathbf{q}_{12}$, $\mathbf{q}_{13}$, $\mathbf{q}_{21}$, $\mathbf{q}_{22}$, $\mathbf{q}_{23}$, $\mathbf{q}_{31}$, $\mathbf{q}_{32}$, and $\mathbf{q}_{33}$ The magnitude of these

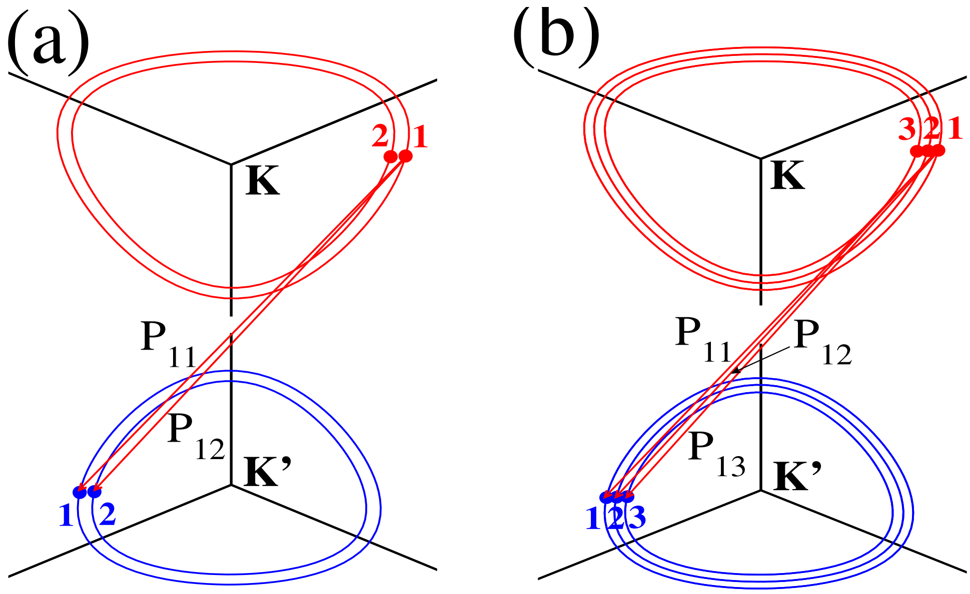

Figure 3.5: The equi-energy contours for (a) double layer and (b) triple layer graphenes around the K and K' points in the 2D Brillouin zone of the graphene. In double resonance scattering from K to K', there are four and nine possible optical processes for the double and triple layer graphenes, that is, for the double layer case, (1→1), (1→2), (2→1), (2→2), and for the triple layer case, (1→1), (1→2), (1→3), (2→1), (2→2), (2→3), (3→1), (3→2), (3→3). The above optical processes indicate each peak component for the G' band of the double and triple layer graphenes. For example, the (1→1) and (1→2) processes correspond to P_{11} and P_{12}, respectively.

nine phonon wave vector are enumerated by following:

$$|\mathbf{q}_{11}| > |\mathbf{q}_{12}| \sim |\mathbf{q}_{21}| > |\mathbf{q}_{13}| \sim |\mathbf{q}_{22}| \sim |\mathbf{q}_{31}| > |\mathbf{q}_{23}| \sim |\mathbf{q}_{32}| > |\mathbf{q}_{33}|. \tag{3.4.4}$$

As the result, the G' band of the triple layer graphene has five subcomponents peaks.

Chapter 4

Raman resonance window

In this Chapter, we show that Raman resonance windows of different (n, m) SWNTs strongly depend on chirality and diameter. As explained in Section 3.3, in order to calculate the resonance window, we have to consider the electron-phonon scattering matrix elements, the density of state (DOS) at a final state, and the phonon occupation number. For the electron-phonon scattering, we select 48 scattering processes, that is, intra- and inter-valley, forward and backward, phonon emission and absorption, and six phonon modes. For the semiconducting SWNTs (s-SWNTs), the DOS at a final state depends on the S1 and S2 types due to the trigonal warping effect [92] around the K point in the 2D Brillouin zone of the graphene sheet. The calculated resonance window values are directly compared with the Raman spectral widths observed in the experiment. In the case of metallic SWNTs (m-SWNTs), the calculated resonance window values deviate from those for the experiment. We expect that the plasmon by free carrier excitation might contribute to the metallic Raman resonance windows.

4.1 Electron-phonon scattering processes

Theoretical Raman resonance window γ can be simply expressed as the electron-phonon scattering probability of Eq. (3.3.5) since the relaxation time τ is an inverse of the scattering probability:

$$\gamma = \frac{\hbar}{\tau} = \hbar \sum_{\mathbf{k}', \nu} W^{\nu}_{\mathbf{k} \to \mathbf{k}'}. \tag{4.1.1}$$

In this Section, we describe the electron-phonon scattering processes for the resonance

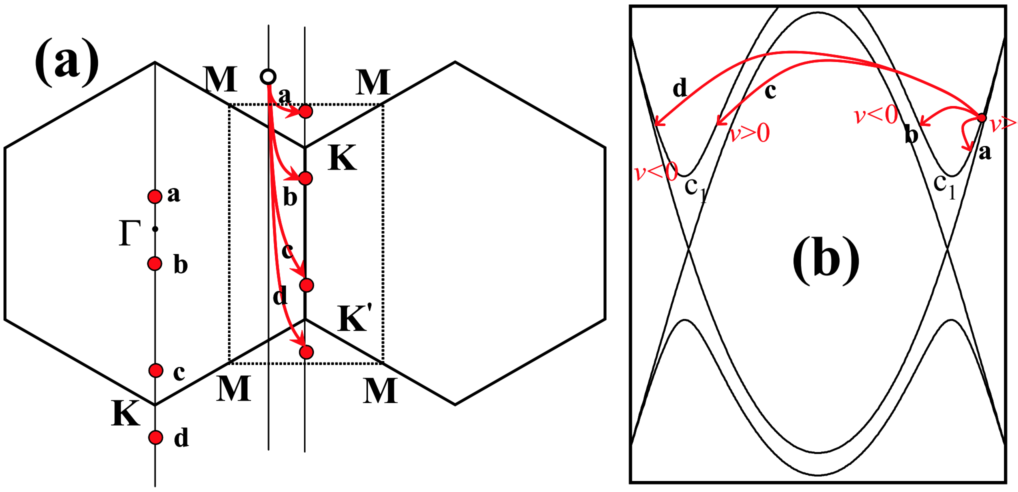

Figure 4.1: (a) The schematic electron-phonon scattering processes around the K and K' points of armchair SWNT. The open circle near the K point indicates an initial $\mathbf{k}$ state in the first conduction band c_1 for the m-SWNTs. The scattering processes (arrows) for **a** and **b** indicate the intra-valley forward and backward scatterings, preserving or changing the sign of the group velocity, respectively, and the corresponding phonon modes are shown around the Γ point. In the electron-phonon scattering from K to K' point, the processes **c** and **d** indicate inter-valley forward and backward scatterings, respectively, and the corresponding phonon modes are shown around the bottom K point. The electron-phonon matrix elements depend on the $K\Gamma$ and KM direction, and then the corresponding forward and backward scattering electron-phonon matrix elements may have a quite different value compared with the backward scattering. (b) The energy band of (10,10) SWNT.

windows of s- and m-SWNTs.

4.1.1 Semiconducting SWNTs

A photo-excited electron in the second conduction band c_2 relaxes to a different state according to the electron-phonon interaction, with requiring the energy-momentum conservation. For each phonon mode and for each energy band, we have (1) the emission and absorption scatterings, (2) the intra- ($K \rightarrow K$ or $K' \rightarrow K'$) and inter-valley ($K \rightarrow K'$ or $K' \rightarrow K$) scatterings, and (3) the forward and backward scatterings, as shown in Figs. 4.1 and 4.2. In order to consider the intra- and inter-valley scatterings, we select a cutting

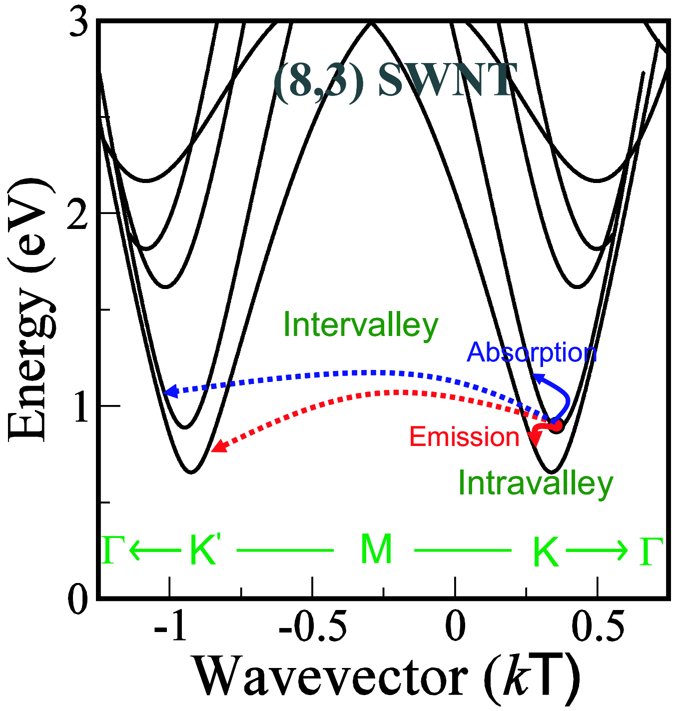

Figure 4.2: The electron-phonon scattering processes of a photo-excited electron from the second conduction band of (8,3) SWNT. The intra- and inter-valley scatterings indicate the transition processes from $K(K')$ to $K(K')$ and from $K(K')$ to $K'(K)$, respectively. For the intra-valley scattering, the phonon wave vector has the value $\mathbf{q} \sim 0$, while $\mathbf{q} \sim 2\mathbf{k}$ for the inter-valley scattering. Since there are six phonon branches, we expect 48 final $\mathbf{k}'$ states for an initial $\mathbf{k}$ state of each conduction energy sub-band.

line to cover both K and K' regions by extending the cutting line to the $\mathbf{K}_2$ direction. We select four M points in the KK' directions and connect four M points around the K and K' point as a rectangular region (see Fig. 4.1 (a)), and then we can make cutting lines within the rectangular region around the K and K' points. Figure 4.2 shows the electron-phonon scattering processes of a photo-excited electron in the conduction band of (8,3) SWNT which are obtained by selecting the cutting lines within the rectangular region around the K and K' points. The intra- and inter-valley scatterings involve the Γ point and K point phonon modes, respectively, as shown in Figs. 4.1 and 4.2. We should mention that the Γ point phonon wave vector has the value $\mathbf{q} \sim 0$, while the K point phonon wave vector has the value $\mathbf{q} \sim 2\mathbf{k}$. The optical phonon modes at the Γ and K points are related to the G and G' bands, respectively, in the Raman spectra of SWNTs.

The intra- (or inter-) valley scattering consists of the forward and backward scatterings as shown in Fig. 4.1. The forward and backward scatterings are determined by the change of the sign for the group velocity of photo-excited electron $\partial E/\partial k$ in the energy band. Namely, the forward scattering preserves a sign of the group velocity, while the backward scattering changes a sign of the group velocity, as shown in Fig. 4.1 (b). The intra-valley forward and backward scatterings occur from K (K') to K (K') point (processes **a** and **b**, respectively, in Fig.4.1), and have a phonon wave vector $\mathbf{q} \sim 0$ around the Γ point. The inter-valley forward and backward scatterings occur from K (K') to K' (K) point (process **c** and **d**, respectively, in Fig.4.1), and have a phonon wave vector $\mathbf{q} \sim 2\mathbf{k}$ around the K point.

In graphene, there are six phonon modes, i.e., out-of-plane transverse acoustic (oTA), in-plane transverse acoustic (iTA), in-plane longitudinal acoustic (iLA), out-of-plane transverse optical (oTO), in-plane transverse optical (iTO), and longitudinal optical (iLO) modes listed in order of increasing phonon frequency. These phonon modes can be applied to carbon nanotube by zone-folding method. Therefore, since we have six branches of phonon modes in the SWNT, we expect 48 $\mathbf{k}'$ final states for each initial state $\mathbf{k}$ of each energy sub-band [12]. As an initial state $\mathbf{k}$, we consider only a photo-excited electron in the bottom of the second conduction band c_2 (E_{22}) which relaxes to the first conduction band c_1 , because only a few photo-excited electrons contribute to the scattering process, and the relaxation rate by a phonon is 1000 times faster (0.1 ps) than the photon emission process (0.1 ns) [59]. Thus, since the initial group velocity is zero, the forward and backward scatterings are replaced with the scatterings along the high symmetry lines KM and $K\Gamma$, in which we simply call KM and $K\Gamma$ direction scatterings.

Figure 4.3 shows that the intra-valley scattering is mostly associated with 5 types of phonon modes, namely, the LO, iTO, oTO, LA, and RBM phonon modes. We can exclude the iTA phonon mode, because of the flatness of the phonon dispersion curves near the Γ point. The electron-phonon couplings with the LO, RBM, and oTO phonon modes of the six phonon modes are stronger than others and in particular, the LO phonon is the strongest due to the longitudinal vibration of the C-C bond. In Fig. 4.3, the green- and orange-filled solid circles represent the KM and $K\Gamma$ direction scatterings, respectively. In the RBM electron-phonon matrix elements, the KM direction scattering is certainly stronger than the $K\Gamma$ direction. The electron-phonon matrix elements around the K point

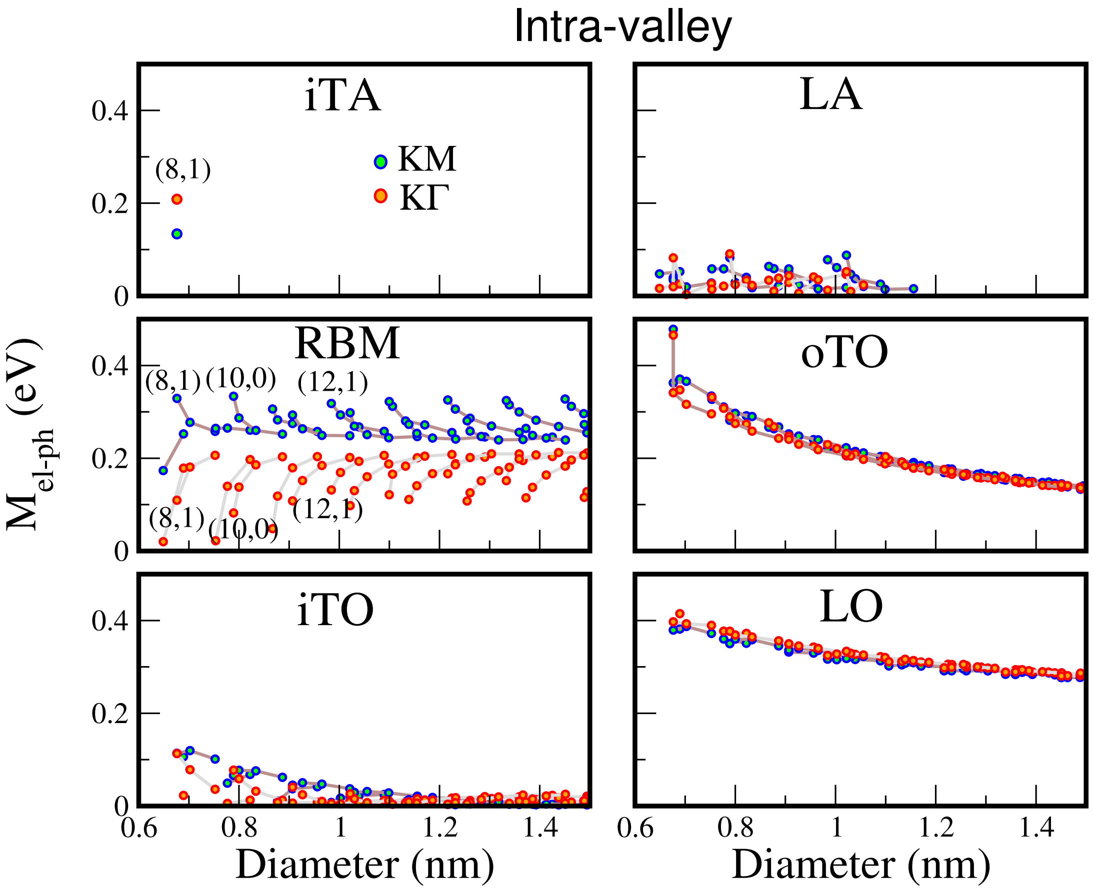

Figure 4.3: Intra-valley electron-phonon scattering matrix elements of a photo-excited electron for the s-SWNT at the E_{22} transition. We calculate six electron-phonon matrix elements for six phonon modes, iTA, LA, RBM, oTO, iTO, and LO. We exclude the calculation of relaxation process less than the cut-off energy 0.02 eV.

are sensitive to the electron wave vector. Therefore, the RBM matrix element in the $K\Gamma$ direction has a quite different value from that in the KM direction. We exclude the electron-phonon scattering with phonon energy less than 0.02 meV for simplicity. Since we calculate the Raman resonance window within $0.6 < d_t < 1.5$ nm, the RBM Raman spectra is in the range $0.02 < \hbar\omega_{\rm RBM} < 0.05$ eV. Therefore, most of iTA and some of LA phonon modes for the different (n, m) SWNTs are out of this range (see Fig. 4.3).

The inter-valley electron-phonon scattering corresponds to the phonon modes near the K point, including all six phonon modes, since these all phonon modes have a large phonon DOS in the vicinity of the K point. Among the six phonon modes, the LO and LA modes give the strongest electron-phonon coupling and thus contribute strongly to relaxation

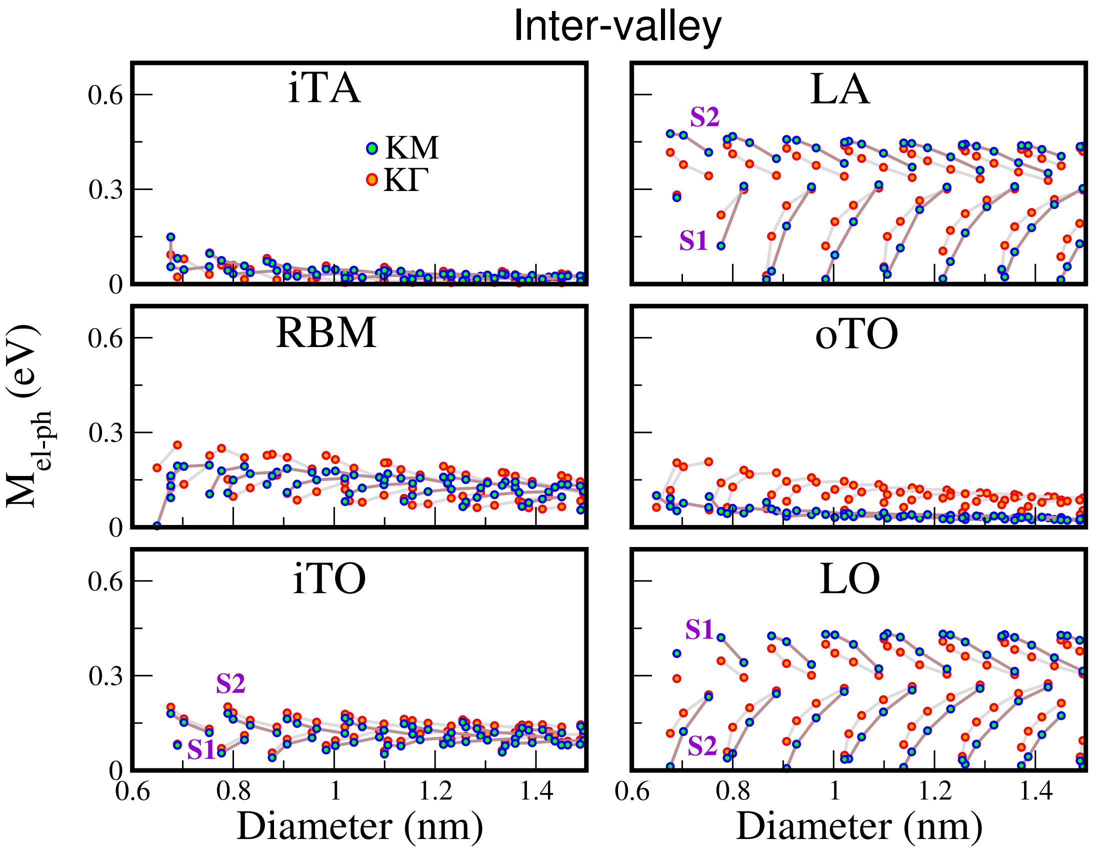

Figure 4.4: Inter-valley electron-phonon scattering matrix elements of s-SWNT at E_{22} transition. Green-filled and orange-filled solid circles represent KM and $K\Gamma$ direction scatterings, respectively. The family spread strongly appears in LO and LA electron-phonon scattering.

processes compared with the other modes, as shown in Fig. 4.4. The electron-phonon matrix elements for the LO and LA phonon modes depend on the $S1$ and $S2$ types which were explained in Section 2.2. For the LO phonon mode, the electron-phonon matrix elements for the $S1$ type are larger than that for the $S2$ type, while for the LA phonon mode, the electron-phonon matrix elements for the $S1$ type are smaller than that for the $S2$ type. For the oTO electron-phonon matrix elements, the scattering in the $K\Gamma$ direction is stronger than that in the KM direction. Interestingly, for the LO and LA phonon modes, the family spread for the KM direction scattering is broader than that for the $K\Gamma$ direction. Here, the family spread means the spread of the matrix elements within the same $2n+m$ =constant family which is connected by the gray and brown lines

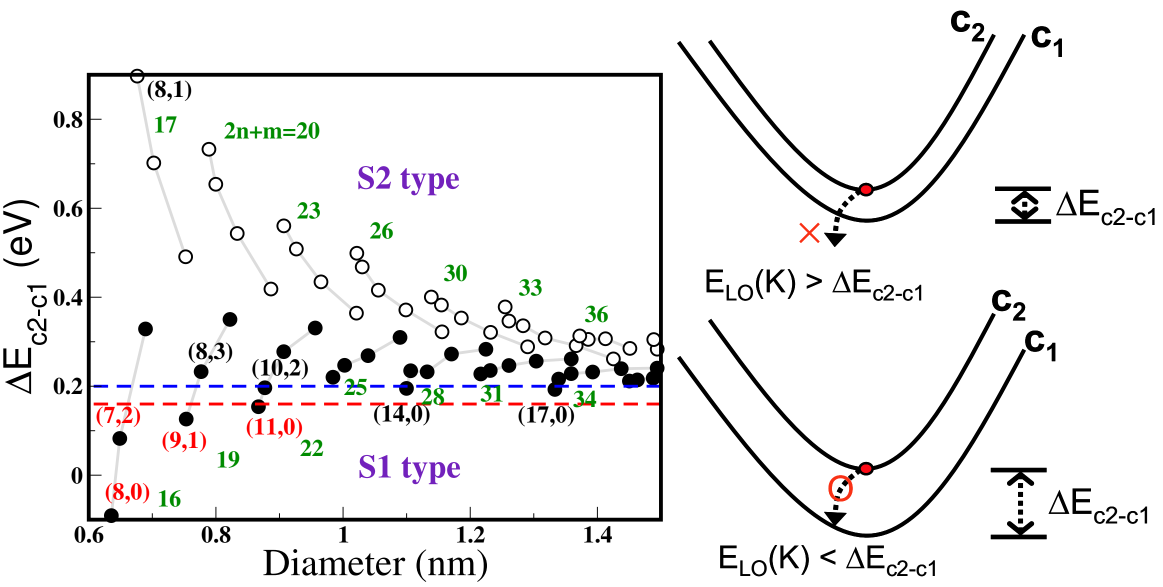

Figure 4.5: Energy differences $\Delta E_{c_2-c_1}$ at the energy extrema between the c_1 and c_2 conduction bands. Filled and open circles denote the S1 type and S2 type SWNTs, respectively, as explain in Chapter 2. Red and blue dashed lines indicate the LO phonon energy at the K(0.16 eV) and Γ(0.20 eV) points of the phonon dispersion relations, respectively. If the energy difference $\Delta E_{c_2-c_1}$ is smaller than the energy (0.16 eV) of the K point LO phonon, the electron-phonon scattering from the energy extrema of c_2 band to c_1 band is *restricted* (see right-top and bottom figure). The red color (n, m) SWNTs have smaller $\Delta E_{c_2-c_1}$ than the LO phonon energy at the K point. In left plot, the green color numbers represent $2n + m$ =constant families.

in Fig. 4.4. While the intra-valley scattering gives almost same matrix elements for the KM and $K\Gamma$ direction scatterings except for the RBM phonon mode, the inter-valley scattering gives quite different matrix elements for the KM and $K\Gamma$ direction scatterings, as shown in Figs. 4.3 and 4.4.

In a relaxation process, the energy difference between two neighbor conduction bands gives the restriction on the electron-phonon scattering. In Fig. 4.5, we make a plot for the energy difference between the conduction bands, c_2 and c_1, as a function of tube diameter for the $S1$ and $S2$ type SWNTs as defined in Section 2.2. The red and blue dashed lines in Fig. 4.5 (left) indicate the LO phonon energy at the K (0.16 eV) and Γ (0.20 eV) points in the Brillouin zone of the graphene sheet, respectively. If the energy difference

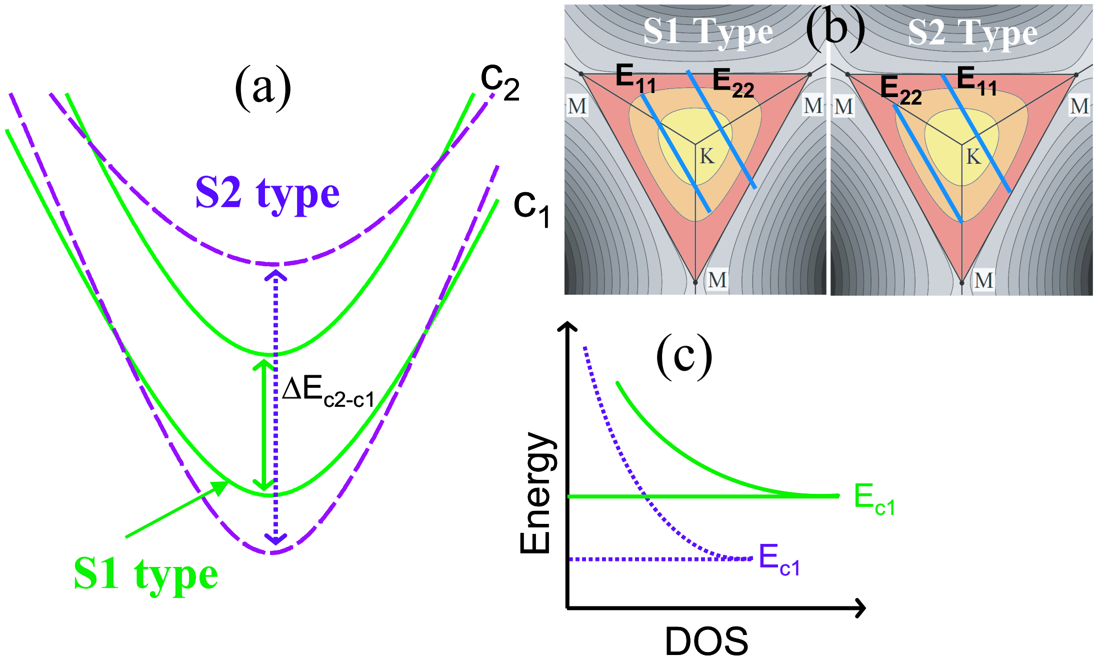

Figure 4.6: (a) The energy dispersion in the conduction bands c_1 and c_2. The energy bands for the S1 type and S2 type SWNTs are plotted by the green solid lines and the violet dashed lines, respectively. For comparing the S1 type conduction bands with the S2 type, we overlap these conduction bands for the two types of tubes at the **k** axis. (b) The trigonal warping effect around the K point in the 2D graphene Brillouin zone. The flat side of the trigonal equi-energy contour faces on the $K\Gamma$ direction, and the corner side faces on the KM direction. (c) The density of states (DOS) plot as a function of energy shows that the DOS of the S1 type is larger than that of the S2 type at the E_{c_1}.

$\Delta E_{c_2-c_1}$ is less than 0.16 eV, the electron-phonon scattering with phonon energy more than 0.16 eV cannot occur due to the energy conservation, as shown in Fig. 4.5 (right). Thus, (8,0), (7,2), (9,1), and (11,0) SWNT which have $\Delta E_{c_2-c_1}$ less than 0.16 eV cannot emit the LO and iTO phonon energies in intra- and inter-valley scatterings because of the energy conservation requirements, and a relatively long lifetime (small γ value) is obtained for these tubes (we will show it in Fig. 4.14 (a)). It should be mentioned that $\Delta E_{c_2-c_1}$ for (8,0) nanotube is negative by the definition of the c_1 and c_2 energy bands, in which the c_1 (c_2) band is defined not by the energy band bottom, but by the cutting line closest (next closest) to the K point of the 2D Brillouin zone. The SWNTs lying on the blue dashed lines, such as (10,2), (8,3), (14,0) and (17,0), are remarkably resonant with the LO phonon mode at the Γ and K points. Because, the $S1$ type SWNTs have a larger DOS at the final state in the c_1 band than the $S2$ type as shown in Fig. 4.6 (c), and the Raman resonance window is proportional to the final DOS as explained in Section 3.3. The schematic figure for the energy difference $\Delta E_{c_2-c_1}$ is shown in Fig. 4.6 (a). The energy difference $\Delta E_{c_2-c_1}$ shows the family pattern for both $S1$ and $S2$ type SWNTs, and we see that $\Delta E_{c_2-c_1}(S1 \text{ type}) < \Delta E_{c_2-c_1}(S2 \text{ type})$, as shown in Fig. 4.5. The reason why the $S1$ and $S2$ type SWNTs have different $\Delta E_{c_2-c_1}$ family spread pattern is due to the trigonal warping effect around the K point of the 2D Brillouin zone, as shown in Fig. 4.6 (b). In Fig. 4.6 (b), two cutting lines of the $S1$ type SWNT exist in the same equi-energy contour, but those of the $S2$ type exist in the different equi-energy contours due to the trigonal warping effect which results from the energy distortion with a triangular asymmetry around the K point in the reciprocal space of the graphene sheet [92]. The energy dispersion of the grahene quickly increases along the $K\Gamma$ direction compared with the KM direction. This means that the E_{11} and E_{22} cutting lines of the $S2$ type SWNTs have lower and higher vHS than those of the $S1$ type, respectively.

Thus, the *resonance* or *restriction* effects related to phonon scattering appear only for the $S1$ type SWNTs due to two reasons, small energy difference $\Delta E_{c_2-c_1}$ and large final DOS due to the trigonal warping effect as explained above. In Fig. 4.6, while the two conduction bands for the $S1$ SWNTs (solid green lines) are parallel to each other, the two curvatures for the $S2$ SWNTs (dashed violet lines) are different from each other, i.e. the curvature for the c_1 band is larger than the curvature for the c_2 band. Figure 4.6 (b) also shows the reason why the curvatures of the $S1$ type at the c_1 band are smaller than those of the $S2$ type. The trigonal warping effect around the K point makes the flat side of trigonal equi-energy contour face on the $K\Gamma$ direction and the corner side face on the KM direction, resulting in large energy band curvature of the cutting line in the KM direction. Accordingly, the DOS, $(dE/dk)^{-1}$, of the final state for a photo-excited electron which relaxes from the bottom point of the c_2 band to c_1 band depends on whether they are $S1$ or $S2$ type SWNTs, since DOS($S1$ type)>DOS($S2$ type) as shown in Fig. 4.6 (c).

By considering the relation between the electron-phonon matrix elements and the final state DOS, we can obtain the Raman resonance windows for different (n, m) s-SWNTs which a photo-excited electron in the bottom of c_2 band relaxes to the final

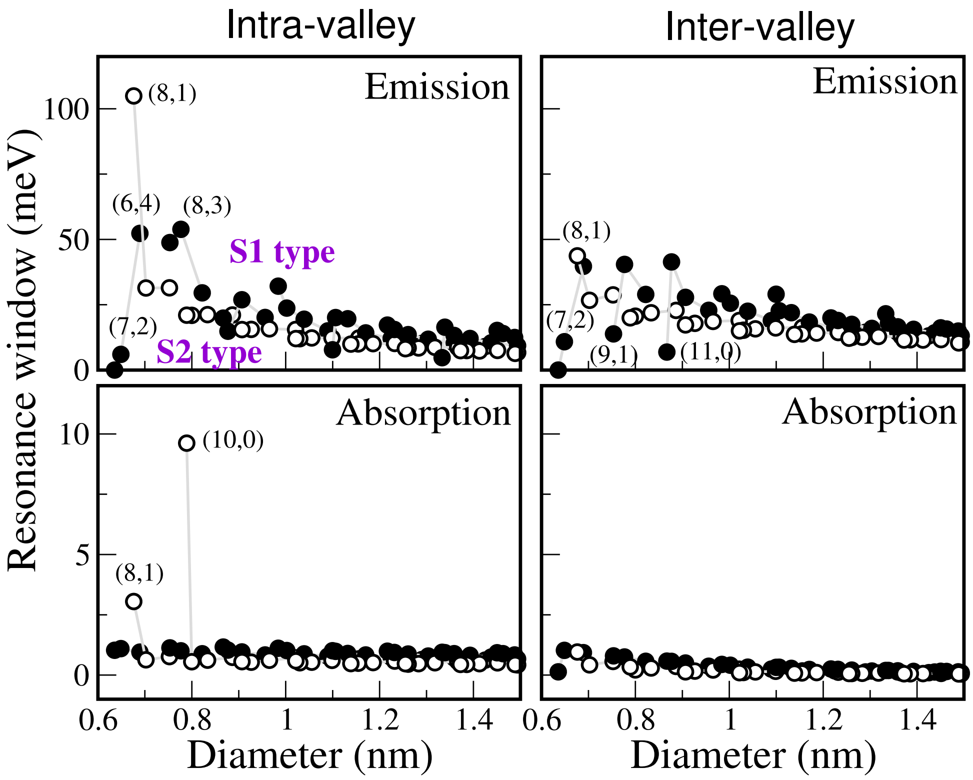

Figure 4.7: Resonance Raman window for intra- (left) and inter-valley (right), emission (top) and absorption (bottom) scattering processes. Filled and open circles represent the $S1$ and $S2$ type, respectively.

states, satisfying the energy-momentum conservation. Before getting the total resonance window which makes a summation of each scattering process, first of all, it is useful to compare the contribution of the resonance window from each scattering process in order to understand completely the Raman resonance window of carbon nanotube system.

Figure 4.7 shows that the resonance windows for the intra-valley scattering as a function of SWNT diameter are almost the same as those for the inter-valley scattering except for (8,1) tube, even though the electron-phonon matrix elements depend on the Γ and K point phonon modes as shown in Figs. 4.3 and 4.4. Interestingly, the emission process gives much larger the resonance windows for different (n, m) SWNTs than the absorption process. In Eq. (3.3.3), the phonon occupation number $n_\nu(\mathbf{q})$ for the absorption decrease exponentially with increasing the phonon energy at the room temperature, in which $n_\nu(\mathbf{q})$ values of the LO phonon at the Γ and K points are about 4.4×10^{-4} and 2.1×10^{-3}, respectively, while $n_\nu(\mathbf{q})$ for the cut-off phonon energy 0.02 eV is about 0.86.

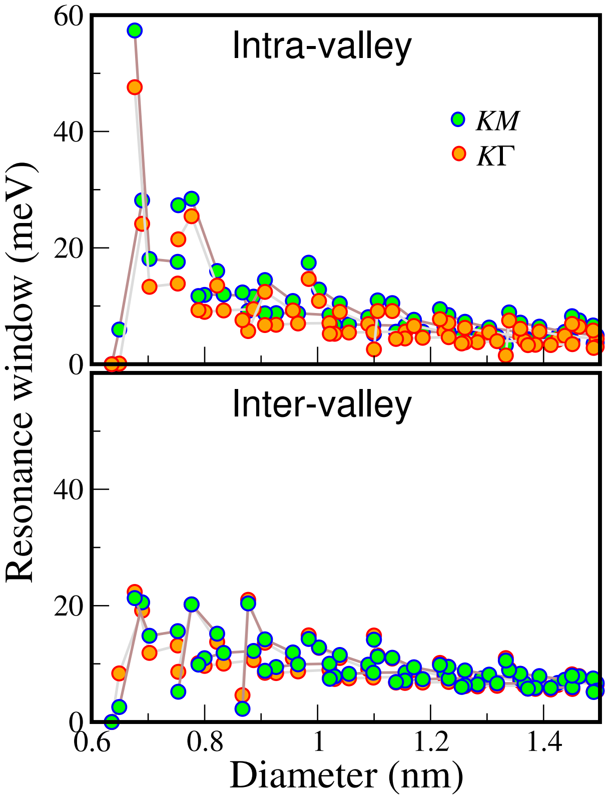

Figure 4.8: Comparison of the KM direction and $K\Gamma$ direction resonance windows for the intra- and inter-valley scattering processes, respectively. Green-filled and orange-filled circles represent the KM and $K\Gamma$ direction scatterings, respectively.

Therefore, the absorption process for the Raman resonance window calculation can be neglected except for (8,1) and (10,0) SWNTs as shown in Fig. 4.7. In the case of the emission process, $1 < n_\nu(\mathbf{q}) + 1 < 1.86$ in the phonon energy range $0.02 < E_{\mathrm{ph}} < 0.2$ eV. Thus, the emission scattering process is dominant in relaxation processes. As motioned above, the $S1$ type SWNTs have larger resonance windows than the $S2$ type.

Figure 4.8 shows the resonance windows of the KM and $K\Gamma$ direction scatterings for the intra- and inter-valley scattering processes, respectively. For the intra-valley scattering, the resonance windows for the KM direction scattering are slightly larger than those for the $K\Gamma$ direction scattering due to the RBM phonon mode as shown in Fig. 4.3. For the inter-valley scattering, the resonance windows for the KM direction scattering are similar to those for the $K\Gamma$ direction scattering because of the similar electron-phonon matrix elements for these two directions as shown in Fig. 4.4.

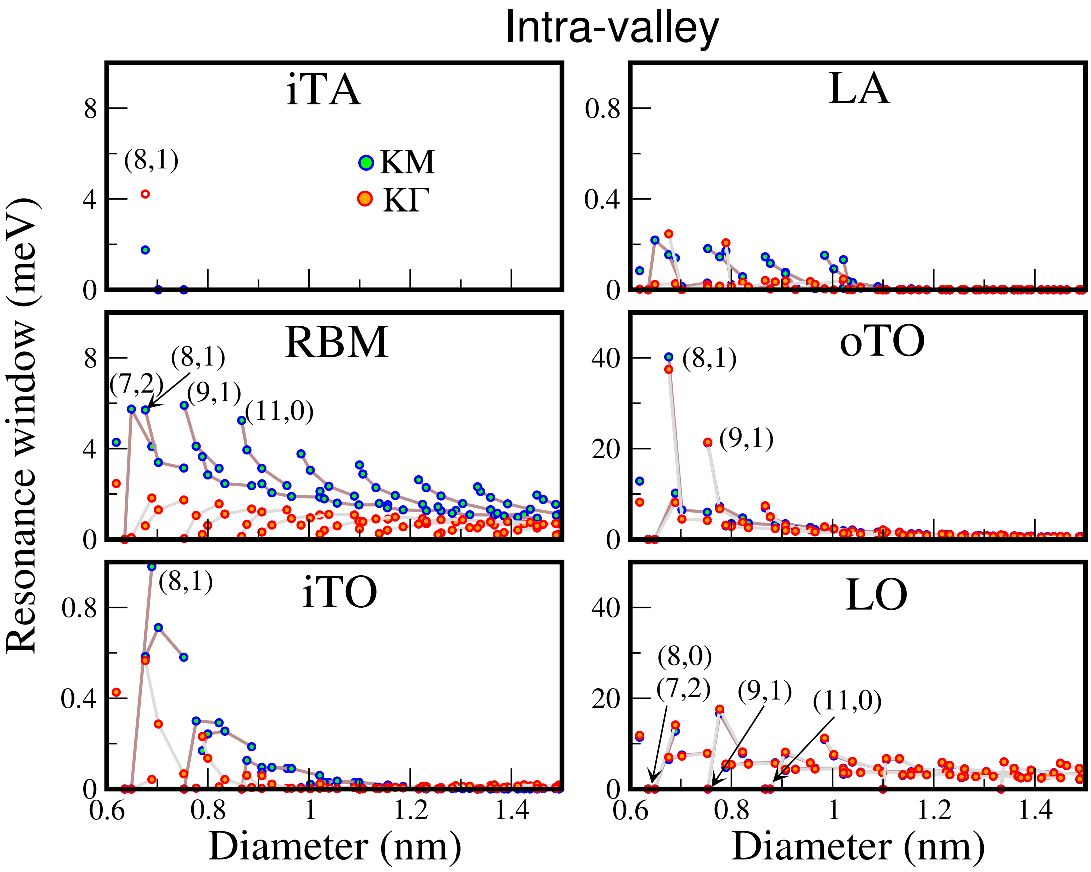

Figure 4.9: Resonance windows for six Γ point phonons for intra-valley scattering. Green-filled and orange-filled circles represent KM and $K\Gamma$ direction scatterings, respectively.

Figure 4.9 shows the resonance windows for six Γ point phonon modes which are relevant to the intra-valley scattering. The contributions to the resonance windows from the LO, oTO, and RBM phonon modes are larger than those of the other phonon modes. For the RBM phonon mode, the resonance windows of the KM direction scattering ($2 < \gamma_{\mathrm{RBM}} < 6$ meV) is quite larger than the $K\Gamma$ direction scattering ($0 < \gamma_{\mathrm{RBM}} < 2$ meV). Also, s-SWNTs near zigzag ($\theta \sim 0^\circ$) such as (7,2), (8,1), (9,1), and (11,0) have relatively large resonance windows for the KM direction scattering, while for $K\Gamma$ direction scattering, the values are almost zero. The resonance windows of the oTO phonon mode are in the range $\gamma_{\mathrm{oTO}} < 13$ meV except for (8,1) and (9,1) SWNTs. (8,1) and (9,1) SWNTs have the resonance window values 40 and 21 meV, respectively. For the LO phonon mode, all resonance windows are in the range less than 20 meV. In particular, the relaxation processes for (8,0), (7,2), (9,1), and (11,0) are restricted as explained in Fig.

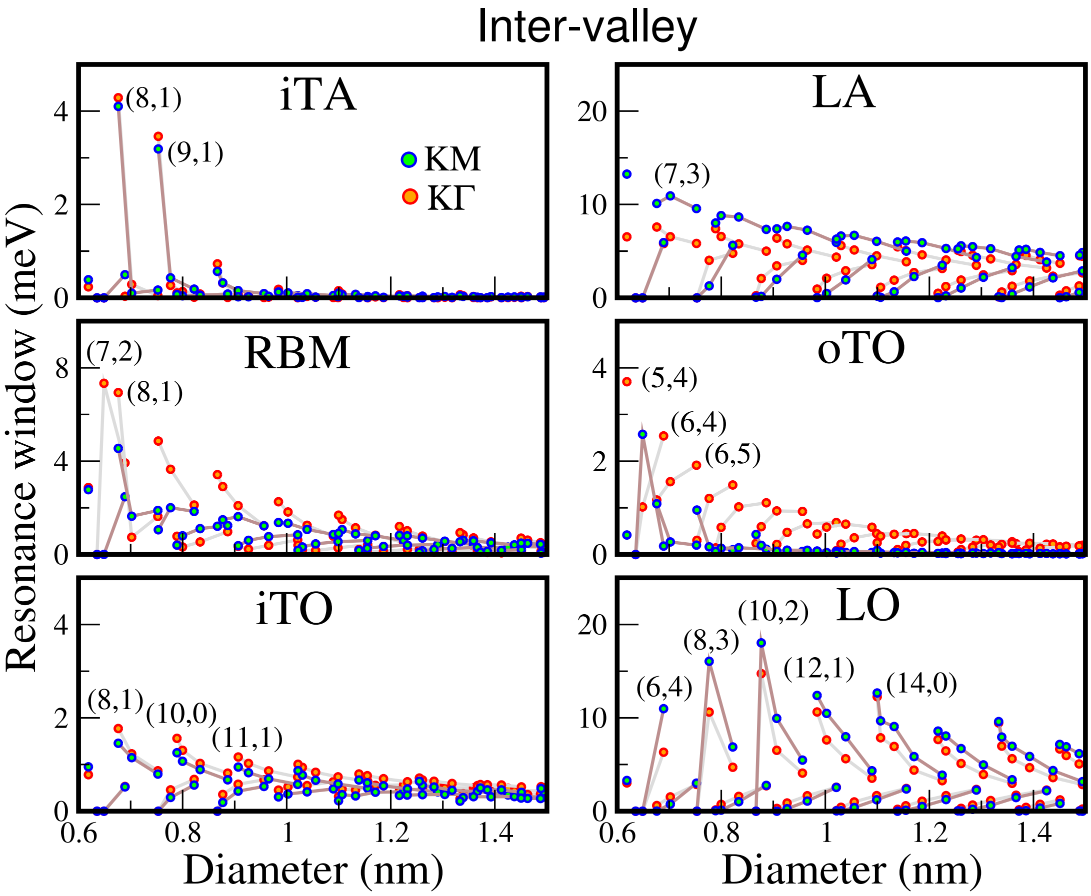

Figure 4.10: Resonance windows for six K point phonon modes for the inter-valley scattering. Green-filled and orange-filled circles represent the KM and $K\Gamma$ direction scatterings, respectively.

4.5, and thus the values of resonance window are suppressed. The LA and iTO phonon modes have very small resonance windows in the range less than 1 meV.

The inter-valley scattering processes for each phonon mode give different behaviors from intra-valley scattering processes as shown in Fig. 4.10. The contributions to the resonance windows from the LO and LA phonon modes show a strong family spread and they are larger than the other phonon modes, that is, $\gamma_{\text{LO}} < 20$ meV, $\gamma_{\text{LA}} < 15$ meV. Similar to the intra-valley scattering, the relaxation processes of (8,0), (7,2), (9,1), and (11,0) SWNTs are restricted for the LO phonon mode. As shown in Fig. 4.10, the resonance windows of the KM direction scattering for LO and LA phonon modes have broader family spread than that of the $K\Gamma$ direction scattering. For the oTO phonon

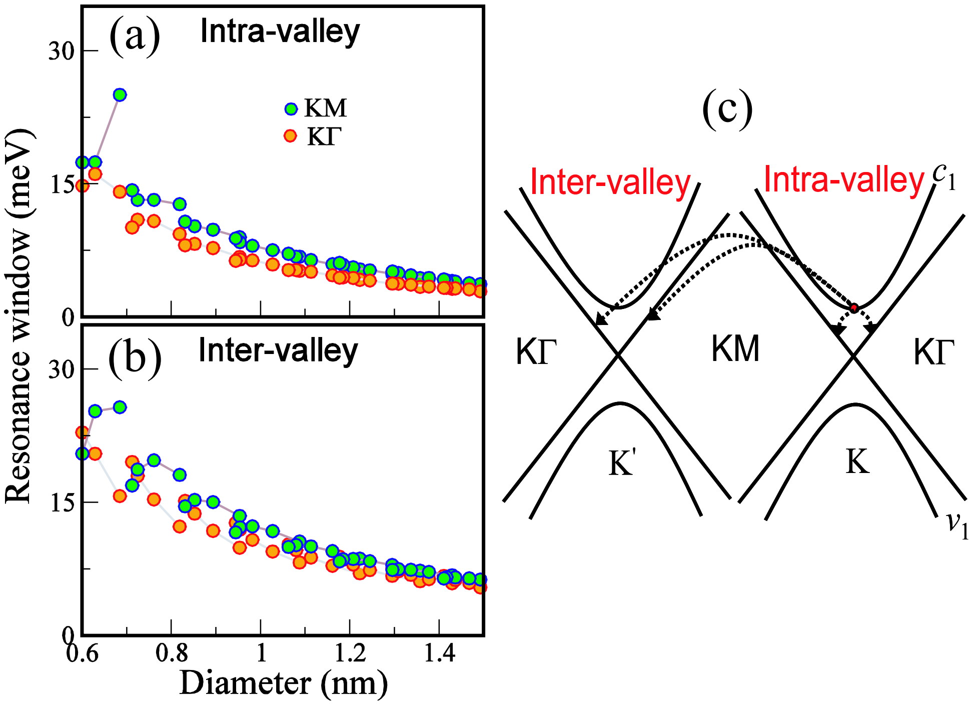

Figure 4.11: Comparison of the KM direction and $K\Gamma$ direction resonance windows for (a) the intra- and (b)inter-valley scattering processes in *metallic* SWNT, respectively. Green-filled and orange-filled circles represent the KM and $K\Gamma$ direction scatterings, respectively. (c) Relaxation processes from the first conduction band c_{1L} to two linear band for the *metallic* SWNTs. The inter- and intra-valley scatterings are divided into two scatterings along the KM and $K\Gamma$ directions, respectively. We consider the scattering which a photo-excited electron relaxes from the c_{1L} band (or c_{1H}) to two linear metallic bands (or to c_{1L}).

mode, the $K\Gamma$ direction scattering has larger resonance windows than the KM direction scattering. The resonance windows for the iTO phonon mode show a relatively narrow family spread and are in the range less than 2 meV.

4.1.2 Metallic SWNTs

Next, we consider the electron-phonon scattering process for the relaxation process of metallic (m-) SWNTs. A photo-excited electron in the c_{1L} band scatters to a metallic energy band by interaction with a phonon, satisfying energy-momentum conservation,

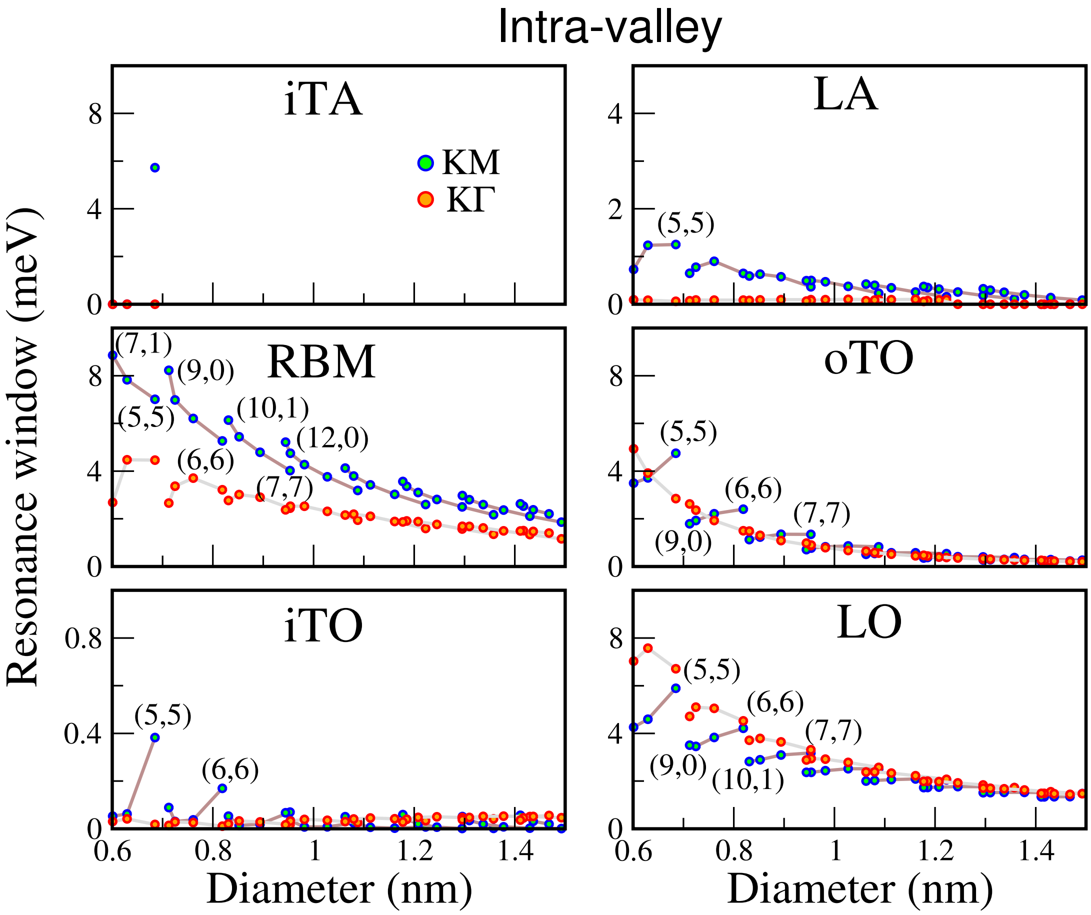

Figure 4.12: Resonance windows for six Γ phonon of *metallic* SWNT in the intra-valley scattering. Green-filled and orange-filled circles represent the KM and $K\Gamma$ direction scatterings, respectively.

as shown in Fig. 4.11 (c). The γ value is obtained by calculating the electron-phonon scattering probability which a photo-excited electron in the bottom of the $c_{1\mathrm{L}}$ band (or $c_{1\mathrm{H}}$) relaxes to two linear energy bands (or to $c_{1\mathrm{L}}$), after E_{11}^{L} (or E_{11}^{H}) optical transition. Here, H and L denote higher and lower energy for the metallic E_{11} energy band. In this Section, we explain only for the case of the E_{11}^{L} transition because of the similar scattering process with the E_{11}^{H} transition. We will show both calculated resonance windows in the final result. We consider the same scattering processes as for s-SWNTs to calculate the scattering probability of m-SWNTs. Figure 4.11 (a-b) shows the resonance windows of the KM and $K\Gamma$ direction scatterings for the intra- and inter-valley scattering processes, respectively, when a photo-excited electron in the c_{1L} band scatters to two linear bands.

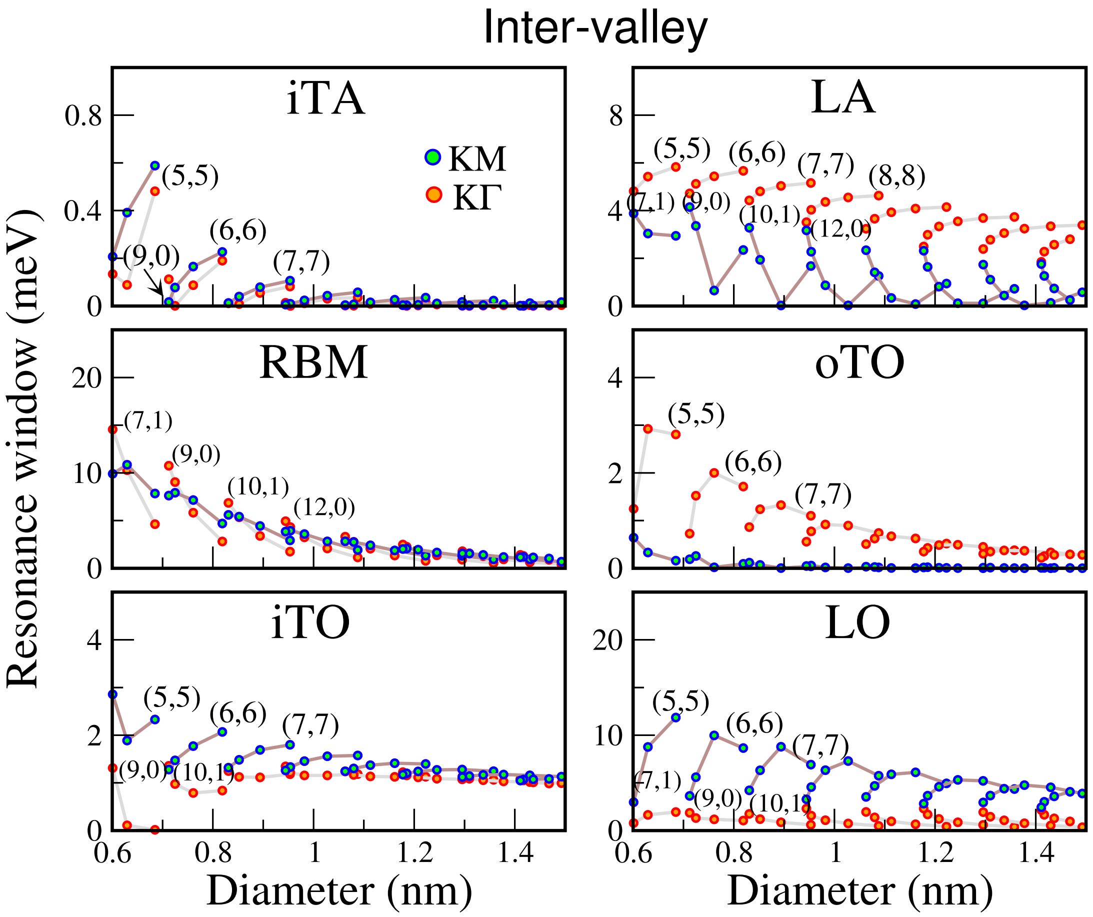

Figure 4.13: Resonance windows for six K phonon of *metallic* SWNT in the inter-valley scattering. Green-filled and orange-filled circles represent the KM and $K\Gamma$ direction scatterings, respectively.

The KM direction scattering has relatively larger resonance windows than the $K\Gamma$ direction scattering for the intra- and inter-valley scatterings, respectively. The resonance windows of both intra- and inter-valley scatterings are inversely proportional to SWNT diameter. In m-SWNT, the inter-valley scattering gives relatively larger resonance windows than the intra-valley scattering.

Also, we consider the electron-phonon scattering processes for six phonon modes when a photo-excited electron in the c_{1L} band to scatter to the two linear bands. Figure 4.12 shows the resonance windows for each phonon mode in the intra-valley scattering. The RBM phonon mode gives quite larger resonance windows for the scattering in the KM direction than those for the scattering in the $K\Gamma$ direction. In metallic E_{11}^{L} transition, the resonance windows for the RBM and LO phonon modes are larger than those for other phonon modes. For the m-SWNTs with small diameter, the electron-phonon scattering probability by the RBM mode is the strongest, while the scattering probability by the iTO mode is very small compared with the RBM scattering. Because of the curvature effect, for the electron-phonon matrix element, the RBM phonon mode becomes large [12]. For the LO phonon mode, the $K\Gamma$ direction scattering near the zigzag SWNT ($\theta \sim 0°$) gives relatively larger resonance window than the KM direction scattering, while both direction scatterings have similar resonance window near the armchair SWNT ($\theta \sim 30°$).

Figure 4.13 shows the resonance windows for six K point phonon modes in the intervalley scattering. The RBM, LA, and LO phonon modes have larger resonance windows than others. For the LA phonon mode, the resonance windows near the zigzag SWNT ($\theta \sim 0°$) give similar values between the KM direction and $K\Gamma$ direction scatterings, while the contributions to the resonance windows from both direction scatterings near the armchair SWNT ($\theta \sim 30°$) give large difference. Also, the contributions to the resonance windows from the scattering in the $K\Gamma$ direction for the oTO phonon mode are larger than those from the scattering in the KM direction. For iTO and LO phonon modes, the scattering in the KM direction is larger than that in the the $K\Gamma$ direction.

In next Section, we show the total Raman resonance window for 48 electron-phonon scattering processes for s- and m-SWNTs, respectively, and compare with experiment.

4.2 Calculated result of resonance windows

Figure 4.14 (a) shows a plot of the resonance windows (hereafter, γ value) of s-SWNTs for all possible relaxation processes which a photo-excited electron in the bottom of c_2 band relaxes to the c_1 band. The γ values for different (n, m) s-SWNTs in Fig. 4.14 (a) are derived by substituting the electron-phonon scattering probability in Eq. (3.3.5) into Eq. (4.1.1). In Fig. 4.14 (a), the γ values are inversely proportional to the diameter of s-SWNTs, and the $S1$ type SWNTs give larger γ values than the $S2$ type SWNTs as shown in Fig. 4.6. The γ value of s-SWNTs near the armchair tubes ($\theta \sim 30°$) gives relatively similar γ values between the $S1$ and $S2$ type SWNTs, while that of s-SWNTs near the zigzag tubes ($\theta \sim 0°$) gives a relatively large difference of the γ values between the $S1$ and $S2$ type SWNTs. In the small diameter range (< 0.9 nm), some s-SWNTs of the $S1$

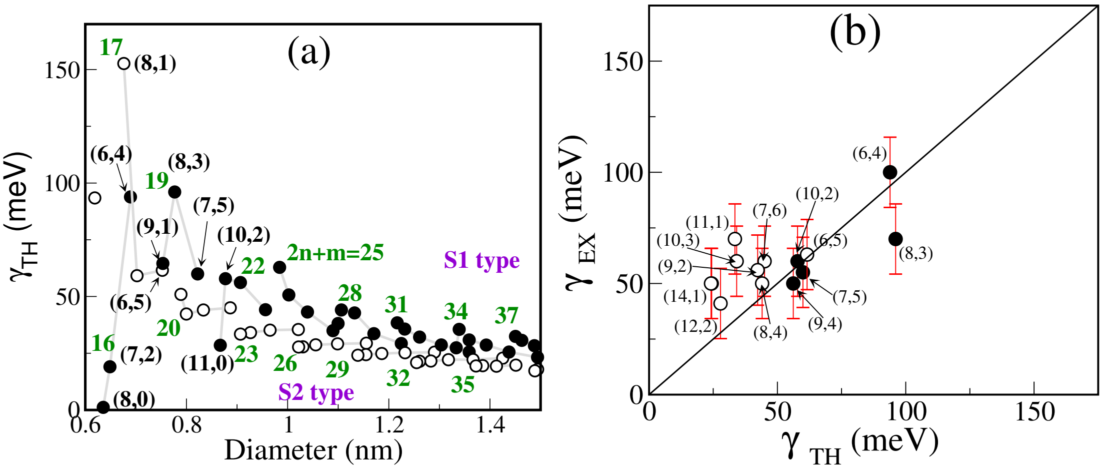

Figure 4.14: (a) The calculated total resonance windows γ_{TH} for s-SWNTs as a function of SWNT diameter in the range $0.6 < d_t < 1.5$ nm. Filled and open circles indicate the $S1$ type and $S2$ type SWNTs, respectively. The γ_{TH} value for an (8,0) SWNT is close to 0 meV, because of the absence of LO phonon scattering. The (8,1) SWNT has the largest γ_{TH} of all (n, m) s-SWNTs (153 meV). Green color numbers represent $2n + m$ =constant families. (b) Comparison of the calculated γ_{TH} with the experimental γ_{EX}. Experimental γ_{EX} values were measured by plotting the RBM intensity for HiPCO-SWNTs in SDS solution at 300 K by changing the laser energy, as explained Chapter 1. Filled and open circles indicate the $S1$ type and $S2$ type SWNTs, respectively. The experimental fitting for getting a resonance window is performed by making the integral in Raman intensity formula, accurately (to ± 15 meV).

type near the zigzag tube ($\theta \sim 0°$), such as (8,0), (7,2), (9,1), and (11,0) SWNTs, have small γ values compared with those for the $S2$ type SWNTs. In the case of (9,1) SWNT, however, because of the electron-phonon scattering with the iTA (7 meV) and RBM (7 meV) phonon modes at the K point and with the RBM (6 meV) and oTO (43 meV) phonon modes at the Γ point, the γ value becomes relatively large (65 meV). These s-SWNTs have small $\Delta E_{c_2-c_1}$ values less than 0.16 eV which is the lower limit for scattering with the LO (iTO) phonon mode as explained in Section 4.1. The (8,1) SWNT which is $S2$ type has a large γ value contrary to other $S2$ type, because the conduction bands c_2, c_3 and c_4 appear in the small energy region, and thus, we can easily find a scattering process to the many energy sub-bands. In Fig. 4.14 (b), the calculated resonance window

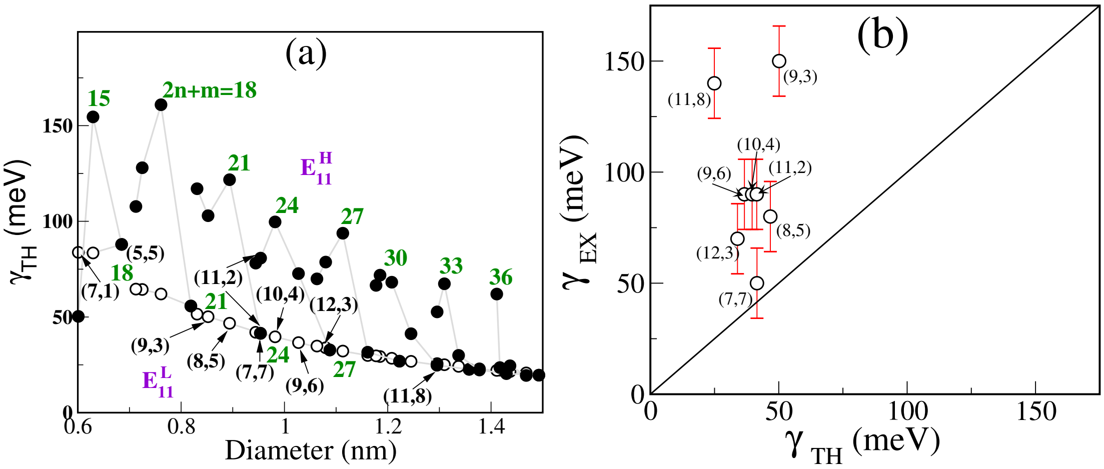

Figure 4.15: (a) Calculated γ values for m-SWNTs as a function of diameter in the range, 0.6< d_t <1.5 nm. Filled and open circles indicate the E_{11}^{H} and E_{11}^{L} optical transitions, respectively. (b) Comparison of $\gamma_{\rm TH}$ with experimental $\gamma_{\rm EX}$ values for m-SWNTs. The calculated $\gamma_{\rm TH}$ values are compared with the experimental $\gamma_{\rm EX}$ values for only E_{11}^{L} transition. The experimental fitting for getting a resonance window is performed by making the integral in Raman intensity formula, accurately (to ± 15 meV).

$\gamma_{\rm TH}$ values are compared with the experimental resonance window $\gamma_{\rm EX}$ obtained from the RBM Raman excitation profile (REP) for the HiPCO sample, as explained Chapter 1. When we compare the calculated $\gamma_{\rm TH}$ value with $\gamma_{\rm EX}$, the agreement is satisfactory. For (6,4), (6,5), and (7,5) SWNTs, the calculated $\gamma_{\rm TH}$ and experimental $\gamma_{\rm EX}$ values ($\gamma_{\rm TH}$, $\gamma_{\rm EX}$) correspond to (94, 100 meV), (62, 63 meV), and (60, 55 meV), respectively. Compared with $S1$ SWNTs, all of experimental $\gamma_{\rm EX}$ for $S2$ type SWNTs are larger than calculated $\gamma_{\rm TH}$, suggesting that there are additional relaxation paths.

Next, we show a plot for the γ values of m-SWNTs in Fig. 4.15 (a). Two types of transition appear in Fig. 4.15 (a) because of the DOS splitting due to the trigonal warping effect [92]. One is an optical transition E_{11}^{H} (solid circles) between the $c_{1\rm H}$ and $v_{1\rm H}$ bands, and the other is an E_{11}^{L} transition between the $c_{1\rm L}$ and $v_{1\rm L}$ bands (open circles). The γ value for E_{11}^{L} shows a diameter dependence and no significant chirality dependence, because the DOS of the final state in the two linear energy bands is constant (no chiral angle dependence) in the case of phonon emission. In detail, even though the γ value for LA scattering depends on the chirality and diameter, the KM and $K\Gamma$ direction scatterings inversely depend on the chirality and diameter for the inter-valley scattering, in which the zigzag tube for both direction scatterings has a similar value and the armchair tube has a quite different value. The scattering in the $K\Gamma$ direction for oTO phonon and the scattering in the KM direction for LO phonon show the chirality and diameter dependences.

However, the γ value for E_{11}^{H} shows both chirality and diameter dependences. The chirality dependence comes from the additional scattering processes to the $c_{1\mathrm{L}}$ band as a final state compared with that for E_{11}^{L}. Nevertheless, when we calculate the REP by considering the electron-phonon matrix elements, the higher energy REP peak is generally smaller in intensity than the lower energy REP peak because of the large value of the electron-phonon matrix element. Namely, since the Raman intensity is inversely proportional to the resonance window γ, the higher energy REP peak with larger γ value becomes smaller. Thus, even though the energy separation between E_{11}^{H} and E_{11}^{L} is sufficiently small compared with the γ value, the overall γ values are not significantly affected by the E_{11}^{H} peak. When we compare the above calculation results with the experiments, the theoretical γ_{TH} values are always smaller than the experimental γ_{EX}, as shown in Fig. 4.15(b). In the case of the (11,8) nanotube, for example, γ_{TH} and γ_{EX} are 25 and 140 meV, respectively. This implies that for the case of this m-SWNT, the additional processes might also be important as well as the electron-phonon interaction.

One possibility for explaining the additional contribution to the relaxation process in m-SWNTs is identified with the interaction between an excited electron and the conduction electrons in two linear energy bands, so-called plasmon. However, since the work is not the original work for this thesis, we will not explain here (see the reference [61]).

4.3 Summary

In this Chapter, we have shown the calculated results of the resonance window of Raman spectra in SWNTs, and we have compared the results of the calculated γ values with experiment. We calculated the γ value as the lifetime of a photo-excited electron, starting from identifying the resonance width with the energy dissipation, i.e. the lifetime of the carriers. For the result, in the case of s-SWNTs, we could get the calculated γ values which are in a good correlation with experiment, by considering the electron-phonon coupling model. We could see that the γ value shows a strong dependence on the chirality and diameter for s-SWNTs. However, the γ value calculation for m-SWNTs needs the additional contribution, such as might come from the electron-plasmon interaction, because the calculated γ value that considers only the electron-phonon interaction is not consistent with experimental results, i.e, we got a considerably underestimated γ value compared with experiment.

The interaction between the excited electron in the conduction band and the plasmon on two linear energy bands gives almost the same order of magnitude for γ as the γ_{EX} value despite using very rough numerical estimations. In order to apply a detailed electron-plasmon effect to the γ value calculation, we need to do more in deep research, in the future.

Chapter 5

G' band Raman spectra of SWNT

The G' band of SWNTs is a double resonance Raman spectrum with a two-phonon scattering process [7, 52]. The G' band which is free from the defect structures, usually has a higher intensity than the D band which consists of an inelastic phonon and a defect-induced elastic scattering processes [7, 53–57]. In this Chapter, the G' band Raman intensity is calculated as a function of the excitation laser energy, $E_{\rm L}$, using the electron-photon $M_{\rm el-op}$ and electron-phonon $M_{\rm el-ph}$ matrix elements for each (n, m) SWNT, as explained in Chapter 3. Also, for more precise Raman intensity calculation, we will use the Raman resonance window γ of each (n, m) SWNT obtained in Chapter 4.

Recently, there was a report on the exciton effect for the Raman intensity [93]. However, in this study, we do not use the exciton-phonon and exciton-photon interactions, but use the electron-phonon and electron-photon interactions for simplicity. This is because the exciton-phonon interaction gives a similar value to the electron-phonon interaction, and the exciton-photon interaction does not change the relative intensity even though the exciton-photon interaction enhances the optical transition significantly ($\sim$ 100 times). In conclusion of this Chapter, it will be shown that the present G' band intensity calculation can explain the metallicity dependence compared with the experiment.

5.1 Origin of G' band

In double resonance Raman scattering processes, the G' band in the Raman spectra of SWNTs can be defined by (1) a second-order, (2) two-phonon, and (3) inter-valley scattering processes, resulting in a resonant enhancement of the Raman intensity by two

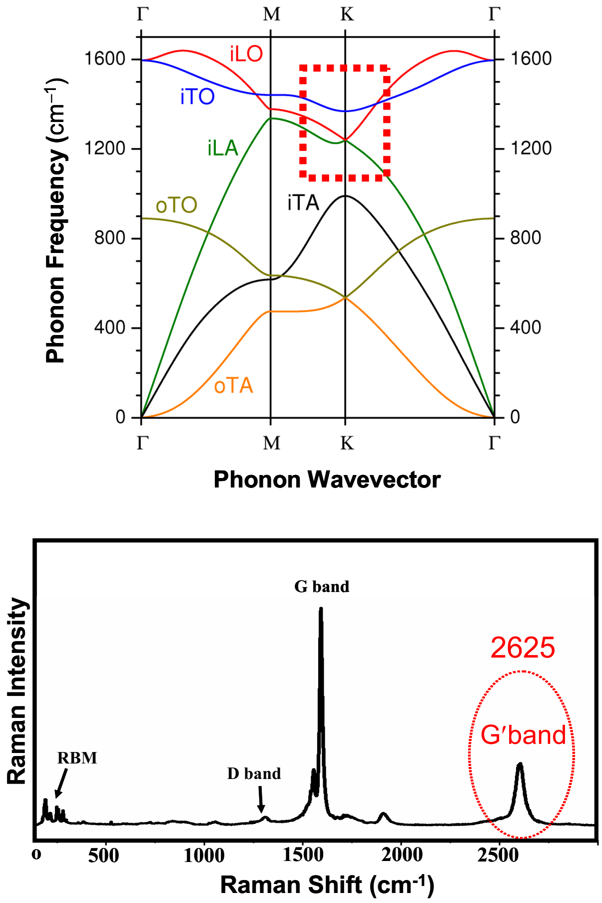

Figure 5.1: Theoretical phonon dispersion relations in graphene (top) and the experimental Raman spectra of SWNTs [23] (bottom). Red elliptical box (bottom) shows the G' band in the Raman spectra and then the two phonon modes combination in the red rectangular box (top) matches to the G' frequency.

consecutive scattering processes. As shown in Fig. 3.1, if the first scattered phonon energy $E^b(\mathbf{k}+\mathbf{q})$ and either the initial excited state energy $E^a(\mathbf{k})$ or the second scattered energy $E^b(\mathbf{k})$ correspond to real electronic states on the energy band, the Raman intensity is enhanced twice by two resonance condition factor in the denominator in the Raman intensity formula of Eq. (3.4.2). This is known as double resonance Raman scattering process. Inter-valley double resonance scattering process involves electrons with the wave vector $\mathbf{k}$ in the vicinity of the K point of 2D Brillouin zone, and thus, the G' band comes from two phonons with wave vector $\mathbf{q} \sim 2\mathbf{k}$. As shown in Fig. 5.1, the experimental G' band frequency is 2625 cm^{-1}, and the corresponding two-phonon combination around the

K point in phonon dispersion relations is related to LA, LO, and iTO phonon modes, as candidate of the origin of the G' band of SWNTs. However, the dispersive behavior of the LA phonon mode is negative along the $K\Gamma$ direction, while the G' band has a positive dispersive behavior with increasing $E_{\rm L}$ along the same direction. Near the G' band, there is a small Raman peak which appears at around 2450 cm^{-1}, and its dispersive behavior is small and negative. This peak is known as combination of iTO and LA phonon modes at the K point [94]. This band is distinguished from the iTOLA band at the Γ point as explained in Section 1.3. In order to avoid confusion, we call the combination mode of iTO and LA at the K point to G^* band in this thesis. Since the G^* band is much weaker than the G' band in the experimental Raman spectra, the observation of the G^* band is required a good quality of sample and long exposure time. Thus, the LA phonon mode at the K point contributes to the G^* band. In comparison, the LO and iTO phonon modes show a positive dispersive behavior along $K\Gamma$ direction and are good candidates as the origin of the G' band.

5.2 Important factors of G' band

As explained in Section 3.4, the G' band involves four scattering processes which consist of optical absorption and emission, and two electron-phonon scatterings by the phonon emission (or absorption). First, the electron-photon matrix elements in SWNTs are obtained by substituting the 1D angular and linear momentum μ, k in Eq. (2.1.17) instead of the 2D momentum $\mathbf{k}$ into Eqs. (3.1.4), (3.1.5) and (3.1.6). The curvature effect of SWNT is given by aligning the atomic orbitals in Eq. (3.1.6) along the tangential and normal directions. The electron-photon matrix elements depend on light propagation direction and polarization vector with respect on the SWNT axis. When the light propagates perpendicular to tube axis and is linearly polarized parallel to the tube axis, the electron-photon matrix element nearly reaches its maximum at the E_{ii} transition in the joint density of states (JDOS) [36,67,95,96]. However, for the perpendicular polarization to tube axis, the electron-photon matrix element has a value for the $E_{i,i\pm1}$ transition in the JDOS [36, 67, 95, 96]. In the present G' band calculation, we consider only for the parallel polarization to tube axis, which corresponds to light propagating perpendicular to tube axis.

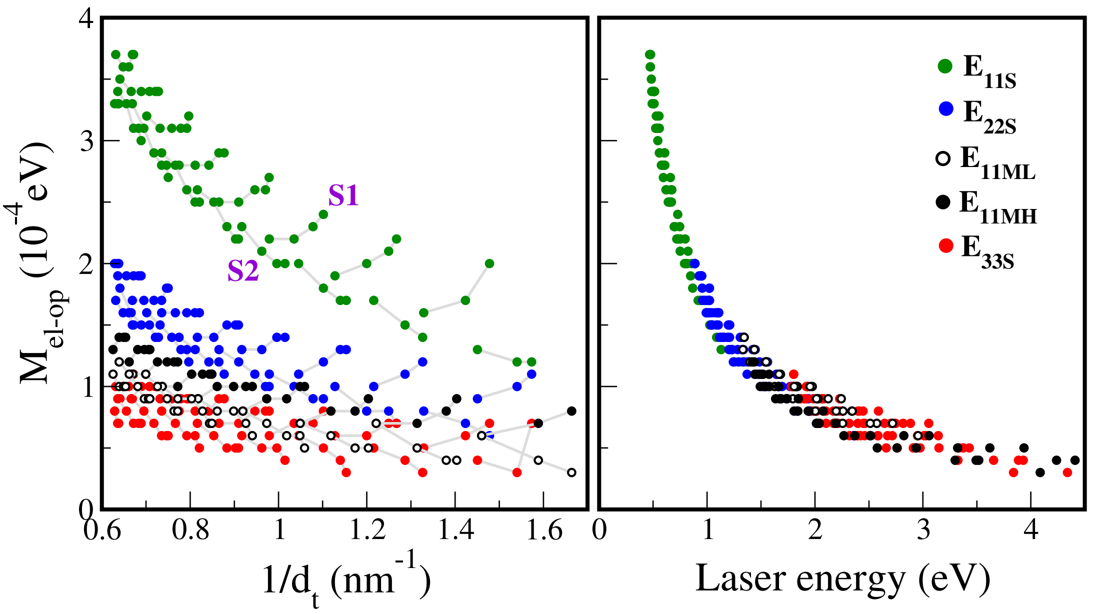

Figure 5.2: Electron-photon matrix elements for each transition, E^S_{11}, E^S_{22}, E^{ML}_{11}, E^{MH}_{11}, and E^S_{33}, as functions of inverse diameter and excitation laser energy.

Figure 5.2 shows the electron-photon matrix elements for each transition, E^S_{11}, E^S_{22}, E^{ML}_{11}, E^{MH}_{11}, and E^S_{33}, as functions of inverse diameter and excitation laser energy. The matrix elements strongly depend on the excitation laser energy E_{L} as seen in Eq. (3.1.4). The E_{L} dependence of electron-photon matrix elements affects the G' band Raman intensity, that is, the G' band intensity decreases with increasing the excitation laser energy, which will further be explained in detail in next Section. Also, the matrix elements $M_{\text{el-op}}$ for E^S_{11} and E^S_{22} transitions show strong diameter and chiral angle dependences, but for E^M_{11} and E^S_{33} transitions, only chiral angle dependence is significantly seen. The strong dependence of $M_{\text{el-op}}$ on the chiral angle for each transition comes from the trigonal warping effect of the electronic structure [92], and the optical matrix elements increase from K to M point in the high symmetry line KM, but decrease from K to Γ point in the line $K\Gamma$ [36]. Therefore, the matrix elements of $S1$ type SWNT at the E^S_{11} transition are larger than those of the $S2$ type. For E^S_{22} transition, the matrix elements of the $S2$ type are larger than those of the $S1$ type. Large family spread of the electron-photon matrix elements appears at the higher transition energy due to the larger JDOS. The matrix elements for each transition can be enumerated in the following order, as shown in Fig.

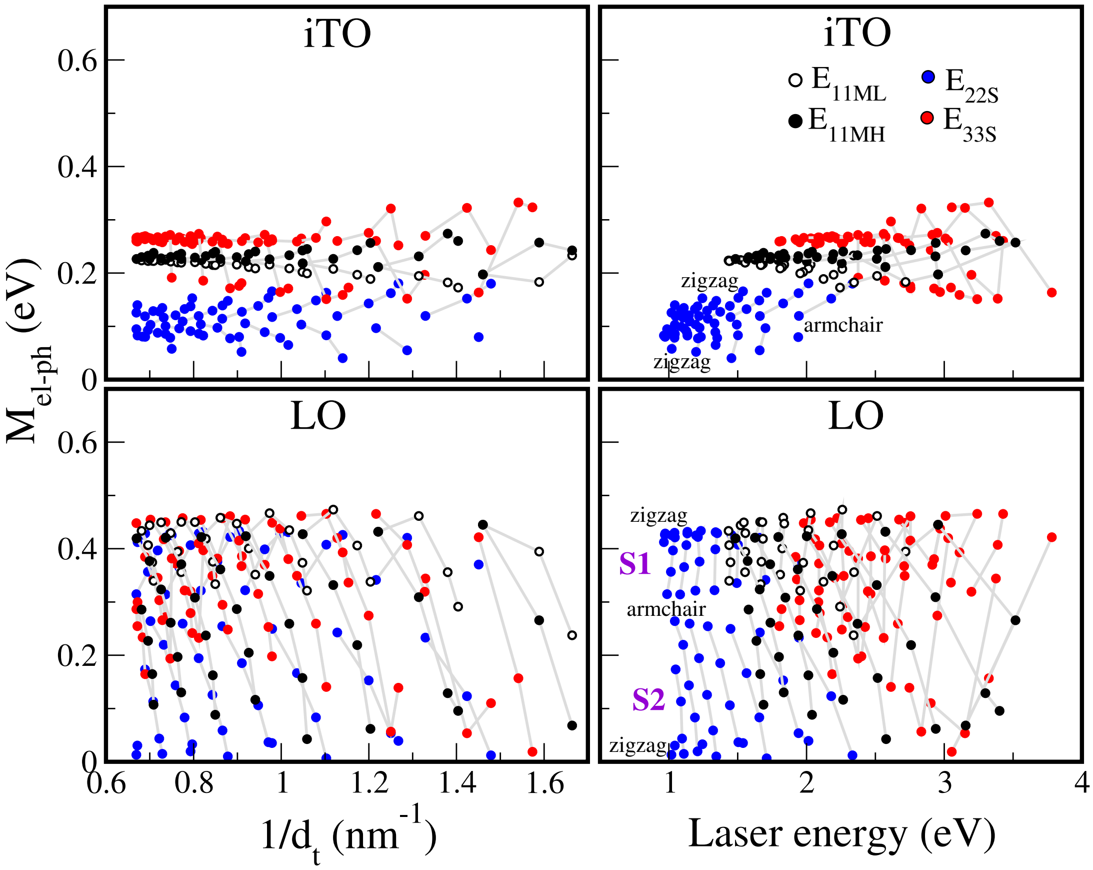

Figure 5.3: Electron-phonon matrix elements of the scattering along the KM direction for the iTO (top) and LO (bottom) phonon modes as functions of inverse diameter (left) and excitation laser energy (right). Blue, white, black, and red circles represent E_{22}^{S}, E_{11}^{ML}, E_{11}^{MH}, and E_{33}^{S} transitions, respectively.

5.2:

$$E_{11}^{S} > E_{22}^{S} > E_{11}^{M} > E_{33}^{S}. \tag{5.2.1}$$

Next, we consider the electron-phonon matrix element for which a photo-excited electron in the conduction band scatters to another K point by emitting a phonon with wave vector $\mathbf{q}$ and energy $\hbar\omega(\mathbf{q})$. For a given initial electron state $\mathbf{k}$ in SWNT, there are four possible electron-phonon scattering paths, i.e. intra- and inter-valley, forward and backward scatterings for $6N$ different phonon modes, since the phonon wave vector in the circumferential direction is discrete. For the G' band intensity calculation, we select the inter-valley, forward, and backward scatterings for LO and iTO phonon modes. Since we select only a photo-excited electron in the bottom of the conduction band as an initial state **k**, the initial band velocity is zero, and thus we replace the forward and backward scatterings with the scatterings along the high symmetry direction KM and $K\Gamma$ lines, respectively, as explained in Chapter 4.

Figure 5.3 shows the electron-phonon matrix elements of the scattering along the KM direction for the iTO and LO phonon modes for E_{22}^S, E_{11}^{ML}, E_{11}^{MH}, and E_{33}^S optical transitions, as functions of inverse diameter and excitation laser energy. While the iTO electron-phonon matrix elements give a small family spread, the LO electron-phonon matrix elements give a large family spread, as shown in Fig. 5.3. For E_{22}^S transition, the LO electron-phonon matrix elements of $S2$ type SWNTs give almost zero value near the zigzag direction ($\theta \sim 0°$), but those of $S1$ type SWNTs have the largest value ($\sim$0.4 eV) near the zigzag direction. In the case of iTO electron-phonon matrix elements for E_{22}^S transition, the SWNTs near the armchair direction ($\theta \sim 30°$) have similar values to one another regardless of $S1$ and $S2$ types, and the difference of the matrix element between the $S1$ and $S2$ types is smaller than that for the LO phonon mode. As the result, the iTO electron-phonon matrix elements give a clear dependence of the transition energy, i.e. E_{22}^S, E_{11}^{ML}, E_{11}^{MH}, and E_{33}^S, similar to the case of the optical matrix element, but the LO electron-phonon matrix elements do not give any transition energy dependence except for the strong chiral angle dependence. Since the LO electron-phonon matrix elements give larger values for some zigzag (n, m) SWNTs than those for the iTO phonon mode, the LO+LO combination for the zigzag SWNT generally gives larger intensity (see Fig. 5.7). The calculated G' band intensity will be shown in next Section.

The electron-phonon matrix elements around the K point are sensitive to the electron wave vector **k**. As shown in Fig. 4.2, the energy dispersion shows asymmetry near the K point, and its asymmetry is relevant to quite different electron-phonon matrix elements for the high symmetry lines KM and $K\Gamma$, respectively. Figure 5.4 shows the electron-phonon matrix elements of the scattering along the $K\Gamma$ direction for the iTO and LO phonon modes for each transition, E_{22}^S, E_{11}^{ML}, E_{11}^{MH}, and E_{33}^S, as functions of inverse diameter and excitation laser energy. Comparison to the scattering in the KM direction in Fig. 5.3, the LO electron-phonon matrix elements for E_{11}^{ML}, E_{11}^{MH}, and E_{33}^S transitions give small values, while the matrix elements for E_{22}^S transition have a similar family spread and similar values to one another. The iTO electron-phonon matrix elements, similar to the scattering in the KM direction, give a dependence on the transition energy except for

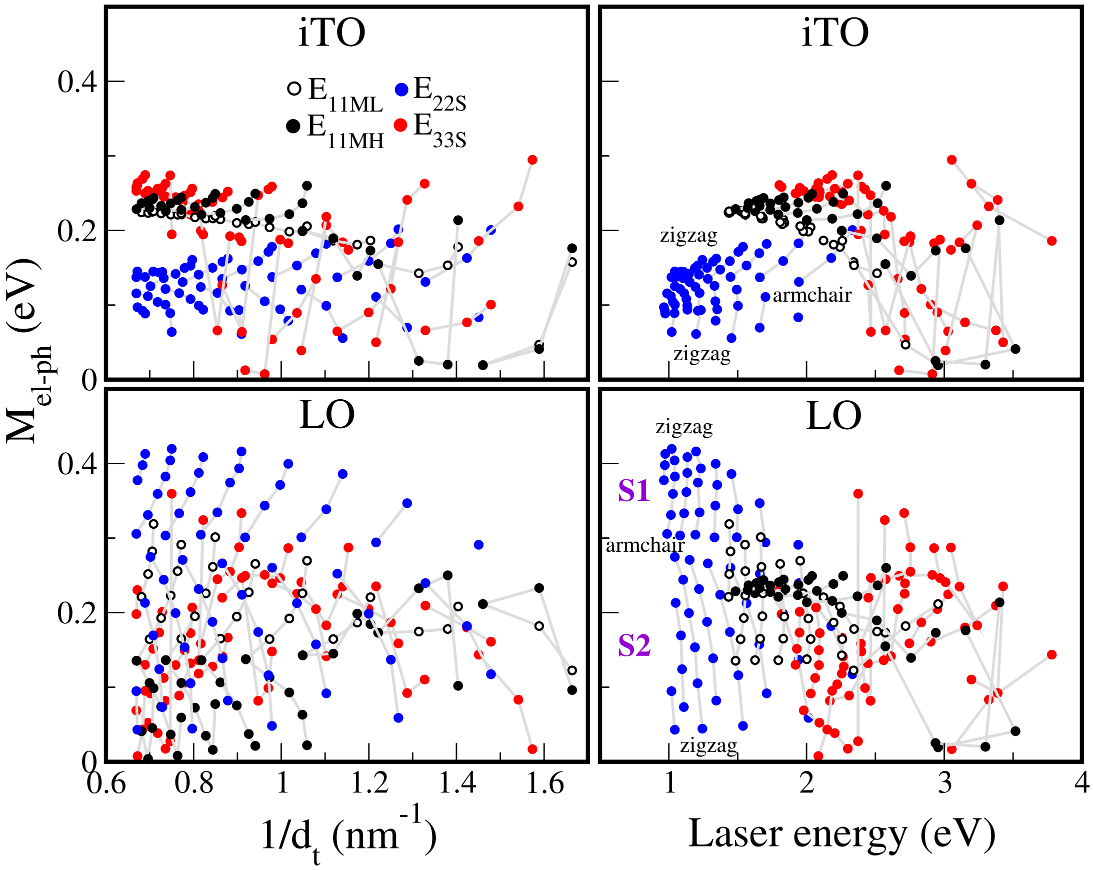

Figure 5.4: Electron-phonon matrix elements of the scattering along the $K\Gamma$ direction for the iTO (top) and LO (bottom) phonon modes in each transition, E_{22}^{S}, E_{11}^{ML}, E_{11}^{MH}, and E_{33}^{S}, as functions of inverse diameter (left) and excitation laser energy (right).

small diameter SWNTs. Some of iTO electron-phonon matrix elements for E_{33}^{S} transition have almost similar values to those for the E_{22}^{S} transition in the small diameter range SWNTs. As the result, we can enumerate the iTO electron-phonon matrix elements of the scattering along the $K\Gamma$ direction for each transition in the following order:

$$E_{22}^{S} < E_{11}^{M} < E_{33}^{S}. \tag{5.2.2}$$

In the case of inter-valley scattering at the E_{33}^{S} transition, a photo-excited electron in c_3 band can scatter to c_2 band or to c_1 band by emitting a phonon, satisfying energy-momentum conservation. Figure 5.5 shows the comparison of electron-phonon matrix elements by scattering from c_3 to c_2 band and by scattering from c_3 to c_1 band at the E_{33}^{S} transition. Figures 5.3 and 5.4 show the electron-phonon matrix elements only for the

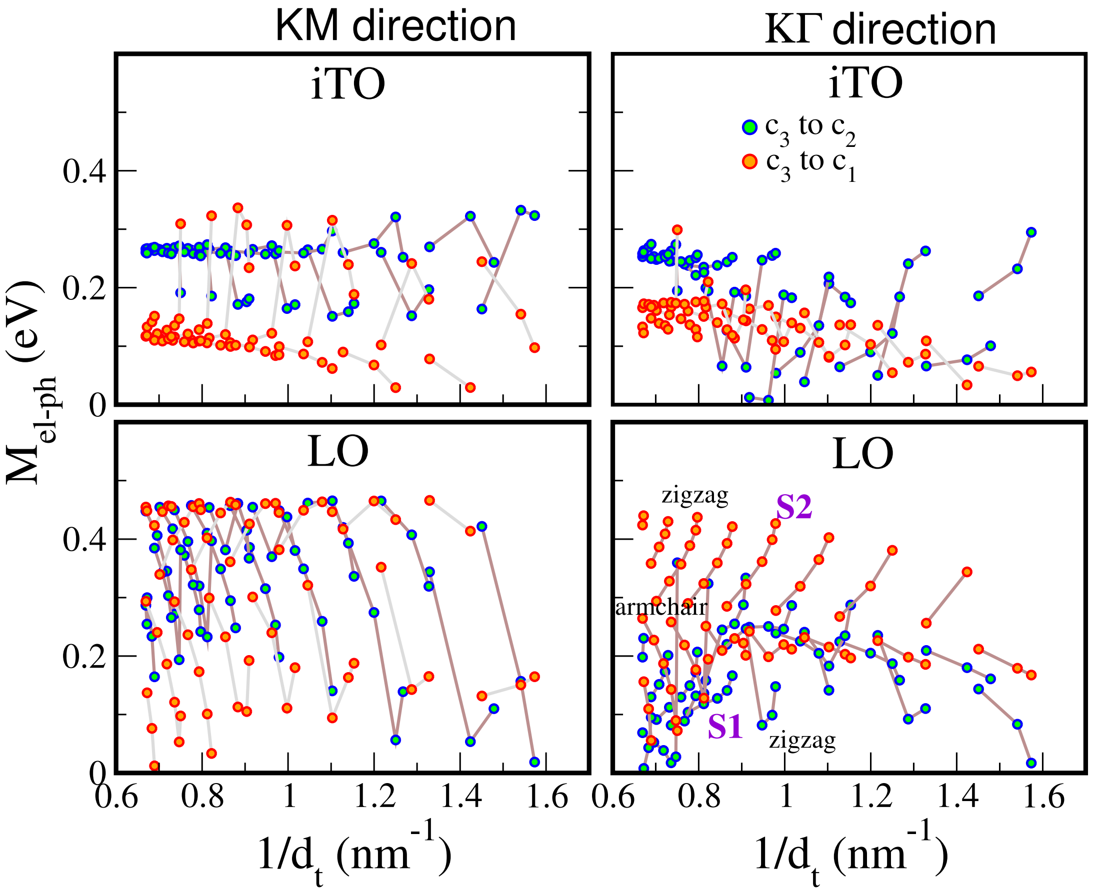

Figure 5.5: Comparison of electron-phonon matrix elements of iTO (top) and LO (bottom) phonon modes for the scattering in the KM (left) and $K\Gamma$ (right) direction for E_{33}^S transition. Green and orange filled circles represent the inter-valley electron-phonon scattering from c_3 to c_2 band and from c_3 to c_1 band, respectively.

scattering from c_3 to c_2 band at the E_{33}^S transition. As shown in Fig. 4.2, the scattered phonon wave vectors from c_3 to c_2 band and from c_3 to c_1 in the $K\Gamma$ direction scattering have a small difference compared with the case of the KM direction scattering because of asymmetry of the energy band around the K point of the Brillouin zone. For the LO phonon scattering along the $K\Gamma$ direction, the scattering from c_3 to c_1 band gives a larger matrix element than the scattering from c_3 to c_2 band, in which the scattering from c_3 to c_1 band for the $S2$ type SWNT is stronger than the scattering from c_3 to c_2 band. Along the KM direction, the LO electron-phonon matrix elements from c_3 to c_2 band have similar values to those from c_3 to c_1 band. We might suggest that the electron-phonon

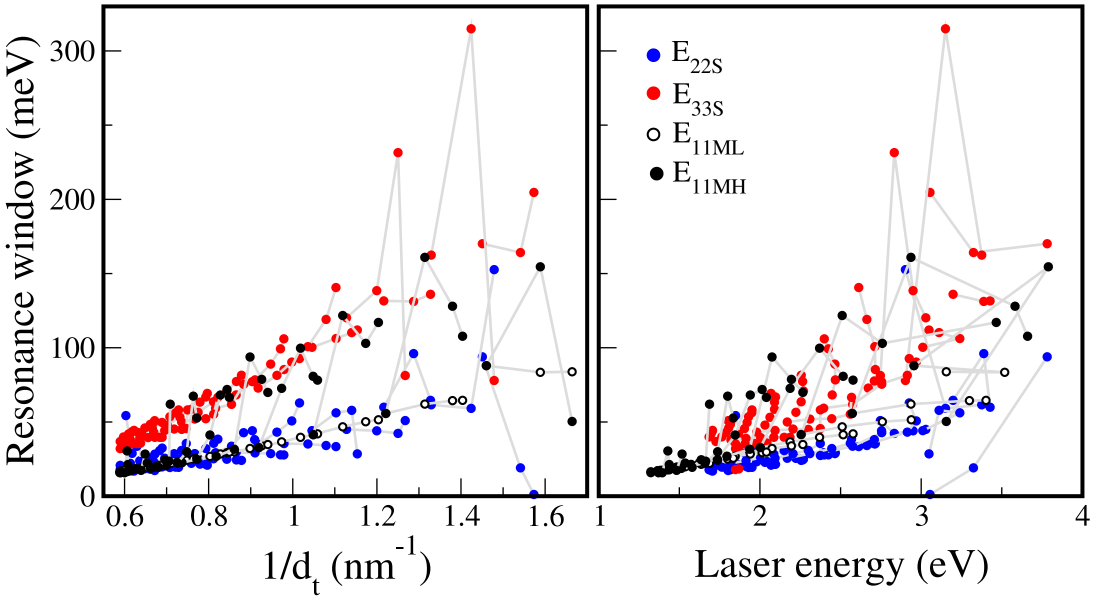

Figure 5.6: Raman resonance windows for the G' band in each transition, E_{22}^{S}, E_{11}^{ML}, E_{11}^{MH}, and E_{33}^{S}, as functions of inverse diameter (left) and excitation laser energy (right). Blue, white, black, and red circles represent E_{22}^{S}, E_{11}^{ML}, E_{11}^{MH}, and E_{33}^{S} transitions, respectively.

KM direction scattering for the LO phonon mode depends on the chiral angle, and the $K\Gamma$ direction scattering depends on the $S1$ and $S2$ types. However, for the iTO phonon mode, the scattering matrix elements in both KM and $K\Gamma$ direction give larger values for the scattering from c_3 to c_2 band than for the scattering from c_3 to c_1 band.

Finally, we consider the Raman resonance window as an important factor of the G' band intensity. The resonance window of Raman spectra is given by the life time of the inelastic electron-phonon scattering for a given photo-excited state in the conduction band. In Chapters 3 and 4, we already explained the calculation method and the result by comparing with the experiment. Since the G' band peak intensity is proportional to the resonance window to minus forth power, γ^{-4}, in Eqs. (3.4.1) and (3.4.2) due to the double resonance Raman scattering, the G' band peak intensity quickly increases with decreasing the resonance window. As explained in Eqs. (3.3.3) and (3.3.5), the resonance window is proportional to square of the electron-phonon matrix elements. Therefore, we suggest that finally the G' band peak intensity is inversely proportional to the electron-phonon matrix elements, $|M_{\rm el-ph}|^{-4}$, where we use the fact that $M_{\rm el-ph}$ matrix elements appear in the numerator of Eq. (3.4.2). Namely, small electron-phonon matrix elements for six phonons give large Raman peak intensity. Thus, the iTO phonon is remarkable in the G' band intensity due to slightly small electron-phonon matrix elements compared with the LO phonon matrix elements.

In this Chapter, however, we calculate the G' band intensity based on Eqs. (3.4.1) and (3.4.2), and use the total resonance window for each electron-phonon scattering path as given in Figs. 4.14 and 4.15. The G' band Raman intensity is obtained by substituting the (n, m) resonance windows into Eq. (3.4.2). Figure 5.6 shows the total Raman resonance windows considering all possible scattering paths for each transition, E_{22}^S, E_{11}^{ML}, E_{11}^{MH}, and E_{33}^S, as functions of inverse diameter and excitation laser energy. As shown in Fig. 5.6, the resonance windows strongly depend on diameter and transition energy. Since, in the electron-phonon scattering in the higher E_{ii} energy, there are many possible scattering paths, E_{33}^S transition has the largest resonance window of these transitions. In the case of E_{11}^M transition, while the resonance windows for E_{11}^{ML} only depend on diameter, the case for E_{11}^{MH} depends on diameter and chiral angle. In particular, for less than 1.75 eV laser energy, the E_{11}^M resonance windows are the smallest of the three transitions, E_{22}^S, E_{11}^M, and E_{33}^S. This result gives the large G' band peak intensity compared with other transitions and we will explain it in the next Section.

5.3 G' band Raman intensity

The G' band intensity is calculated for each E_{ii} value of (n,m) SWNTs whose intensity is normalized by per unit length of a SWNT. Three variables were already calculated to obtain the G' band intensity in previous Section: the electron-phonon matrix element, electron-photon matrix element, and Raman resonance window. Using the phonon dispersion relation of the SWNT, we already explained that the G' band might be related to a combination of the LO and iTO phonon modes around the K point in the Brillouin zone of graphene sheet. Moreover, the electron-phonon matrix elements at the K point for the iTO phonon depend on the transition energy E_{ii}. The electron-phonon matrix element for the E_{11}^M transition for the metallic SWNTs is larger than that for the E_{22}^S transition of the semiconducting SWNTs.

In Fig. 5.7, we show the calculated G' band intensity for iTO+iTO (top) and LO+LO (bottom) phonon combinations as a two-phonon scattering process for all (n,m) SWNTs

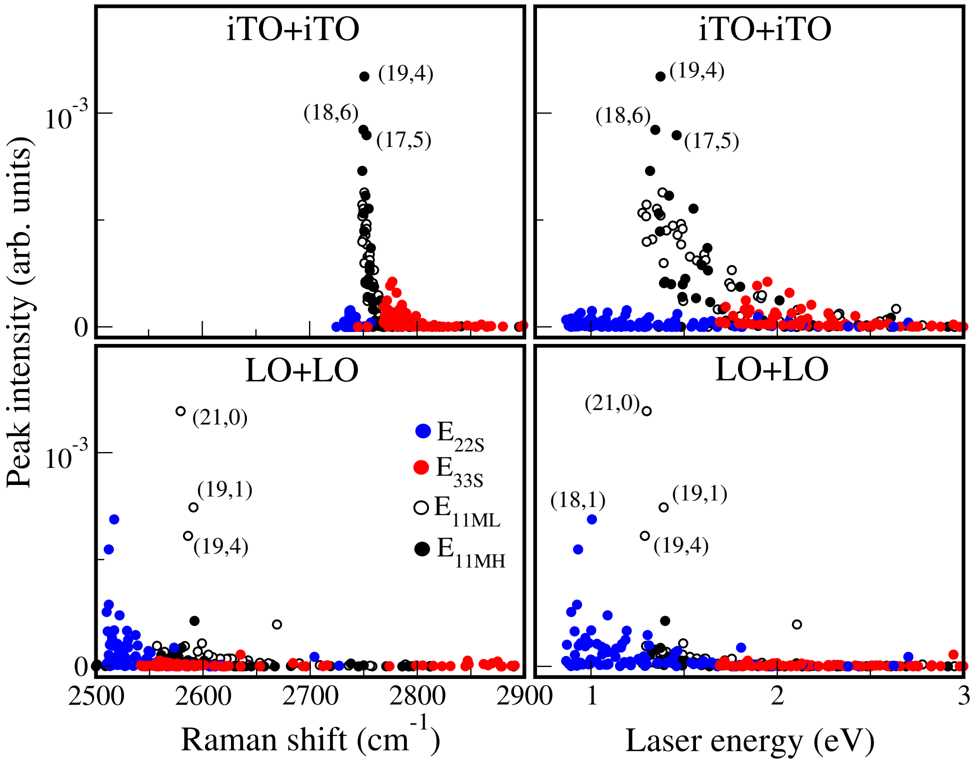

Figure 5.7: The calculated G' band Raman intensity for all (n, m) SWNTs in the diameter range $0.6 < d_t < 1.6$ nm as functions of Raman shift (left) and excitation laser energy (right) for the iTO overtone (top) and the LO overtone (bottom), respectively. White and black filled circles indicate the lower metallic transition E_{11}^{ML} and the higher metallic transition E_{11}^{HM}, respectively and blue and red filled circles indicate the semiconducting transitions E_{22}^{S} and E_{33}^{S}, respectively.

in the diameter range, $0.6 < d_t < 1.6$nm, as functions of Raman shift and excitation laser energy. The LO+LO optical phonon combinations do not provide a metallicity dependence consistent with the experiment for the G' band Raman intensity as shown in Fig. 5.7. In Fig. 1.5, we showed that the G' band intensity depends on metallicity in the HiPCO SWNTs sample which removes the metallic SWNTs from the semiconducting SWNTs in small diameter range, $d_t < 1.0$ nm, by a chemical reaction which acts on metallic SWNTs [24, 25, 97]. It should be noted that the G' band by the LO+LO phonon combination provides a stronger intensity for semiconducting SWNT than that for metallic SWNT in the excitation laser energy range, $E_{\mathrm{L}} < 1.2$ eV. For larger excitation laser energies (> 1.2 eV), a few metallic (n,m) tubes have a stronger intensity than that for

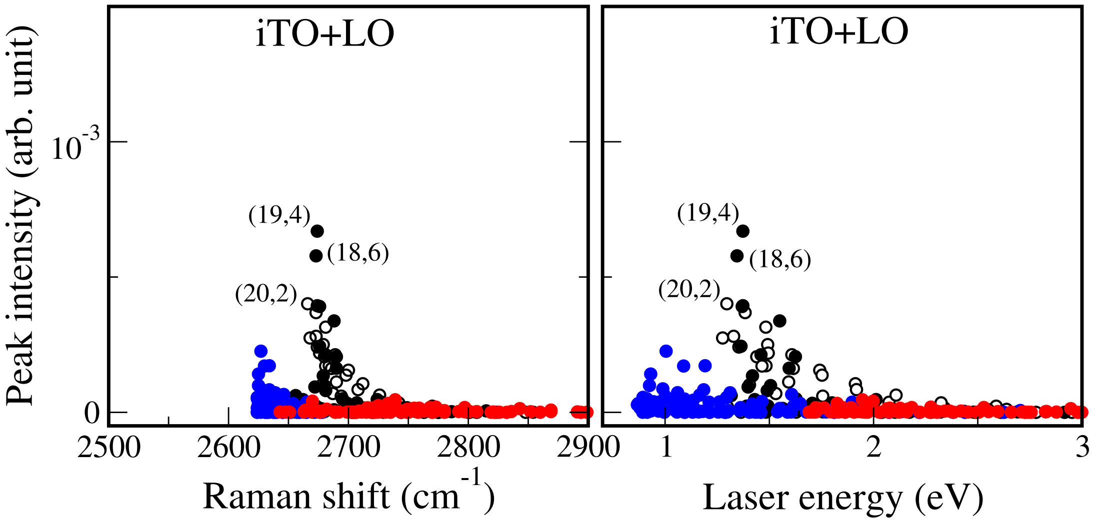

Figure 5.8: The calculated G' band Raman intensity for all (n, m) SWNTs in the diameter range $0.6 < d_t < 1.6$ nm as functions of Raman shift (left) and excitation laser energy (right) for combination of the iTO and LO phonon modes.

semiconducting SWNTs, in which a zigzag metallic tube (21,0) has a large intensity due to the chiral angle dependence of the LO electron-phonon matrix elements as explained in Fig. 5.3. However, the electron-phonon matrix elements for the LO phonon mode at the K point are independent of the metallicity as explained in the previous Section. For the combination of the iTO phonon mode, E_{11}^M provides a larger G' band intensity than E_{22}^S and E_{33}^S as shown in Fig. 5.7. For the reason for this behavior, we found that the electron-phonon matrix elements of the iTO phonon mode produce larger values for E_{11}^M than for E_{22}^S. For E_{33}^S, the electron-phonon matrix elements have a similar value to E_{11}^M. However, the γ value for E_{33}^S is larger than that for E_{11}^M, which reduces the Raman intensity for E_{33}^S as shown in Fig. 5.6. Because of the trigonal warping effect, E_{11}^M, the vHS peak is split into two peaks at lower and the higher energies, E_{11}^{LM} and E_{11}^{HM}, respectively. The G' band intensity for E_{11}^{LM} is definitely larger than that for E_{22}^S and E_{33}^S at all laser excitation energy ranges which is consistent with the experimental observation.

The Raman shift of the G' band for iTO overtone in the calculation was blue-shifted (100 cm^{-1}) compared with the experimental value. The agreement of the theoretical prediction with experiment values will be improved if the Kohn anomaly, which is more dispersive around the K point, is considered.

In Fig. 5.8, the G' band intensities for combination of the iTO and LO phonon modes for all (n, m) SWNTs in the diameter range $0.6 < d_t < 1.6$ nm have small values compared with those for the iTO+iTO phonon combination, even though the iTO+LO intensity gives the dependence of metallicity in the excitation laser energy range, $1.2 < E < 1.75$ eV. Therefore, we can say that the iTO+iTO combination for the G' band is dominant compared with the iTO+LO combination.

5.4 Summary

The G' band is defined as double resonance Raman scattering, two-phonon scattering, and inter-valley scattering. By considering these starting points, we calculated the G' band and could investigate a peculiar phenomenon in the G' band Raman intensity of SWNTs. The intensity of the G' band was strongly related to the metallicity of the SWNT sample. This metallicity dependence is explained by electron-phonon interactions (mostly iTO phonon modes) from the extended tight-binding calculations. These results demonstrate that the intensity of the G' band in Raman spectroscopy is a measure of the metallicity of carbon nanotube samples.

However, the optical and relaxation properties of SWNTs are affected by excitonic effect, and the free electron model fails to quantitatively reproduce the relative intensities of the spectral features observed in experiments, for example, tube length dependence. The exciton-photon and exciton-phonon transition matrix elements are calculated upon substituting the excitonic wave functions obtained within the ETB framework. Future calculations of the Raman spectra involving the exciton-photon and exciton-phonon transition matrix elements are expected to provide better agreement with the results of experimental observations.

Chapter 6

G' band of multi-layer graphene

In this Chapter, we present the electronic energy band structure for multi-layer graphene and calculate the Raman G' band as a function of the number of graphene layers, and compare the calculated results with the experiment. As explained in Section 3.5, the inter-layer interaction in multi-layer graphene gives the energy band splitting near the Fermi level. Since the G' band is a double resonance Raman scattering process, the split energy band structure for multi-layer graphene results in different sub-peaks in the G' band region. Therefore, in order to understand the electronic energy band structure for multi-layer graphene, we need to analyze sub-peaks of the G' band in experimental Raman spectra.

6.1 Raman scattering processes

In the case of single layer graphene, we already described in detail the double resonance Raman scattering process in section 3.5. Since the energy dispersion for π electron of single layer graphene gives only two linear bands at the K point in the Brillouin zone of a graphene sheet, we just consider one possible optical scattering process. As the result, the G' band shows a sharp peak with small spectral width.

In double layer graphene, the energy band around the K point shows two parabolic bands for up and down bands which are split from two linear band of single layer graphene due to inter-layer interaction between π electrons (see Fig. 3.4 (a)). The splitting of the energy band around the K point plays an important role to determine the G' band as explained above. For the G' band calculation of double layer graphene, we have to find

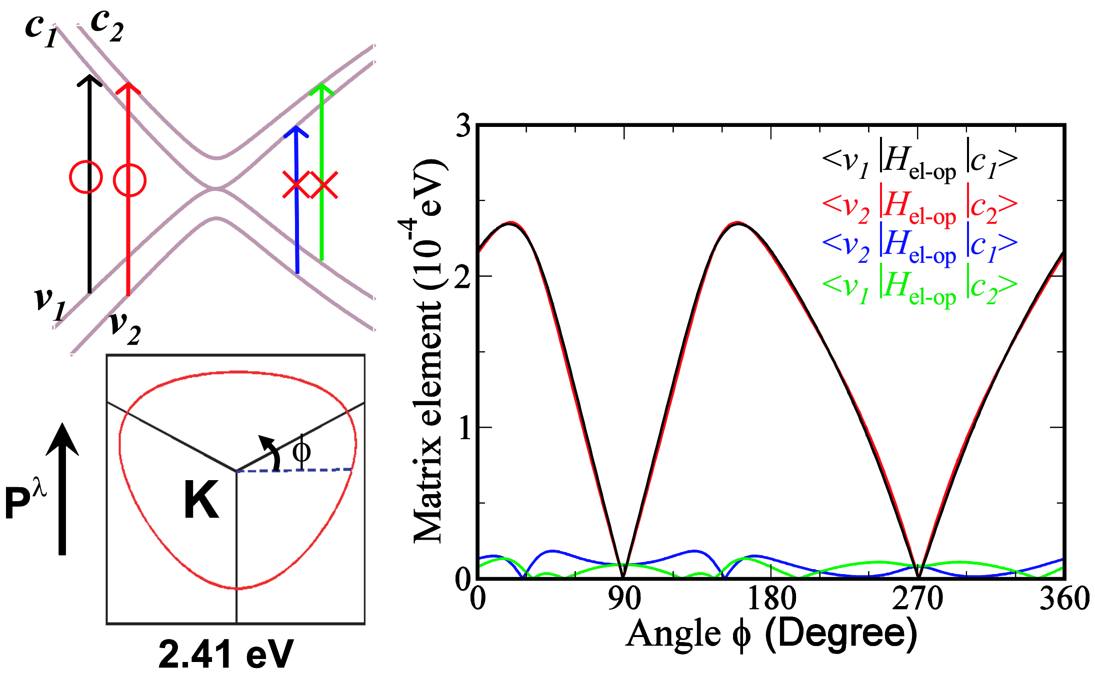

Figure 6.1: Possible optical absorption processes (left top). By the optical matrix elements calculation, the optical absorption processes from v_i to c_i $(i = 1, 2)$ are possible, where i indicates the energy sub-band index. The light polarization vector $\mathbf{P}^\lambda$ is in the zigzag direction (left bottom) and the optical matrix elements is given as a function of polar angle ϕ along the contour of $E_{\mathrm{L}} = 2.41$ eV (right). Black, red, blue, and green arrows correspond to the electron-photon matrix elements $\langle v_1|H_{\mathrm{el-op}}|c_1\rangle$, $\langle v_2|H_{\mathrm{el-op}}|c_2\rangle$, $\langle v_2|H_{\mathrm{el-op}}|c_1\rangle$, and $\langle v_1|H_{\mathrm{el-op}}|c_2\rangle$, respectively [72].

possible Raman scattering processes. First, we check possible electron-photon absorption processes, when a valence electron is excited to the conduction band of double layer graphene, as shown in Fig. 6.1. In order to calculate the electron-photon matrix element $M_{\mathrm{el-op}}$ for double layer graphene, we have to consider four optical transitions from the valence band to the conduction band. For double layer graphene, the optical matrix elements $M_{\mathrm{el-op}}(v_1 \text{ to } c_2)$ and $M_{\mathrm{el-op}}(v_2 \text{ to } c_1)$ become almost zero by theoretical calculation which can be understood by the symmetry, as shown in right plot of Fig. 6.1. The electron-photon matrix elements calculation is based on Section 3.1. In comparison, the optical matrix elements $M_{\mathrm{el-op}}(v_1 \text{ to } c_1)$ and $M_{\mathrm{el-op}}(v_2 \text{ to } c_2)$ within the same layer are similar to that for single layer graphene. Thus, we have two possible optical absorption

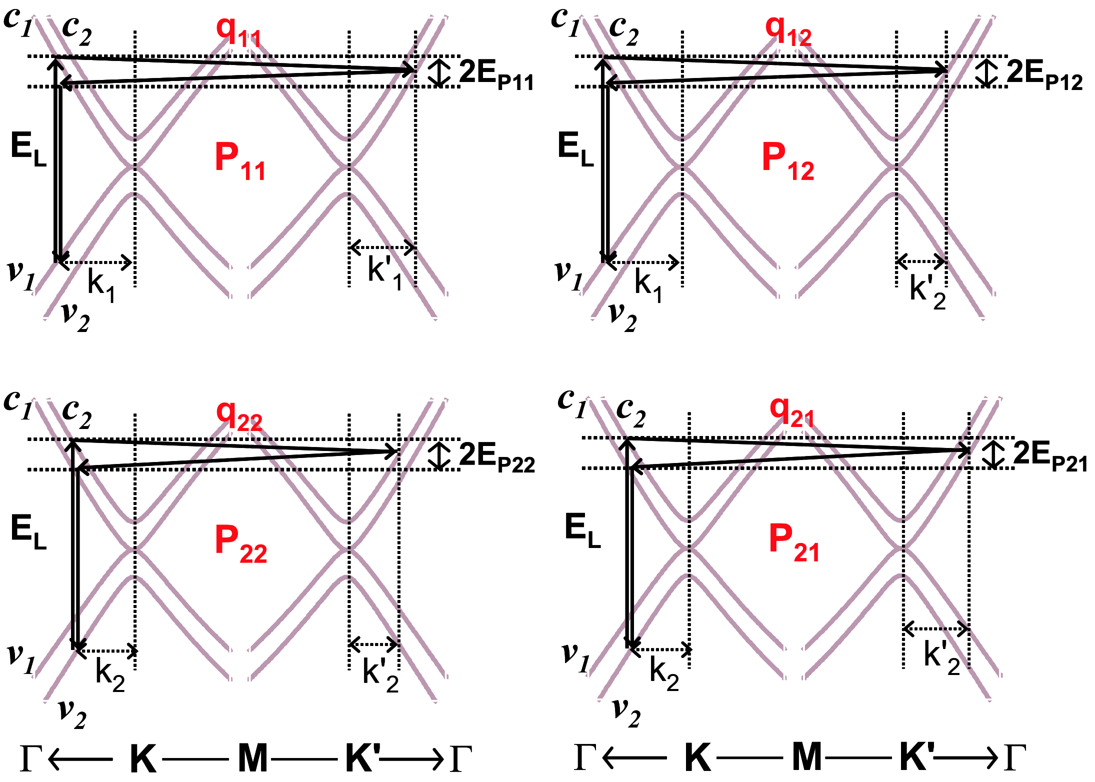

Figure 6.2: Schematic double resonance Raman scattering processes of double layer graphene. We find four possible optical processes in the energy band structure of double layer graphene.

processes and we can make two equi-energy contour around the K point as explained in Section 3.5. An electron which is excited from v_i to c_i enery band scatters to one of two parabolic bands at the K' point, emitting a phonon, where i (=1,2) indicates the energy sub-band index.

Therefore, we have four possible double resonance Raman scattering processes for the double layer graphene along the $\Gamma - K - M - K' - \Gamma$ direction, as shown in Fig. 6.2. These four possible inter-valley double resonance Raman scattering processes might lead to the observation of four sub-peaks in the double layer graphene. P_{11} process represents that an electron with wave vector $\mathbf{k}_1$ in v_1 band scatters to c_1 band, absorbing the incident laser energy E_{L}, and scatters to another electronic state $\mathbf{k}'_1$ in c'_1 band by emitting a phonon with wave vector $\mathbf{q}_{11}$, and scatters back to c_1 band, and finally recombines with a hole in v_1 band, where $\mathbf{q}_{11} = \mathbf{k}_1 - \mathbf{k}'_1$. P_{22} process involves the optical absorption process from v_2

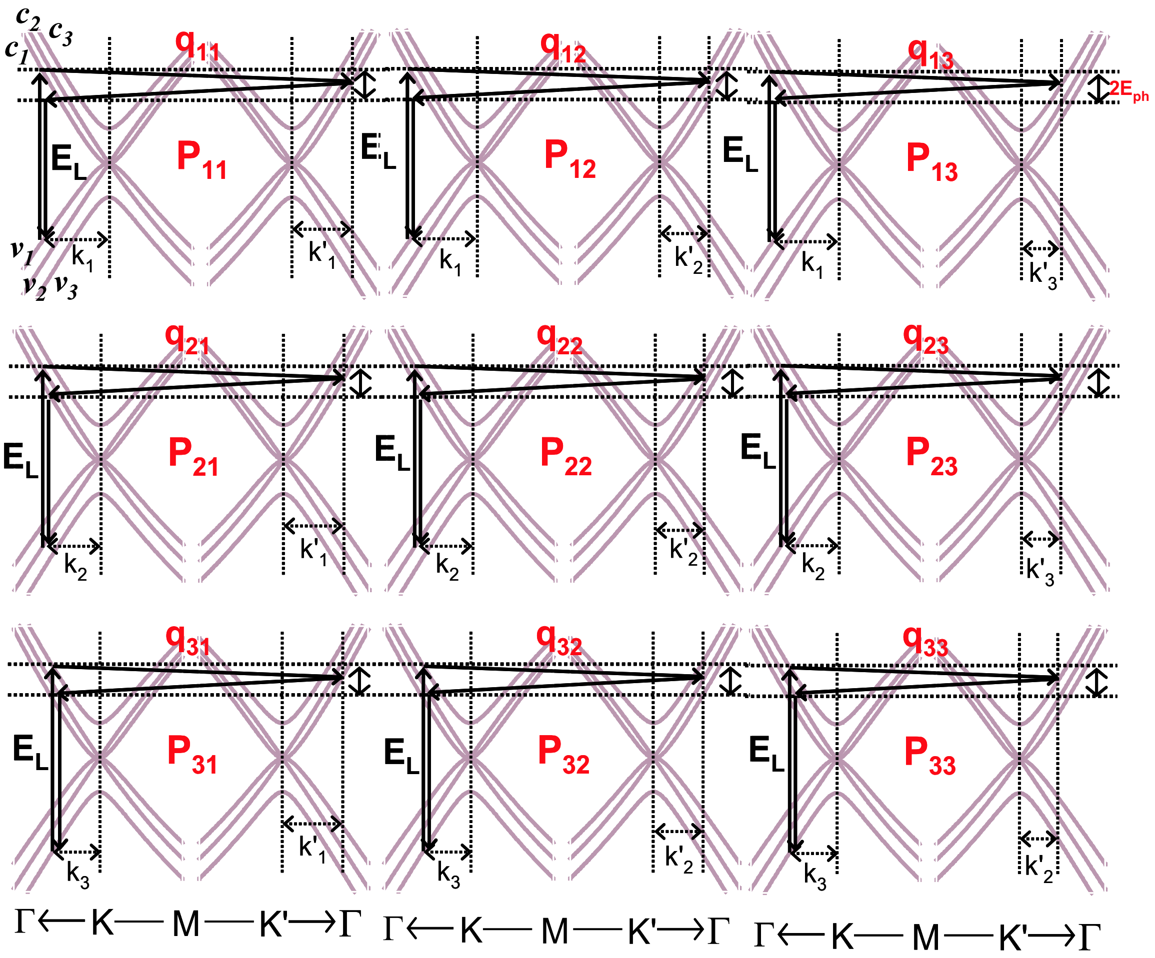

Figure 6.3: Schematic double resonance Raman scattering processes of triple layer graphene. We find nine possible optical processes in the electronic band structure of triple layer graphene.

to c_2 band with electron wave vector $\mathbf{k}_2$ and the electron-phonon scattering process from c_2 to c_2' band by emitting a phonon with wave vector $\mathbf{q}_{22} = \mathbf{k}_2 - \mathbf{k}_2'$. Similarly, P_{12} and P_{21} processes also involve the optical process of an electron with $\mathbf{k}_1$ and $\mathbf{k}_2$, respectively, and involve the electron-phonon scattering process for a phonon with wave vector $\mathbf{q}_{12}$ and $\mathbf{q}_{21}$, respectively, where $\mathbf{q}_{12} = \mathbf{k}_1 - \mathbf{k}_2'$, and $\mathbf{q}_{21} = \mathbf{k}_2 - \mathbf{k}_1'$. As explained in Chapter 5, the G' band comes from the overtone of iTO phonon mode. Since the wave vector of iTO phonon mode $\mathbf{q}_{11}$ associated with P_{11} process is the largest of these four wave vetors, as shown in Fig. 6.2, the P_{11} process corresponds to the highest frequency subpeak in the G' band of double layer graphene. On the other hand, the P_{22} process gives the lowest frequency

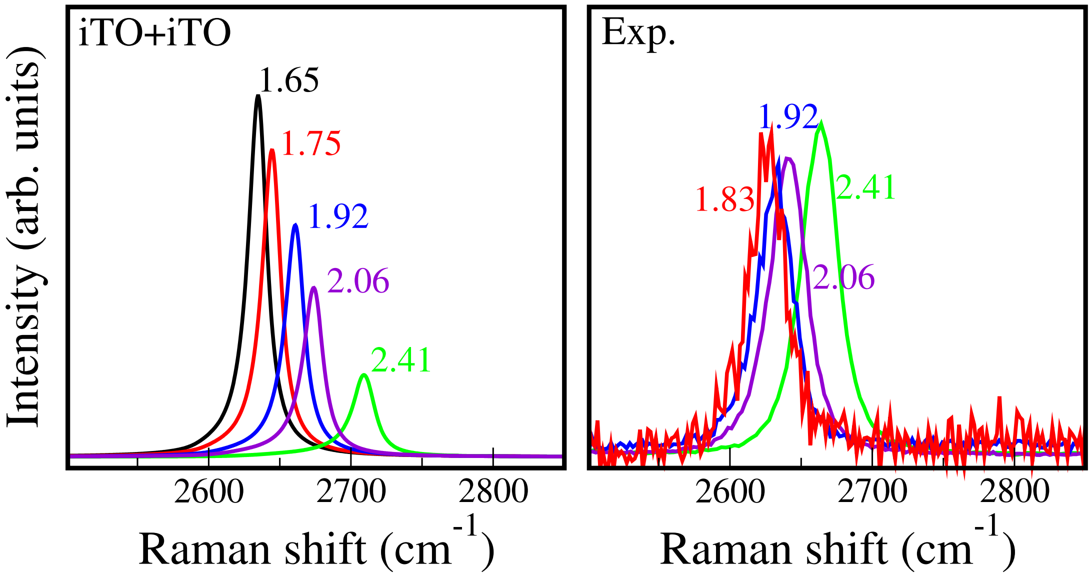

Figure 6.4: Theoretical (left) and experimental (right) G' band spectra for single layer graphene for the different excitation laser energies. The number for each peak indicates the excitation laser energy. The experimental result is given by Mr. A. Reina in MIT in the collaboration with our group [26].

sub-peak due to the smallest phonon wave vector $\mathbf{q}_{22}$. The inter-mediate sub-peaks are associated with the P_{12} and P_{21} processes. The ETB calculation for the energy dispersion relations for the double layer graphene gives same phonon wave vector for $\mathbf{q}_{12}$ and $\mathbf{q}_{21}$. Thus, the inter-mediate sub-peaks for the P_{12} and P_{21} processes are degenerated at same frequency.

For the case of triple layer graphene, we can also neglect the optical matrix elements which connect different subband indexes of the valence and conduction bands, because of the appearance of a similar dipole selection rule to the double layer case. As the result, there are nine possible double resonance Raman scattering processes in triple layer graphene, as shown in Fig. 6.3. The P_{11} and P_{33} processes give the highest and lowest frequency sub-peaks in the G' band spectra with corresponding the phonon wave vectors $\mathbf{q}_{11}$ and $\mathbf{q}_{33}$, where $\mathbf{q}_{11} = \mathbf{k}_1 - \mathbf{k}'_1$, and $\mathbf{q}_{33} = \mathbf{k}_3 - \mathbf{k}'_3$. The other sub-peaks in the G' band spectra for the triple layer graphene are associated with the degenerated processes $\mathrm{P}_{21} + \mathrm{P}_{12}$, $\mathrm{P}_{22} + \mathrm{P}_{13} + \mathrm{P}_{31}$, and $\mathrm{P}_{23} + \mathrm{P}_{32}$, which give similar phonon wave vectors to one another for each sub-peak.

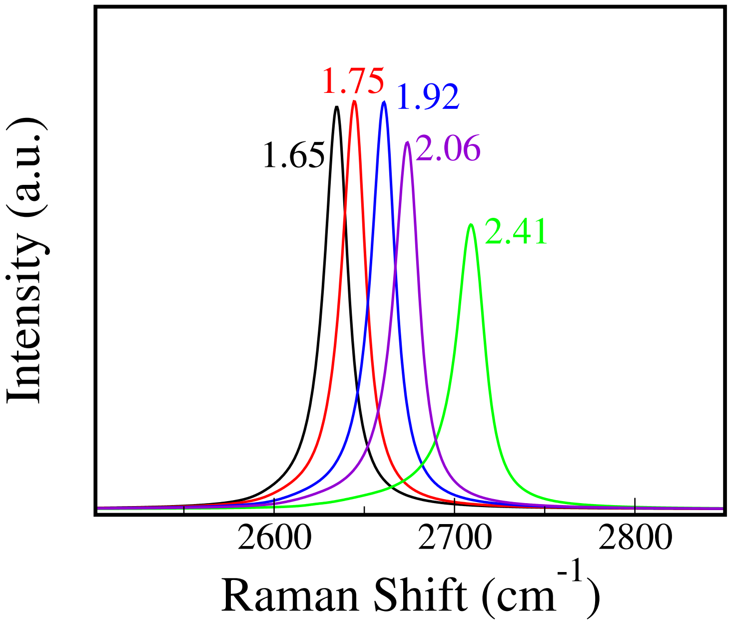

Figure 6.5: The G' band calculation for excitation laser energies E_{L} =1.65, 1.75, 1.92, 2.06, and 2.41 eV, for single layer graphene without considering E_{L} factor in the optical matrix elements of Eq. (3.1.4). Thus, the calcuated G' band intensity as a function of the excitation laser energy becomes similar to the experiment in right panel of Fig. 6.4.

6.2 G' band spectra

6.2.1 Single layer graphene

Figure 6.4 shows the theoretical (left) and experimental (right) G' band spectra for the different excitation laser energies for the single layer graphene. Since the calculated G' band spectra-widths for different excitation laser energies are similar to one another, the comparison of the peak intensities should apply to the values of integrated intensity. The calculated peak intensity of the G' band decreases with increasing laser energy, while the experimental results show an irregular behavior. The experimental G' band spectra shown in Fig. 6.4 are obtained by normalizing the measured G' band peak intensity to that for the G band. As the excitation laser energy changes from 1.83 eV to 2.41 eV, the experimental G' band peak intensity behavior does not show any special tendency whether it decreases or not with increasing excitation energy as shown in right panel of Fig. 6.4, contrary to the calculated result. In Chapter 5, we showed that the optical matrix elements $M_{\mathrm{el-op}}$ of

SWNTs decrease with increasing excitation laser energy. For the graphene sheet, we also obtain the same result. This excitation laser energy dependence appears in Eq. (3.1.4) for the optical matrix elements calculation. By substituting the absorption and emission optical matrix from Eq. (3.1.4) into Eq. (3.4.1), we can get the result that the G' band Raman intensity is proportional to E_{L}^{-3}. The excitation laser energy dependence of the electron-phonon matrix elements for iTO phonon are small and can be neglected. Thus, theoretical G' band intensity shows the dependence of electron-photon matrix element on the excitation laser energy E_L.

However, if we neglect the E_{L} dependence of the optical matrix element formula in Eq. (3.1.4), the calculated G' band Raman intensity as a function of the excitation energy E_{L} becomes similar to the experiment, as shown in Fig. 6.5, which can be compared with the experiment, since the marix element for G band also depends on the electron-photon matrix element. The E_{L} dependence in Eq. (3.1.4) comes from the fact that the stimulated absorption and spontaneous emission optical processes occur for $M_{\mathrm{el-op}}^{\mathrm{ab}}$ and $M_{\mathrm{el-op}}^{\mathrm{em}}$, respectively.

6.2.2 Double layer graphene

Figure 6.6 shows the peak fitting results of the experimental and calculated G' bands for double layer (2L) graphene with E_{L} =2.41 eV. Even though there are four possible double Raman scattering processes which contribute to the G' band spectra of double layer graphene, our calculation shows only three sub-peaks, P_{11}, $\mathrm{P}_{12}+\mathrm{P}_{21}$, and P_{22}, since the phonon wave vectors $\mathbf{q}_{12}$ and $\mathbf{q}_{21}$ are almost the same. As explained in previous Section, the peak P_{11} is arranged a higher frequency component compared with $\mathrm{P}_{12}+\mathrm{P}_{21}$ and P_{22} sub-peaks. Therefore, the experimental G' band spectra of 2L graphene is also fitted to three peak components, as shown in Fig. 6.6 (bottom). In the calculation, the middle sub-peak intensity is the strongest of the three components, but in experiment, the P_{11} peak has the strongest intensity.

We should mention that, for comparing the calculated frequency with the experiment for the G' band, we did not use the calculated phonon energy dispersion but numerically the experimental fitting formula for iTO phonon frequency [33], $\omega(\mathrm{cm}^{-1}) = 1241(\mathrm{cm}^{-1}) + 313(\mathrm{cm}^{-1}\text{Å})q$, where q is the phonon wave vector from the K point. It is because that the calculated phonon energy dispersion does not reproduce the dispersion of the experimental

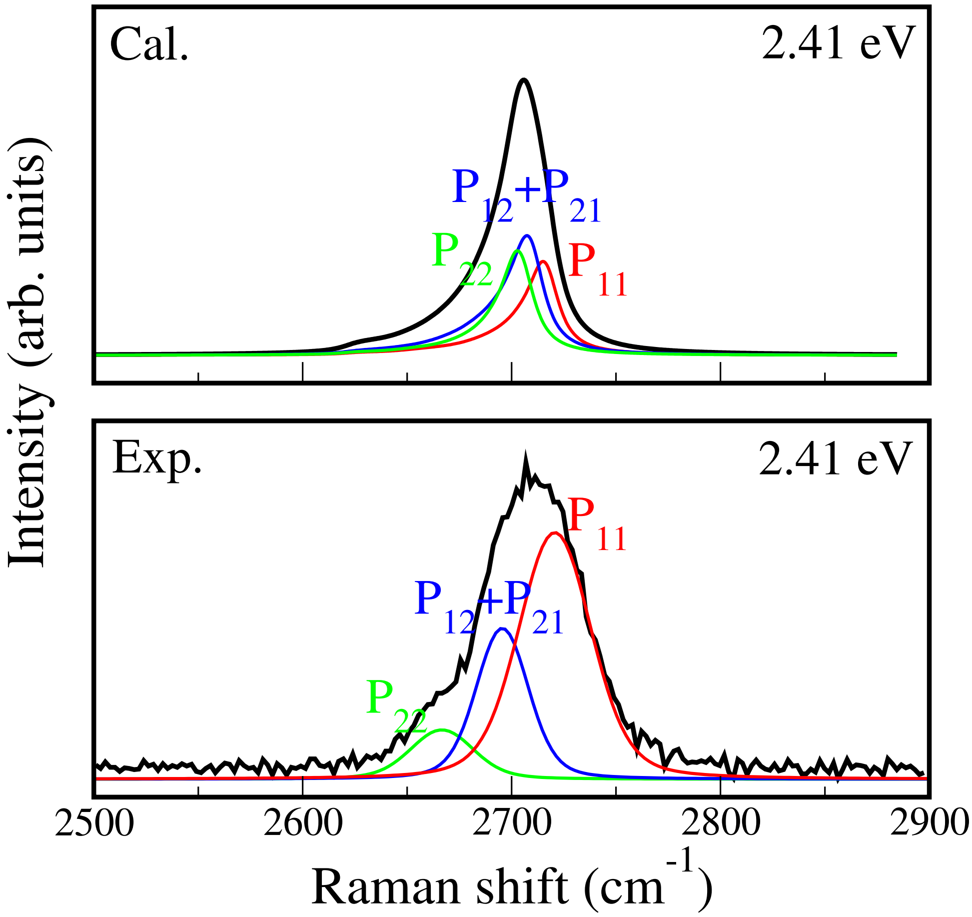

Figure 6.6: Theoretical (top) and experimental [26] (bottom) fitting of the G' band spectra for the double layer graphene with three Lorentzian components at the excitation laser energy 2.41 eV. Red, blue, and green solid lines represent P_{11}, $P_{12}+P_{21}$, and P_{22} scattering processes, respectively.

G' band frequency. If the Kohn anomaly [90, 98], which gives more dispersive phonon frequency around the K point, is considered in the calculation of the phonon dispersion relation, the comparison of the calculation with the experiment will be further improved.

Figure 6.7 shows the dispersion of the G' band sub-peaks for the double layer graphene as a function of laser excitation energy for the calculation (left) and the experiment (right). The dispersion of the G' band for the single layer graphene is also shown as red line. It can be expected that the single layer G' band frequency lies midway between the optical processes P_{11} and P_{22} and is similar with the $P_{12} + P_{21}$ peak position, as shown in the calculation result. However, the experimental middle peak component of double layer

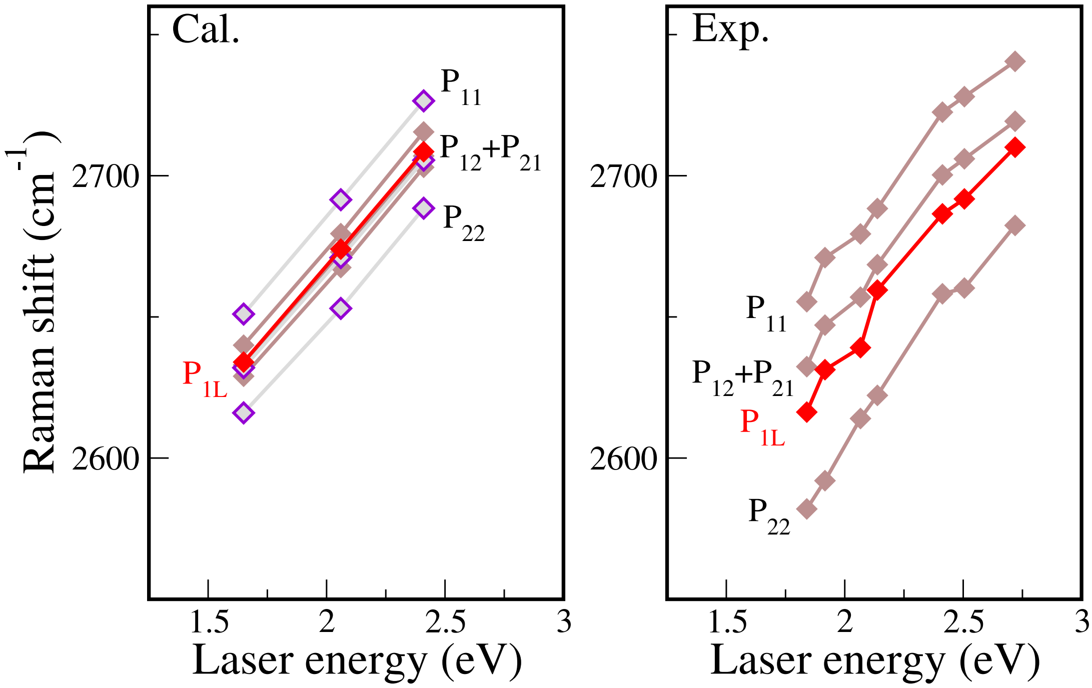

Figure 6.7: The theoretical (left) and experimental (right) [26] phonon energy dispersions of the G' band as a function of the excitation laser energy for the three sub-peaks fitting to the G' band of double layer graphene, respectively. Red line indicates the G' band dispersion of single layer graphene. In the left panel, brown and gray lines mean the G' band calculation for different inter-layer distance between upper and bottom graphene layers, 0.34 and 0.30 nm, respectively.

graphene, which accounts for the $P_{12} + P_{21}$ processes, is up-shifted with respect to the single layer G' band frequency. It might be that the blue-shift of the middle peak for the double layer graphene results from environment effect such as the interaction between bottom layer and SiO_2 substrate. The calculated G' band width is narrow in comparison to experiment. The G' band width depends on the inter-layer distance between upper and bottom graphene layers. In general, the experimental inter-layer distance is known as 0.34 nm. In left panel of Fig. 6.7, brown and gray lines represent the G' band calculation for different inter-layer distance, 0.34 and 0.30 nm, respectively. Even though the inter-layer distance 0.30 nm is very narrow experimentally, the theoretical comparison shows that the G' band width becomes broad with deceasing inter-layer distance.

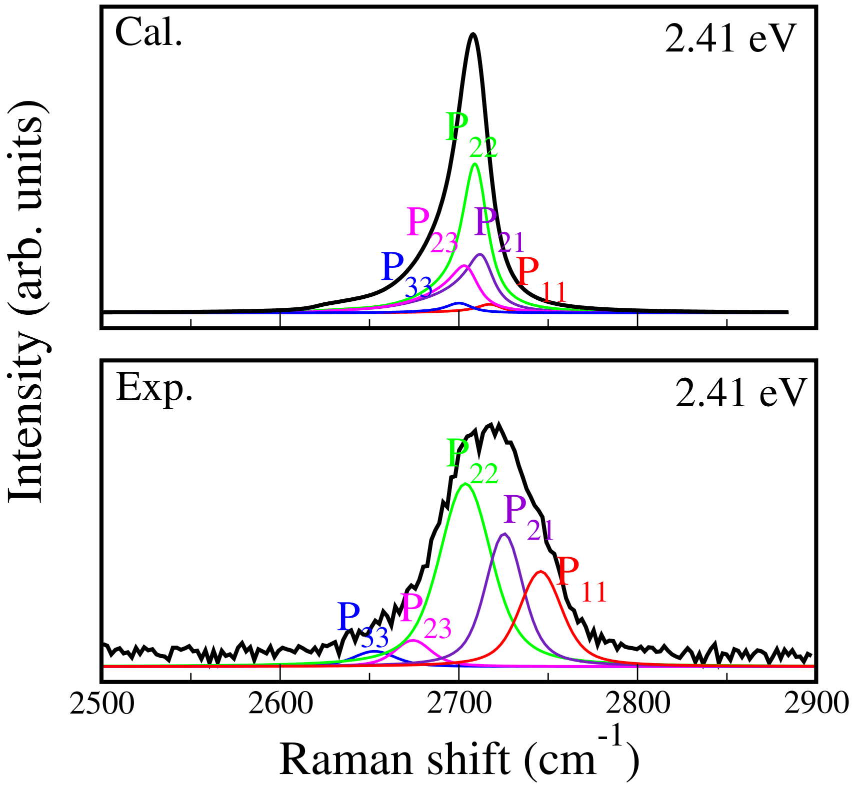

Figure 6.8: Theoretical (top) and experimental [26] (bottom) fittings of triple layer graphene G' band spectra with five peak components at the excitation laser energy 2.41 eV. Red, violet, green, pink, and blue solid lines represent P_{11}, $\mathrm{P}_{12}+\mathrm{P}_{21}$, $\mathrm{P}_{13}+\mathrm{P}_{22}+\mathrm{P}_{31}$, $\mathrm{P}_{23}+\mathrm{P}_{32}$, and P_{33} scattering processes. In this plot, we simply label the degenerated components $\mathrm{P}_{12}+\mathrm{P}_{21}$, $\mathrm{P}_{13}+\mathrm{P}_{22}+\mathrm{P}_{31}$, $\mathrm{P}_{23}+\mathrm{P}_{32}$ to P_{21}, P_{22}, P_{23}, respectively.

6.2.3 triple layer graphene

In Fig. 6.8, we show the peak fitting of the theoretical (top) and experimental (bottom) G' bands with 2.41 eV. As already explained in Section 6.1, the triple layer graphene has nine possible double resonance Raman processes which contribute to the G' band spectra, but five sub-peaks appear in the calculation such as P_{11}, $\mathrm{P}_{21}+\mathrm{P}_{12}$, $\mathrm{P}_{13}+\mathrm{P}_{22}+\mathrm{P}_{31}$, $\mathrm{P}_{23}+\mathrm{P}_{32}$, and P_{33}, due to same phonon wave vector. Hereafter, we simply label the degenerated sub-peak components $\mathrm{P}_{12}+\mathrm{P}_{21}$, $\mathrm{P}_{13}+\mathrm{P}_{22}+\mathrm{P}_{31}$, $\mathrm{P}_{23}+\mathrm{P}_{32}$ to P_{21}, P_{22}, P_{23}, respectively. Therefore, a fit is made of five peaks in the G' band spectra of triple layer graphene for the experimental Raman spectra with E_{L} =2.41 eV, as shown in Fig. 6.8. In the calculation, the G' band peak position for the triple layer graphene is consistent with

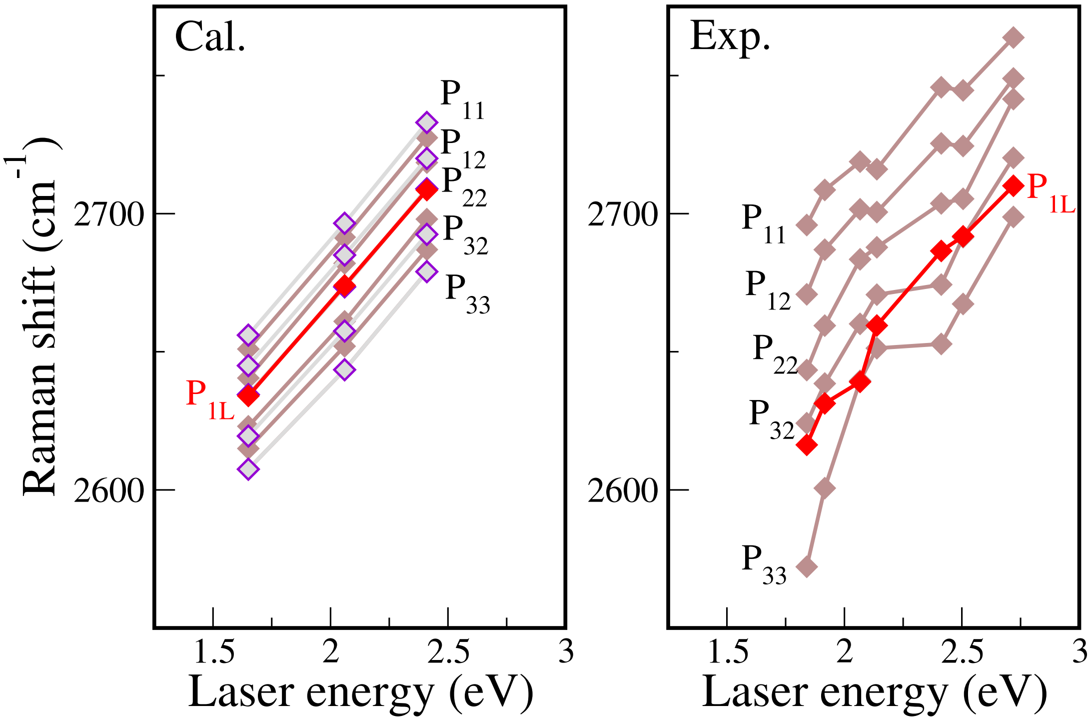

Figure 6.9: Theoretical (left) and experimental (right) [26] phonon energy dispersions of the five peak components P_{11}, P_{12}, P_{22}, P_{32}, and P_{33} in the G' band of triple layer graphene as a function of the excitation laser energy. Red line indicates the G' band dispersion of single layer graphene. In the left panel, brown and gray lines mean the G' band calculation for the different inter-layer distance between upper and bottom graphene layers, 0.34 and 0.30 nm, respectively.

the sub-peak P_{22} position. However, in the experiment, the P_{22} peak slightly deviates from the G' band peak position.

In Fig. 6.9, the dispersion of the G' band sub-peaks for the triple layer graphene is shown as a function of excitation laser energy for the calculation (left) and the experiment (right). In experiment, the dispersion for the single layer graphene G' band peak (red line) is almost consistent with that of the peak P_{23} in triple layer graphene G' band, as shown in Fig. 6.9. The calculated dispersion of single layer graphene is overlapped to the sub-peak P_{22}. Similar to the case of double layer graphene, when the inter-layer distance decreases from 0.34 (brown line) to 0.30 nm (gray line), the G' band for the triple layer become broad from the center peak P_{22}, as shown in left panel of Fig. 6.9.

Finally, we compare the G' band for different number of graphene layers, and compare

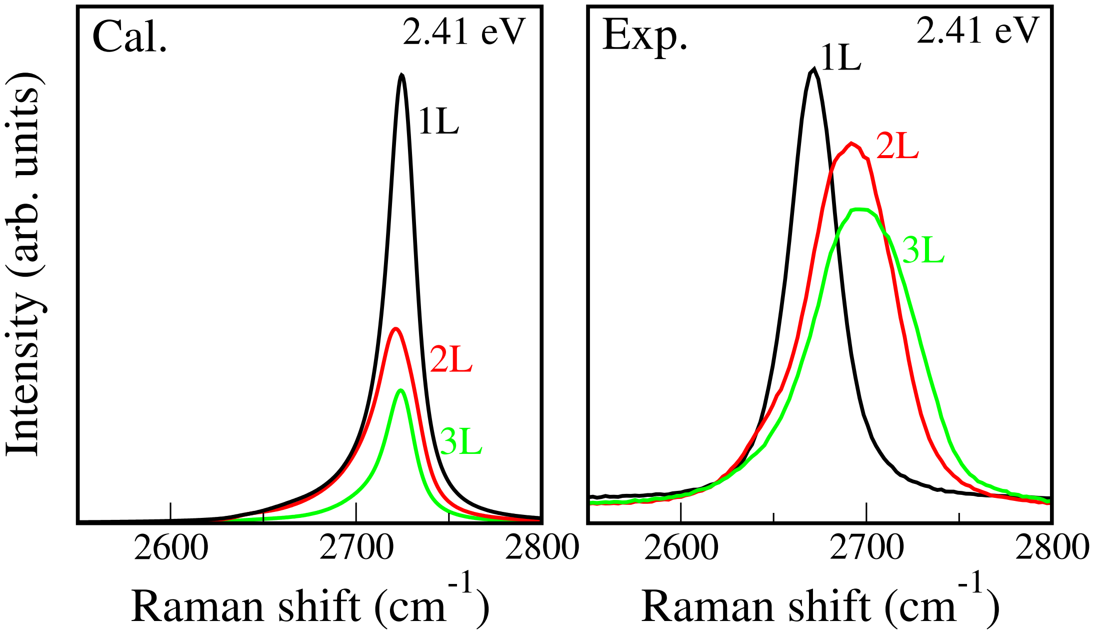

Figure 6.10: The dependence of the G' band intensity for $E_{\rm L} = 2.41$eV as a function of the number of layers for the calculation (left) and experiment [26] (right), respectively. Black, red, and green lines indicate the G' band for single, double, and triple layer graphenes, respectively.

the calculation with the experiment. In Fig. 6.10, the calculated G' band peak intensity decreases with number of layers, agreeing with the experimental G' band spectra calculations. The experimental G' band peak intensity of double layer graphene is 20% larger than that of the triple layer graphene, whereas the G' band peak intensity of single layer is 25% larger than that of double layer as shown in Fig. 6.10. However, in the calculation, the G' band peak intensity of the double layer graphene is 46% larger than that of the triple layer graphene, and that of the single layer graphene is 77% larger than that of the double layer graphene. In the experiment, the double layer G' band spectra-width (55 cm^{-1}) is nearly twice of single layer graphene (28 cm^{-1}), which agrees with our calculation. The calculated spectra-widths of the double and single layer graphenes are 29 cm^{-1} and 19 cm^{-1}, respectively. Since we use $\gamma = 10$ meV for all numbers of layers, the calculated spectra-width comes from the fact that each peak of the double resonance scattering process shifts to one another. The experimental spectra-width of triple layer graphene is only 10-20 % larger than that of double layer graphene. For the calculated G'

band spectra-width, we obtained a spectra-width (24 cm^{-1}) for triple layer graphene that is slightly small compared with that of double layer graphene (29 cm^{-1}). Even though the G' band of triple layer graphene has more optical processes (nine) than that of double layer graphene (four), both outside peaks (P_{11} and P_{33}) of the nine G' band components have a much smaller intensity than the main components, and the split width of the energy band near the Fermi level for triple layer graphene does not become larger than that of double layer graphene, so that we get a smaller calculated spectra-width for triple layer graphene than for double layer graphene. The split width of the energy band near the Fermi level depends on the interlayer distance, in which we fixed it as 0.34 nm. If the interlayer distance decreases, the split width of the energy band becomes larger as explained above. This fact results in the increase of the G' band spectra-width for the double and triple layer graphene. Moreover, the experimental G' band center frequency increases with increasing number of layers as shown in Fig. 6.10. However, the increase between single and double layer is 20 cm^{-1} while the increase between 2L and 3L is only 10 cm^{-1}. Such a G' band peak frequency shift with number of layers might be caused by the interaction between the SiO_2 substrate and the bottom layer graphene. According to the double resonance Raman theory, if an environmental effect does not exist, then there should not be a shift in the averaged G' band peak frequency as the number of graphene layers changes.

6.3 Summary

We calculated the G' band Raman spectra of single, double, and triple layer graphenes and in particular, analyzed the peak FWHM, frequency, and peak intensity for different number of layers and for the different excitation laser energies. The G' band calculation is based on the double resonance Raman theory. As the result, we found that there are four and nine optical processes that contribute to the G' band for the double and triple layer graphenes, respectively. In the other papers which have studied the G' band of double layer graphene, four peak components are used to describe the G' band [32, 33]. However, theoretically, each peak position depends on a wave vector, and then the two middle peak components are degenerate. Therefore, we suggest that the G' band of double layer graphene can be described by three components and correspondingly triple layer graphene has five components. This point might explain the reason why the G' band width of graphite does not become much larger than that of double layer graphene. The dependence of the G' band peak intensity on the excitation laser energy is predicted to decrease due to decrease of the electron-photon matrix elements with increasing excitation laser energy. When we discuss the relative intensity of G' band to G band, the energy dependence of electron-photon matrix elements disappears and thus the agreement with the experimental results that are given by the peak intensity ratio G'/G is satisfactory.

Chapter 7

Conclusion

In this thesis, we calculated the double resonance Raman scattering processes for the single wall carbon nanotubes (SWNTs) and the multi-layer graphene based on the double resonance Raman theory. The double resonance Raman theory requires the electron-photon matrix elements, the electron-phonon matrix elements, and the resonance windows for satisfying the resonance condition and for obtaining the Raman intensity. Such a calculation involves the electron and phonon dispersion relations, and we adopt the extended tight binding method for the calculation as explained in Chapter 2. For the intensity calculation of the resonance Raman spectroscopy (RRS), the electron-photon and electron-phonon matrix elements are obtained by the dipole vector and the atomic deformation potential vector, respectively. Until now, these matrix elements have given many information for the experimental optical spectra for SWNT and graphene. However, we showed in Chapter 4 that we need more precise Raman intensity calculation for different (n, m) SWNTs and we need to calculate the Raman resonance windows. The Raman resonance window is defined as the energy dissipation by inelastic electron-phonon scattering and obtained by calculating the transition probability of the excited electron in the conduction band. The transition probability calculated by electron-phonon scattering is given by the Fermi Golden rule. As the result, the resonance windows for different (n, m) SWNTs depend on $S1$ and $S2$ type in semiconducting SWNTs, and diameter and chiral angle. Also, the resonance windows depend on the transition path, for example, E_{22}^{S}, E_{11}^{M}, and E_{33}^{S}, because the higher transition has the more relaxation paths. The calculation results are in a good agreement with the experiment except for metallic SWNTs. In the case of metallic SWNTs, we expect that the relaxation of a photo-excited electron in the conduction band results from not only the electron-phonon scattering but also the electron-plasmon scattering due to two linear energy band around the Fermi level.

Based on the results of electron-photon, electron-phonon matrix elements, and the Raman resonance widows, we calculated the G' band Raman spectra which appears at 2650 cm^{-1} as one of important features in RRS of SWNTs, in Chapter 5. The G' band of SWNTs is positively dispersive with increasing the excitation laser energy, and results from two-phonon inter-valley scattering, and has a strong metallicity dependence of the intensity. We suggested that the G' band comes from the overtone of the iTO phonon mode by deducing the G' band properties. The electron-phonon matrix elements for the iTO phonon mode show the dependence on the electronic transition energies such as E_{22}^S, E_{11}^M, and E_{33}^S. The resonance windows for metallic SWNTs give smaller values than those for semiconducting SWNT. This is the main reason why the G' band intensity depends on the metallicity in SWNTs.

Furthermore, we expend the G' band calculation to the case of multi-layer graphene. Comparison with single layer graphene, the multi-layer graphene has inter-layer interaction between π electrons on the different layers, and then the electronic energy band structure of the multi-layer graphene is split to several energy sub-bands around the Fermi level. The split energy bands make many double resonance Raman scattering processes, and give broad G' band compared with single layer graphene. Also, we checked that the G' band intensity of multi-layer graphene depends on the number of layers because the electron-phonon matrix elements decrease with increasing the number of graphene layers. The calculated results are in a good agreement with the experiment.

Bibliography

[1] S. Iijima, Nature (London) **354**, 56 (1991).

[2] S. Iijima and T. Ichihashi, Nature **363**, 603 (1993).

[3] D.S. Bethune, C. H. Kiang, M. S de Vries, G. Gorman, R. Sacoy, J. Vasquez, and R. Beyers, Nature(London) **363**, 605 (1993).

[4] R. Saito, M. Fujita, G. Dresselhaus, and M. S. Dresselhaus, Appl. Phys. Lett. **60**, 2204 (1992).

[5] R. Saito, G. Dresselhaus, and M.S. Dresselhaus, *Physical Properties of Carbon Nanotubes* (Imperial College Press, London, 1998).

[6] M.S. Dresselhaus, G. Dresselhaus, and P. Avouris, *Carbon Nanotubes-Synthesis, Structure, Properties, and Application* (Springer, Berlin, 2001).

[7] M. S. Dresselhaus, G. Dresselhaus, R. Saito, and A. Jorio, Physics Reports **409**, 47 (2005).

[8] J. Jiang, R. Saito, A. Grüneis, S. G. Chou, Ge. G. Samsonidze, A. Jorio, G. Dresselhaus, and M. S. Dresselhaus, Phys. Rev. B **71**, 205420 (2005).

[9] C. Fantini, A. Jorio, M. Souza, M. S. Strano, M. S. Dresselhaus, and M. A. Pimenta, Phys. Rev. Lett. **93**, 147406 (2004).

[10] H. Kataura, Y. Kumazawa, Y. Maniwa, I. Umezu, S. Suzuki, Y. Ohtsuka, and Y. Achiba, Synth. Metals **103**, 2555–2558 (1999).

[11] A. Jorio, A. P. Santos, H. B. Ribeiro, C. Fantini, M. Souza, J. P. M. Vieira, C. A. Furtado, J. Jiang, L. Balzano, D. E. Resasco, and M. A. Pimenta, Phys. Rev.B **72**, 075207 (2005).

[12] J. Jiang, R. Saito, Ge. G. Samsonidze, S. G. Chou, A. Jorio, G. Dresselhaus, and M. S. Dresselhaus, Phys. Rev. B **72**, 235408 (2005).

[13] Y. Oyama, R. Saito, K. Sato, J. Jiang, Ge. G. Samsonidze, A. Grüneis, Y. Miyauchi, S. Maruyama, A. Jorio, G. Dresselhaus, and M. S. Dresselhaus, Carbon **44**, 873 (2006).

[14] Ge. G. Samsonidze, R. Saito, N. Kobayashi, A. Grüneis, J. Jiang, A. Jorio, S. G. Chou, G. Dresselhaus, and M. S. Dresselhaus, Appl. Phys. Lett. **85**, 5703 (2004).

[15] A. Jorio, C. Fantini, M. A. Pimenta, D. A. Heller, M. S. Strano, M. S. Dresselhaus, Y. Oyama, J. Jiang, and R. Saito, Appl. Phys. Lett. **88**, 023109 (2006).

[16] T. Okazaki, T. Saito, K. Matsuura, S. Ohshima, M. Yumura, Y. Oyama, R. Saito, and S. Iijima, Chem. Phys. Lett. **420**, 286 (2005).

[17] V. W. Brar, Ge. G. Samsonidze, G. Dresselhaus, M. S. Dresselhaus, R. Saito, A. K. Swan, M. S. Ünlü, B. B. Goldberg, A. G. Souza Filho, and A. Jorio, Phys. Rev. B **66**, 155418 (2002).

[18] A. Jorio, R. Saito, J. H. Hafner, C. M. Lieber, M. Hunter, T. McClure, G. Dresselhaus, and M. S. Dresselhaus, Phys. Rev. Lett. **86**, 1118 (2001).

[19] M. Milnera, J. Kurti, M. Hulman, and H. Kuzmany, Phys. Rev. Lett. **84**, 1324 (2000).

[20] A. Jorio, A. G. Souza Filho, G. Dresselhaus, M. S. Dresselhaus, A. K. Swan, M. S. Unlu, B. B. Goldberg, M. A. Pimenta, J. H. Hafner, C. M. Lieber, and R. Saito, Phys. Rev. B **65**, 155412 (2002).

[21] R. Saito, A. Jorio, J. H. Hafner, C. M. Lieber, M. Hunter, T. McClure, G. Dresselhaus, and M. S. Dresselhaus, Phys. Rev. B **64**, 085312 (2001).

[22] J. Jiang, R. Saito, A. Grüneis, S. G. Chou, Ge. G. Samsonidze, A. Jorio, G. Dresselhaus, and M. S. Dresselhaus, Phys. Rev. B **71**, 205420 (2005).

[23] K. K. Kim, J. S. Park, S. J. Kim, H. Z. Geng, K. H. An, C. M. Yang, K. Sato, R. Saito, and Y. H. Lee, Phys. Rev. B **76**, 205426 (2007).

[24] K. H. An, J. S. Park, C. M. Yang, S. Y. Jeong, S. C. Lim, C. Kang, J. H. Son, M. S. Jeong, and Y. H. Lee, J. Am. Chem. Soc. **127**, 5196 (2005).

[25] C. M. Yang, J. S. Park, K. H. An, S. C. Lim, K. Seo, B. Kim, K. A. Park, S. Han, C. Y. Park, and Y. H. Lee, J. Phys. Chem. B **109** (2005).

[26] J. S. Park, A. Reina, R. Saito, J. Kong, G. Dresselhaus, and M. S. Dresselhaus, submitted to Carbon (2008).

[27] K. S. Novoselov, A. K. Geim, S. V. Morozov, M. I. Katsnelson D. Jiang, I. V. Grigorieva, S. V. Dubonos, and A. A. Firsov, Nature **438**, 197 (2005).

[28] Y. Zhang, Y. W. Tan, H. L. Stormer, and P. Kim, Nature **438**, 201 (2005).

[29] Y. Zhang, J. P. Small, W. V. Pontius, and P. Kim, Appl. Phys. Lett. **86**, 073104 (2005).

[30] C. Berger, Z. Song, T. Li, X. Li, A. Y. Ogbazghi, R. Feng, Z. Dai, A. N. Marchenkov, E. H. Conrad, P. N. First, and W. A. de Heer, J. Phys. Chem. B **108**, 19912 (2004).

[31] K. S. Novoselov, D. Jiang, F. Schedin, T. J. Booth, V. V. Khotkevich, S. V. Morozov, and A. K. Geim, Proc. Natl. Acad. Sci. **102**, 10451 (2005).

[32] A. C. Ferrari, J. C. Meyer, V. Scardaci, C. Casiraghi, M. Lazzeri, F. Mauri, S. Piscanec, D. Jiang, K. S. Novoselov, S. Roth, and A. K. Geim, Phys. Rev. Lett. **97**, 187401 (2006).

[33] L. M. Malard, J. Nilsson, D. C. Elias, J. C. Brant, F. Plentz, E. S. Alves, A. H. Castro Neto, and M. A. Pimenta, Phys. Rev. B **76**, 201401 (2007).

[34] J. Jiang, R. Saito, A. Grüneis, G. Dresselhaus, and M. S. Dresselhaus, Chem. Phys. Lett. **392**, 383 (2004).

[35] J. Jiang, R. Saito, A. Grueneis, G. Dresselhaus, and M. S. Dresselhaus, Carbon **42**, 3169 (2004).

[36] A. Grueneis, R. Saito, Ge. G. Samsonidze, T. Kimura, M. A. Pimenta, A. Jorio, A. G. Souza Filho, G. Dresselhaus, and M. S. Dresselhaus, Phys. Rev. B **67**, 165402 (2003).

[37] J. W. McClure, Phys. Rev. **108**, 612 (1957).

[38] J. C. Slonczewski and P. R. Weiss, Phys. Rev. **109**, 272 (1958).

[39] C. Journet, W. K. Maser, P. Bernier, A. Loiseau, M. Lamy de la Chapelle, S. Lefrant, P. Deniard, R. Lee, and J. E. Fischer, Nature (London) **388**, 756–758 (1997).

[40] A. Thess, R. Lee, P. Nikolaev, H. Dai, P. Petit, J. Robert, C. Xu, Y. H. Lee, S. G. Kim, A. G. Rinzler, D. T. Colbert, G. E. Scuseria, D. Tománek, J. E. Fischer, and R. E. Smalley, Science **273**, 483–487 (1996).

[41] P. Nikolaev, M. J. Bronikowski, R. K. Bradley, F. Rohmund, D. T. Colbert, K. A. Smith, and R. E. Smalley, Chem. Phys. Lett. **313**, 91 (1999).

[42] C. Bower, W. Zhu, S. Jin, and O. Zhou, Appl. Phys. Lett. **77**, 830 (2000).

[43] T. W. Ebbesen, H. Hiura, J. Fujita, Y. Ochiai, S. Matsui, and K. Tanigaki, Chem. Phys. Lett. **209**, 83 (1993).

[44] R. Bacon, J. Appl. Phys. **31**, 283–290 (1960).

[45] W. Krätschmer, L. D. Lamb, K. Fostiropoulos, and D. R. Huffman, Nature (London) **347**, 354–358 (1990).

[46] J. Kong, A. M. Cassel, and H. Dai, Chem. Phys. Lett. **292**, 567 (1998).

[47] J. Kong, H. T. Soh, A. M. Casswell, C. F. Quate, and H. Dai, Nature (London) **395**, 878–881 (1998).

[48] A. M. Cassell, N. R. Franklin, T. W. Tombler, E. M. Chan, J. Han, and H. Dai, J. Am. Chem. Soc. **121**, 7975 (1999).

[49] N. R. Franklin and H. Dai, Advanced Materials **12**, 890 (2001).

[50] H. Soh, C. Quate, A. Morpurgo, C. Marcus, J. Kong, and H. Dai, Appl. Phys. Lett. **75**, 627 (1999).

[51] S. Berber, Y. K. Kwon, and D. Tománek, Phys. Rev. Lett. **84**, 4613 (2000).

[52] A. G. Souza Filho, A. Jorio, Anna K. Swan, M. S. Ünlü, B. B. Goldberg, R. Saito, J. H. Hafner, C. M. Lieber, M. A. Pimenta, G. Dresselhaus, and M. S. Dresselhaus, Phys. Rev. B **65**, 085417 (2002).

[53] R. Saito, A. Jorio, A. G. Souza Filho, G. Dresselhaus, M. S. Dresselhaus, and M. A. Pimenta, Phys. Rev. Lett. **88**, 027401 (2001).

[54] R Saito, A Grüneis, Ge G Samsonidze, V W Brar, G Dresselhaus, M S Dresselhaus, A Jorio, L G Cancado, C Fantini, M A Pimenta, and A G Souza Filho, New J. Phys. **5**, 157 (2003).

[55] R. Saito, A. Jorio, A. G. Souza Filho, G. Dresselhaus, M. S. Dresselhaus, A. Grüneis, L. G. Cançado, and M. A. Pimenta, Japanese J. Appl. Phys. Part 1 **41**, 4878–4882 (2002).

[56] M. S. Dresselhaus, G. Dresselhaus, A. Jorio, A. G. Souza Filho, and R. Saito, Carbon **40**, 2043–2061 (2002).

[57] L. G. Cançado, M. A. Pimenta, R. Saito, A. Jorio, L. O. Ladeira, A. Grüneis, A. G. Souza Filho, G. Dresselhaus, and M. S. Dresselhaus, Phys. Rev. B **66**, 035415 (2002).

[58] Y. Miyauchi, S. Chiashi, Y. Murakami, Y. Hayashida, and S. Maruyama, Chem. Phys. Lett. **387**, 198 (2004).

[59] C. F. Klingshirn, *Semiconductor optics* (Springer, Berlin, 2004).

[60] S. M. Bachilo, M. S. Strano, C. Kittrell, R. H. Hauge, R. E. Smalley, and R. B. Weisman, Science **298**, 2361–2366 (2002).

[61] J. S. Park, Y. Oyama, R. Saito, W. Izumida, J. Jiang, K. Sato, C. Fantini, A. Jorio, G. Dresselhaus, and M. S. Dresselhaus, Phys. Rev. B **74**, 165414 (2006).

[62] B. Kitiyanan, W. E. Alvarez, J. H. Harwell, and D. E. Resasco, Chem. Phys. Lett. **317**, 497 (2000).

[63] Y. Miyauchi, R. Saito, K. Sato, Y. Ohno, S. Iwasaki, T. Mizutani, J. Jiang, and S. Maruyama, Chem. Phys. Lett. **442**, 394–399 (2007).

[64] S. D. M. Brown, A. Jorio, P. Corio, M. S. Dresselhaus, G. Dresselhaus, R. Saito, and K. Kneipp, Phys. Rev. B **63**, 155414 (2001).

[65] C. H. Olk and J. P. Heremans, J. Mater. Res. **9**, 259–262 (1994).

[66] R. Saito, K. Sato, Y. Oyama, J. Jiang, Ge. G. Samsonidze, G. Dresselhaus, and M. S. Dresselhaus, Phys. Rev. B **71**, 153413 (2005).

[67] Ge. G. Samsonidze, R. Saito, A. Jorio, M. A. Pimenta, A. G. Souza Filho, A. Grüneis, G. Dresselhaus, and M. S. Dresselhaus, Journal of Nanoscience and Nanotechnology **3**, 431–458 (2003).

[68] S. J. Tans, M. H. Devoret, H. Dai, A. Thess, R. E. Smalley, L. J. Geerligs, and C. Dekker, Nature (London) **386**, 474–477 (1997).

[69] J. C. Slater and G. F. Koster, Phys. Rev. **94**, 1498 (1954).

[70] G. S. Painter and D. E. Ellis, Phys. Rev. B **1**, 4747 (1970).

[71] S. Reich, C. Thomsen, and J. Maultzsch, *Carbon Nanotubes: Basic Concepts and Physical Properties* (WILEY-VCH, Weinheim, 2003).

[72] G. G. Samsonidze, *Photophysics of Carbon nanotube* (Massachusetts Institute of Technology, PhD Thesis, 2007).

[73] J. W. Hill and R. H. Petrucci, *General Chemistry* (3rd edition, Prentice Hall, NJ, 2002).

[74] A. Jorio, R. Saito, J. H. Hafner, C. M. Lieber, M. Hunter, T. McClure, G. Dresselhaus, and M. S. Dresselhaus, Phys. Rev. Lett. **86**, 1118–1121 (2001).

[75] R. B. Weisman and S. M. Bachilo, Nanoletters **3**, 1235–1238 (2003).

[76] C. L. Kane and E. J. Mele, Phys. Rev. Lett. **90**, 207401 (2003).

[77] V. N. Popov, New J. of Phys. **6**, 17 (2004).

[78] S. Reich, J. Maultzsch, C. Thomsen, and P. Ordejón, Phys. Rev. B **66**, 035412 (2002).

[79] D. Porezag, T. Frauenheim, T. Kohler, G. Seifert, and R.Kaschner, Phys. Rev. B **51**, 12947 (1995).

[80] T. Ando, J. Phys. Soc. Jpn. **66**, 1066–1073 (1997).

[81] C. L. Kane and E. J. Mele, Phys. Rev. Lett. **93**, 197402 (2003).

[82] T. G. Pedersen, Phys. Rev. B **67**, 073401 (2003).

[83] V. Perebeinos, J. Tersoff, and Ph. Avouris, Phys. Rev. Lett. **92**, 257402 (2004).

[84] H. Zhao and S. Mazumdar, Phys. Rev. Lett. **93**, 157402 (2004).

[85] J. Jiang, R. Saito, Ge. G. Samsonidze, A. Jorio, S. G. Chou, G. Dresselhaus, and M. S. Dresselhaus, Phys. Rev. B **75**, 035407–1–13 (2007).

[86] J. W. Mintmire, B. I. Dunlap, and C. T. White, Phys. Rev. Lett. **68**, 631–634 (1992).

[87] R. A. Jishi, M. S. Dresselhaus, and G. Dresselhaus, Phys. Rev. B **48**, 11385–11389 (1993).

[88] J. Jiang, R. Saito, A. Grüneis, S. G. Chou, Ge. G. Samsonidze, A. Jorio, G. Dresselhaus, and M. S. Dresselhaus, Phys. Rev. B **71**, 045417 (2005).

[89] O.Dubay and G.Kresse, Phys. Rev. B **67**, 035401 (2003).

[90] J. Maultzsch, S. Reich, C. Thomsen, H. Requardt, and P. Ordejon, Phys. Rev. Lett. **92**, 075501 (2004).

[91] R. Saito and H. Kamimura, Phys. Rev. B **33**, 7218 (1986).

[92] R. Saito, G. Dresselhaus, and M. S. Dresselhaus, Phys. Rev. B **61**, 2981 (2000).

[93] J. Jiang, R. Saito, K. Sato, J. S. Park, Ge. G. Samsonidze, A. Jorio, G. Dresselhaus, and M. S. Dresselhaus, Phys. Rev. B **75**, 035405 (2007).

[94] D. L. Mafra, G. Samsonidze, L. M. Malard, D. C. Elias, J. C. Brant, F. Plentz, E. S. Alves, and M. A. Pimenta, Phys. Rev. **76**, 233407 (2007).

[95] H. Ajiki and T. Ando, Physica B **201**, 349 (1994).

[96] R. Saito, A. Grüneis, Ge. G. Samsonidze, G. Dresselhaus, M. S. Dresselhaus, A. Jorio, L. G. Cançado, M. A. Pimenta, and A. G. Souza, Appl. Phys. A **78**, 1099–1105 (2004).

[97] C.-M. Yang, J. S. Park K. H. An, K. A. Park, S. C. Lim, Y. S. Lee, W. J. Park, and Y. H. Lee, Phys. Rev. B **73**, 075419 (2006).

[98] K. Sasaki, R. Saito, G. Dresselhaus, M. S. Dresselhaus, H. Farhat, and J. Kong, submitted to Phys. Rev. B (2008).

Publication list

First Author Publications

1. J. S. Park, Y. Oyama, R. Saito, W. Izumida, J. Jiang, K. Sato, C. Fantini, A. Jorio, G. Dresselhaus, M. S. Dresselhaus: Raman resonance window of single-wall carbon nanotubes, Phys. Rev. B **74**, 165414 (2006).
2. J. S. Park, A. Reina, R. Saito, J. Kong, G. Dresselhaus, M. S. Dresselhaus: G' band Raman spectra of single, double, and triple layer graphene, submitted to Carbon , (2008).

Co-Author Publications

1. K. H. An, J. S. Park, C. M. Yang, S. Y. Jeong, S. C. Lim, S. Kang, J. H. Son, M. S. Jeong, Y. H. Lee: A Diameter-selective attack on metallic carbon nanotubes by nitronium ions, J. Am. Chem. Soc. **127**, 5196-5203 (2005).
2. C. M. Yang, J. S. Park, K. H. An, S. C. Lim, K. Y. Seo, B. S. Kim, K. A. Park, S. W. Han, C. Y. Park, Y. H. Lee: Diameter-selective chirality separation of single-wall carbon nanotubes by using HNO_3/H_2SO_4 solution, J. Phys. Chem. B **109**, 19242-19248 (2005).
3. K. H. An, C. M. Yang, J. S. Park, S. Y. Jeong, K. A. Park, Y. H. Lee: Intercalant-induced superbundle formation of single-wall carbon nanotubes, J. Phys. Chem. B **109**, 10004-10008 (2005).
4. C. M. Yang, K. H. An, J. S. Park, K. A. Park, S. C. Lim, Y. S. Lee, Y. H. Lee: Preferential etching of metallic single-walled carbon nanotubes with small diameter

by fluorine gas, Phys. Rev. B **73**, 075419 (2006).

5. J. Jiang, R. Saito, K. Sato, J. S. Park, Ge. G. Samsonidze, A. Jorio, G. Dresselhaus, M. S. Dresselhaus: Exciton-photon, Exciton-phonon matrix elements and Resonance Raman Intensity of single wall carbon nanotubes, Phys. Rev. B **75**, 035405-1-10 (2007).

6. K. K. Kim, J. S. Park, S. J. Kim, H. Z. Geng, K. H. An, C. M. Yang, K. Sato, R. Saito, Y. H. Lee: Dependence of the G'-band intensity in Raman spectra on the metallicity of single wall carbon nanotubes, Phys. Rev. B **76**, 205426-1-8 (2007).

First Author Presentations (2005.10-2008.9)

1. J. S. Park, Y. Oyama, R. Saito, W. Izumida, J. Jiang, K. Sato, C. Fantini, A. Jorio, G. Dresselhaus, M. S. Dresselhaus: Raman resonance window of Single wall carbon nanotubes, Seventh International Conference on the Science and Application of Nanotubes (NT06), Hotel Metropolitan Nagano, Nagano, JAPAN, (2006. 6.18-23).

2. J. S. Park, R. Saito, K. Sato, J. Jiang, K. K. Kim, Y. H. Lee, G. Dresselhaus and M. S. Dresselhaus: Chirality dependence of G' band intensity on Raman Spectra of Single Wall Carbon Nanotubes, The 3rd Japan-Korea Sympojium on Carbon Nanotubes, Gyeongju TEMP Hotel, Gyeongju, KOREA, (2006.10.14-17).

3. J. S. Park, R. Saito, K. Sato, J. Jiang, K. K. Kim, Y. H. Lee, G. Dresselhaus and M. S. Dresselhaus: Chirality dependence of G′ band intensity on Raman spectra of single wall carbon nanotubes, The 32nd Fullerene Nanotubes General Symposium, Meijo University at Tempaku Campus, Nagoya, Japan, (2007.2.13-15).

4. J. S. Park, R. Saito, K. Sato, J. Jiang, G. Dresselhaus, M. S. Dresselhaus: Raman Effect by Length Control of the Single Wall Carbon Nanotube, Eighth International Conference on the Science and Application of Nanotubes, NT07, Parque Metalurgico - Centro De Arles e Convencoes, Ouro Preto, Minas Gerais, Brazil, (2007.6.24-29).

5. J. S. Park, R. Saito, K. Sato, J. Jiang, G. Dressselhaus, M. S. Dresselhaus: Excitonic Effect in Short Tube Length of the Single Wall Carbon Nanotube, The 33rd

Fullerene-Nanotubes General Symposium, Kyushu University, Hukuoka, Japan, (2007. 7.11-13).2007

6. J. S. Park, R. Saito, K. Sato, J. Jiang, G. Dressselhaus, M. S. Dresselhaus: Excitonic Effect in Short Tube Length of the Single Wall Carbon Nanotube, A3 Foresight Program (Meeing and Summer School) in Beijing, Tsinghua University, Beijing, China, (2007.7.25-29).

7. J. S. Park, R. Saito, K. Sato, J. Jiang, G. Dressselhaus, M. S. Dresselhaus: Raman Effect by Length Control of the Single Wall Carbon Nanotube, Asia Science Forum, Sendai International Center, Sendai, (2007.9.10-11).

8. J. S. Park, E. B. Barros, R. Saito, G. Dresselhaus, M. S. Dresselhaus: G' band Raman Spectrum of Double Layer Graphene, The 4th Korea-Japan Symposium on Carbon Nanotube, Kansai Seminar House, Kyoto, Japan, (2007.10.28-31).

9. J. S. Park, A. Reina, R. Saito, J. Kong, G. Dresselhaus, M. S. Dresselhaus: G' band Raman spectrum of single, double, and triple layer graphene, The 34th Fullerene-Nanotubes General Symposium, Meijo University, Nagoya, Japan, (2008.3.3-5).